Simulation of Soft Inclusive Events at Hadron Colliders

Zur Erlangung des akademischen Grades eines

Doktors der Naturwissenschaften

von der Fakultät für Physik des

Karlsruher Institutes für Technologie (KIT)

genehmigte

Dissertation

von

Dipl.-Phys. Christian Röhr

aus Rottweil

Tag der mündlichen Prüfung: 14. Februar 2014

Referent: PD Dr. Stefan Gieseke
Korreferent: Prof. Dr. Dieter Zeppenfeld

Abstract

We study the simulation of soft inclusive hadron collisions at high energies. This topic is addressed in two projects: the analysis of colour reconnections in the presence of multiple parton interactions (MPI) and the joint description of diffractive and MPI cross sections. We describe a model for nonperturbative colour reconnections in the Monte Carlo event generator Herwig++. This model redefines colour singlets in the partonic final state after all perturbative parts of the event generation has been completed. Its effects on hadronic final states at lepton and hadron colliders are investigated. Little impact is found in lepton collisions. However, the simulation of soft inclusive events and the underlying event at hadron colliders is sensitive to colour reconnections. Using analyses at parton level, we can attribute the effects seen at hadron level to nonperturbative parts of the event generation. In tunes to hadron collider data we find an improved description of diffraction-reduced minimum-bias data and underlying-event data at several centre-of-mass energies. We furthermore present a parametrization of the enhanced underlying-event model that allows to assess the underlying-event activity at future collider energies. To account for diffraction in the simulation of inclusive hadron-collider event samples, we analytically study the description of diffractive cross sections in a consistent unitarization model. To this end, a two-channel eikonal formalism is employed. Moreover, enhanced pomeron diagrams are taken into account. Using an implementation of this model in Herwig++, we can validate its description of inclusive hadronic cross sections over a wide range of centre-of-mass energies.

Contents

Introduction

Although there has been tremendous progress in the theoretical description of high-energy hadron collisions in recent years, we are still far away from understanding all of its aspects. Meanwhile, precise calculations for many processes that can be probed at the Large Hadron Collider (LHC) are available. These high-precision calculations are, however, limited to regimes in which perturbation theory applies. In Quantum Chromodynamics (QCD), this requires high energy scales in the process, which imply a small gauge coupling.

In the absence of a high energy scale, perturbative QCD is not applicable. Hence we have to rely on nonperturbative models for parts of the simulation of hadron collisions using Monte Carlo event generators. One example concerns hadronization, i.e. the transition of quarks and gluons to hadrons. Essentially, two different nonperturbative models are used for this task in current general-purpose event generators for LHC physics, namely the cluster model [1] and the string model [2]. Both hadronization models are based on theoretical considerations. They include, however, parameters that have to be determined from experimental data.

Another example is the simulation of the underlying event. The signature of hard subprocesses in hadron collisions is always accompanied by additional hadronic activity in all phase space regions. This additional activity, the underlying event, can be explained by means of uncorrelated multiple parton interactions (MPI) [3]. Meanwhile, all recent general-purpose Monte Carlo event generators for LHC physics, Herwig++ [4], Pythia [5, 6] and Sherpa [7], use multiple parton interactions in order to simulate the underlying event. The description of multiple parton interactions within perturbative QCD is possible by introducing a cutoff for the minimum transverse momentum of the parton interactions. In order to describe interactions below this cutoff, however, nonperturbative models have to be employed.

Multiple parton interactions seem to also be a necessary component to describe inclusive data of inelastic events at hadron colliders (minimum-bias data) [8]. Here we follow the convention of Ref. [9] by using the term 'soft inclusive' in order to refer to theoretical models of minimum-bias data. Soft inclusive models are required to assess the impact of simultaneous pp collisions (pileup collisions), which can cause additional hadronic activity in the detector. Compared to earlier hadron colliders, the LHC suffers from a high pileup activity as it operates at high instantaneous luminosities. Since pileup collisions resemble hadron interactions that are studied in minimum-bias analyses, a good modelling of soft inclusive physics is an important component of event generators.

In the following we concentrate on the MPI model in HERWIG++ since this thesis is focussed on developments in this event generator. The perturbative component of the MPI model is implemented in terms of uncorrelated QCD dijet processes at leading order. The model provides a good description of the underlying event in sufficiently hard collisions at the Tevatron [10]: it reproduces the average hadronic activity (the particle multiplicity and the scalar sum of transverse momenta) in the azimuthal region transverse to the jet with the highest transverse momentum. With soft interactions included in the MPI model, the average underlying-event activity can be described in inclusive samples from minimum-bias runs as well [8]. Since soft-jet production is not accessible in perturbative QCD, the free parameters in the soft MPI model are determined in fits to hadronic-cross section data.

A wide range of minimum-bias and underlying-event measurements at the LHC provide the possibility to study the MPI model in more detail [11–21]. The data reveals deficiencies of the soft inclusive model in HERWIG++ in the description of the pseudorapidity distribution of charged particles. Furthermore, the average transverse momentum as a function of the number of charged particles is significantly underestimated in the model. The latter observable is known to be sensitive to nonperturbative colour reconnections [22].

Colour reconnection was originally studied in the context of hadronic WW production at LEP, where the formation of jets in the two W systems was expected to be subject to interference effects [23–29]. Later analyses at LEP could not find strong colour reconnection effects in WW systems [30–32]. Significant effects of colour reconnection, however, can be seen in the generation of soft inclusive hadron collider events using the PYTHIA event generator [22, 33].

In the first part of this thesis we study colour reconnections within the MPI framework in Herwig++. The goal is to improve the agreement of both the soft inclusive and the underlying-event model with hadron collider data, particularly from the LHC. The colour reconnection model that we establish and discuss in this work is thus motivated by phenomenological aspects. Guided by colour preconfinement [34], however, we also give a theoretical motivation for the need of colour reconnection in hadron collisions. We illustrate the physical idea of the model in various analyses of the modelled final state. Furthermore, we present results of tuning this model to the currently available minimum-bias and underlying-event data.

A substantial fraction of the inelastic pp cross section at LHC energies is due to diffractive processes (see e.g. Ref. [35]). These processes are experimentally characterized by a large region in pseudorapidity in which no hadrons are detected. The incoming protons in these processes either remain intact or dissociate into a set of particles with a (typically) low invariant mass.

The soft inclusive model in Herwig++ does not include diffractive processes. A comparison to minimum-bias data is thus only reasonable if the measurement is restricted to phase space regions in which the contribution of diffraction can be neglected, as for example in Ref. [13]. As we show in this thesis, colour reconnection and a dedicated tuning of the MPI model make for a distinct progress in the description of diffraction-reduced minimum-bias data. Including diffractive processes would further increase the scope of the soft inclusive model in Herwig++.

In the second part of this thesis we make a first step towards this goal: we include the calculation of diffractive cross sections in the unitarization model for multiple parton interactions. The formulation of this model is inspired by the underlying models of the event generators Dtujet [36] and Phojet [37, 38]. We determine the free parameters of the new model in fits to cross section data from high-energy hadron collisions.

This thesis is outlined as follows: We start in Chapter 1 by reviewing the main theoretical concepts used in later chapters. In particular, we summarize the physical ideas of the so-called eikonal model. In Chapter 2 we give a brief account of multiple parton interactions in Herwig++. Chapter 3 covers the implementation and analysis of colour reconnections in Herwig++. In Chapter 4 we discuss the calculation of diffractive cross sections in the eikonal model. Finally, Chapter 5 summarizes the main findings of this work.

Chapter 1

Foundations

In this chapter we establish the basic formalism used in later chapters. First, we summarize important results from a general approach to relativistic scattering, S-matrix theory. Furthermore we review relevant aspects of Regge theory. The chapter ends with an introduction to eikonal models. For comprehensive reviews of the topics discussed here we refer to Refs. [39–41].

1.1 Relativistic scattering

The kinematics in two-body exclusive scattering, $a + b \to c + d$, is conveniently described in terms of the Lorentz invariant Mandelstam variables

$$s = (p_a + p_b)^2\,, \quad t = (p_a - p_c)^2\,, \quad u = (p_a - p_d)^2\,, \tag{1.1}$$

and the masses of the external particles m_a, m_b, m_c and m_d. Since these variables satisfy the identity

$$s + t + u = \sum_k m_k^2\,, \tag{1.2}$$

only two of them are independent.

A special case of two-body scattering is elastic scattering, $a + b \to a' + b'$, where in general only the momenta of the particles change in the interaction. Lorentz invariant elastic scattering amplitudes can thus be formulated in terms of two Mandelstam variables and the external masses. In the high-energy limit the masses are often negligible. The scattering amplitude is then a function of two independent variables, for instance the square of the centre-of-mass energy s and the squared momentum transfer t, and can be written as $\mathcal{A}(s, t)$.

Unitarity of the S-matrix, $SS^\dagger = S^\dagger S = \mathbb{1}$, follows directly from conservation of probability. As a consequence one finds the optical theorem, which in the large-s limit reads

$$\sigma_{\text{tot}} = \frac{1}{s} \operatorname{Im} \mathcal{A}_{\text{el}}(s, t = 0) \,. \tag{1.3}$$

It states that the total cross section, i.e. the cross section for $a + b \to$ *anything*, is directly proportional to the imaginary part of the forward elastic scattering amplitude. Hence it is possible to calculate inelastic cross sections from the elastic amplitude at vanishing momentum transfer.

1.2 Impact parameter representation

At high energies geometrical models can be applied to describe elastic scattering since the corresponding interaction length scale is small compared to the transverse size of the colliding particles. The elastic scattering amplitude in the very forward direction can then be written as [42]

$$\mathcal{A}\big(s, t = -q^2\big) = 4s \int \mathcal{A}(s, b)\, \mathrm{e}^{\mathrm{i}\boldsymbol{q}\cdot\boldsymbol{b}}\, \mathrm{d}^2 b \,. \tag{1.4}$$

where $\boldsymbol{b}$ denotes the impact parameter in the two-dimensional plane perpendicular to the direction of motion of the incoming particles. Here we introduce the (dimensionless) impact parameter amplitude $\mathcal{A}(s, b)$.

As is evident from (1.4), the impact parameter amplitude is the Fourier transform of the scattering amplitude in momentum space. By analogy with geometrical optics, we can interpret $\mathcal{A}(s, b)$ thus as the density in impact parameter space for the production of outgoing waves. The Fourier transform may be inverted,

$$\mathcal{A}(s, b) = \frac{1}{16\pi^2 s} \int \mathcal{A}(s, t)\, \mathrm{e}^{-\mathrm{i}\boldsymbol{q}\cdot\boldsymbol{b}}\, \mathrm{d}^2 q \,, \tag{1.5}$$

which clarifies the azimuthal symmetry assumed initially for $\mathcal{A}(s, \boldsymbol{b})$.

In the geometrical model, the total and elastic cross sections are simple functions of the source density in impact parameter space,

$$\sigma_{\text{tot}}(s) = 4 \int \mathrm{d}^2 b \, \operatorname{Im} \mathcal{A}(s, b) \quad \text{and} \quad \sigma_{\text{el}}(s) = 4 \int \mathrm{d}^2 b \, |\mathcal{A}(s, b)|^2 \,. \tag{1.6}$$

The expression for the total cross section follows directly from the optical theorem, (1.3). To obtain the elastic cross section in (1.6), however, it was

assumed that spin effects can be neglected and hence (1.4) is valid also in non-forward directions.

At small momentum transfers the hadronic elastic scattering cross section can effectively be parametrized as

$$\frac{\mathrm{d}\sigma_{\mathrm{el}}(t)}{\mathrm{d}t} \approx \left[\frac{\mathrm{d}\sigma_{\mathrm{el}}}{\mathrm{d}t}\right]_{t=0} \mathrm{e}^{-B_{\mathrm{el}}|t|}\,, \tag{1.7}$$

where B_{el} is called the elastic slope. This quantity is closely connected to the size of the scattering particles: assuming a constant complex phase of $\mathcal{A}\big(s, b^2\big)$, the slope of the elastic cross section is a simple function of the impact parameter amplitude [42],

$$B_{\mathrm{el}}(s, t=0) = \frac{\int \mathrm{d}^2b\, b^2 \mathcal{A}(s, b^2)}{2\int \mathrm{d}^2b\, \mathcal{A}(s, b^2)}\,. \tag{1.8}$$

The elastic slope is thus proportional to the squared impact parameter weighted by $\mathcal{A}(s, b)$,

$$B_{\mathrm{el}}(s, t=0) = \frac{1}{2}\big\langle b^2 \big\rangle\,. \tag{1.9}$$

In a recent measurement of the elastic cross section in proton-proton collisions at 8 TeV, a slope of $(19.9 \pm 0.3)\,\mathrm{GeV}^{-2}$ was found [43]. In fact, this value corresponds to $\langle b^2\rangle^{1/2} \approx 1.2\,\mathrm{fm}$, which is of the order of the proton charge radius, 0.9 fm [44].

1.3 Regge poles

Regge theory was originally formulated in the framework of nonrelativistic potential scattering [45] and later extended to higher energies [46]. It describes the asymptotic behaviour of two-body scattering amplitudes in the Regge limit, where $s \gg |t|$.

The scattering amplitude for a process $a + b \to c + d$ can be expanded in partial waves,

$$\mathcal{A}(s, t) = \sum_{\ell=0}^{\infty} (2\ell + 1)\, a_\ell(t)\, P_\ell(1 + 2s/t)\,, \tag{1.10}$$

where a_ℓ are the partial wave amplitudes and P_ℓ are the Legendre polynomials. Equation (1.10) can be obtained from crossing symmetry

starting with a conventional partial wave expansion of the crossed process, $a + \bar{c} \to \bar{b} + d$. Here the external masses are assumed to be small compared to the centre-of-mass energy. The index ℓ denotes the orbital angular momentum exchanged in the t-channel. Equation (1.10) can be written as a contour integral in the complex ℓ-plane. For that purpose two analytic functions, $a^{(\tau)}(\ell, t)$ with $\tau = \pm 1$, are introduced, the analytic continuations of the even and odd partial wave amplitudes to complex values of ℓ. They have to be treated separately to ensure the continuation to be unique. The parameter τ is called signature.

In the limit $s \gg |t|$ this contour integral can be expressed in terms of the residues of $a^{(\tau)}(\ell, t)$ at possible poles located at $\ell = \alpha_n{}^{(\tau)}(t)$, the Regge poles. Provided there are only simple poles, the dominant contribution to the amplitude is due to the rightmost Regge pole in the complex ℓ-plane, i.e. the one with the highest real part. We denote the location, residue and signature of this pole by $\alpha(t)$, $\beta(t)$ and τ, respectively. One finds a power-like asymptotic s-dependence of the amplitude,

$$\mathcal{A}(s,t) \xrightarrow{s\to\infty} \beta(t)\,\eta(t)\left(\frac{s}{s_0}\right)^{\alpha(t)}, \quad s_0 = 1\,\mathrm{GeV}^2, \tag{1.11}$$

with the signature factor

$$\eta(t) = -\frac{1 + \tau\,\mathrm{e}^{-\mathrm{i}\pi\alpha(t)}}{\sin\pi\alpha(t)}\,. \tag{1.12}$$

Positive values of t are unphysical in an s-channel process, $a + b \to c + d$. The amplitude of the respective process crossed to the t-channel, $a + \bar{c} \to \bar{b} + d$, however, should have poles corresponding to physical particles or resonances. From a particle with mass m and spin j one expects a pole in the amplitude at $\alpha\left(t = m^2\right) = j$. The function $\alpha(t)$, which interpolates the resonances, is called Regge trajectory or reggeon. Regge trajectories corresponding to mesons with identical quantum numbers (apart from spin) were found to be linear [47],

$$\alpha(t) = \alpha(0) + \alpha' t\,, \tag{1.13}$$

where $\alpha(0)$ is called the intercept and α' the slope of the reggeon. It can be shown that (1.13) holds for negative t as well.

Hence the asymptotic s-channel behaviour (1.11) is due to the exchange of families of resonances, collectively denoted as reggeons in the crossed channel. The residue function $\beta(t)$ in (1.11) can be factorized

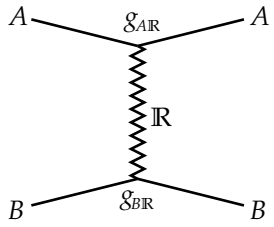

Figure 1.1: Diagram representation of the single-reggeon exchange approximation (1.14) of the elastic amplitude in high-energy AB scattering.

to coupling constants of the reggeon $\mathbb{R}$ to the two scattering particles A and B (Fig. 1.1),

$$\mathcal{A}(s,t) = s_0\, g_{A\mathbb{R}}(t)\, g_{B\mathbb{R}}(t)\, \eta(t) \left(\frac{s}{s_0}\right)^{\alpha(t)} . \tag{1.14}$$

1.4 The pomeron

The asymptotic behaviour of the total cross section due to reggeon exchange,

$$\sigma_{\text{tot}}^{\mathbb{R}} \propto \left(\frac{s}{s_0}\right)^{\alpha(0)-1} \quad \text{for } s \to \infty\,, \tag{1.15}$$

is easily derived from (1.3) and (1.11). The intercepts $\alpha(0)$ of mesonic Regge trajectories do not exceed about 0.5, thus resulting in asymptotically vanishing total cross sections. In experiments, however, total cross sections have been seen to rise slowly as centre-of-mass energy increases. This rise implies the existence of a Regge trajectory with intercept greater than one. This trajectory, the pomeron, dominates the scattering amplitude at high energies.

The original Donnachie-Landshoff parametrization [48] describes the s-dependence of the total proton-proton and proton-antiproton cross sections by means of a pomeron and an effective reggeon term; the pomeron intercept takes the value $\alpha_{\mathbb{P}}(0) = 1.0808$. Another, more recent fit [49], where the leading meson trajectories are treated separately [50], indicates a somewhat higher value, $\alpha_{\mathbb{P}} \approx 1.096$. Current LHC measurements at 8 TeV agree well with the latter parametrization [43].

In this work we make use of an important property of the pomeron: it couples with the same strength to particles and their antiparticles.

This equality is due to the pomeron carrying quantum numbers of the vacuum, for instance even parity and vanishing isospin. Furthermore it can be shown that the pomeron has even signature, $\tau = +1$. Thus the signature factor (1.12) at zero momentum transfer is $\eta(0) = \mathrm{i}$, where we approximate the pomeron intercept by 1. Hence the single-pomeron exchange amplitude for proton-proton scattering coincides with the respective proton-antiproton amplitude. At $t = 0$ it is purely imaginary and reads

$$\mathcal{A}_{\mathbb{P}}(s,0) = \mathrm{i} s_0 \, g^2_{\mathrm{p}\mathbb{P}}(0) \left(\frac{s}{s_0}\right)^{\alpha_{\mathbb{P}}(0)} . \tag{1.16}$$

As the theory of strong interactions, Quantum Chromodynamics is supposed to explain all aspects of hadron interactions at high energies where electroweak effects are irrelevant. Particularly, we can expect the high-energy behaviour of the total hadronic cross section and hence the pomeron to be subject to QCD.

The Balitsky-Fadin-Kuraev-Lipatov (BFKL) equation [51–54] determines the properties of the pomeron in perturbative Quantum Chromodynamics (pQCD). The BFKL pomeron is constructed of t-channel ladders consisting partly of so-called reggeized gluons [39]. In this connection, a particle is said to *reggeize* if its exchange in the t-channel results in an asymptotic s-dependence as in (1.11) and if the particle itself lies on the corresponding trajectory $\alpha(t)$.

However, pQCD applies only in a regime where high energy scales appear and the strong coupling constant vanishes asymptotically. Hence, elastic scattering at small momentum transfer cannot completely be understood within this framework. The BFKL approach to the pomeron is still an active field of research and is reviewed for instance in Ref. [39]. In this work, however, we are not concerned with the field theoretical description of the pomeron.

1.5 Multi-reggeon amplitudes

The exchange of multiple reggeons in the t-channel is an important contribution to scattering amplitudes at high energies. Multi-reggeon exchange results in branch cuts in the complex angular momentum plane. A general method to evaluate diagrams containing Regge cuts is the reggeon calculus proposed by Gribov [55]. This method allows to obtain multi-reggeon diagrams in the Regge limit by means of Feynman

(a) (b)

Figure 1.2: Diagrams of n-pomeron exchange amplitudes. (a) Full amplitude. The blobs represent all possible interactions of n pomerons with the scattering particles. (b) Elastic-rescattering approximation with on-shell intermediate states.

diagrams, using

$$\eta(\boldsymbol{k}^2)\left(\frac{s}{s_0}\right)^{\alpha(\boldsymbol{k}^2)} \tag{1.17}$$

as reggeon propagator [41].

To motivate the eikonal model, a closer look at the n-pomeron amplitude is helpful. Applying reggeon calculus and taking into account only elastic intermediate states (Fig. 1.2), this amplitude can be written in the *eikonal* form [56]

$$\begin{aligned}\mathcal{A}^{(n)}(s,t) = \frac{\mathrm{i}^{n-1}}{n!}\frac{1}{(2s)^{n-1}}(2\pi)^2\int\frac{\mathrm{d}^2\boldsymbol{k}_{1\perp}}{(2\pi)^2}\cdots\int\frac{\mathrm{d}^2\boldsymbol{k}_{n\perp}}{(2\pi)^2}\\ \times\,\mathcal{A}^{(1)}(s,\boldsymbol{k}_{1\perp}^2)\ldots\mathcal{A}^{(1)}(s,\boldsymbol{k}_{n\perp}^2)\,\delta^{(2)}\left(\boldsymbol{q}_\perp-\sum_{i=1}^{n}\boldsymbol{k}_{i\perp}\right),\end{aligned} \tag{1.18}$$

where $\boldsymbol{k}_{i\perp}$ denote the two-dimensional transverse momenta of the pomerons. The amplitude for several exchanged pomerons can thus be expressed in terms of the single-pomeron amplitude. As we will see below in Sec. 1.7, this relation simplifies further in impact parameter space.

1.6 AGK cutting rules

The optical theorem (1.3) relates the total cross section to the imaginary part of the forward scattering amplitude. Assuming the pomeron can be interpreted as ladders of particles in a more fundamental field theory,

the imaginary part of a single-pomeron diagram can then be taken as the unitarity cut through the particle ladders, hence forcing the cut "rungs" to be on their mass shell. In particular, final-state particles corresponding to a cut pomeron obey multi-peripheral kinematics [57], i.e. they are strongly ordered in rapidity.

The Abramovsky-Gribov-Kancheli (AGK) cutting rules [58] allow to obtain cross sections for final states corresponding to diagrams with several pomerons. These rules assign weights for asymptotically non-vanishing contributions to the imaginary part of the amplitude. These enhanced contributions are due to unitarity cuts passing *completely* through k pomerons in an n-pomeron diagram, where $0 \leq k \leq n$. For large s, only completely cut pomerons contribute to the total cross section. A cut through k pomerons contributes to the cross section σ_k for k multi-peripheral particle production subprocesses.

The n-pomeron forward elastic scattering amplitude contributes with a term $B_k^n \operatorname{Im} \mathcal{A}^{(n)}(s, t = 0)$ (in the sense of the optical theorem) to σ_k, where the AGK factors read [59]

$$B_k^n = \begin{cases} (-1)^{k-1} 2^{n-1} \binom{n}{k} & \text{if } 1 \leq k \leq n\,, \\ 1 - 2^{n-1} & \text{if } k = 0\,. \end{cases} \tag{1.19}$$

These factors can be derived by analysing the aforementioned nonvanishing unitarity cuts of the n-pomeron amplitude (1.18), where counting factors are included in order to account for all possibilities to cut a subset of all pomerons. The AGK factors (1.19) resolve the partial contribution of the n-pomeron amplitude to the cross sections for k cut pomerons. The total absorptive part of the amplitude, however, is retained,

$$\sum_{k=0}^{n} B_k^n = 1\,. \tag{1.20}$$

1.7 Eikonal model

In impact parameter space the n-pomeron amplitude in the elastic-rescattering approximation (1.18) can be written compactly in terms of the Born amplitude [56],

$$\mathcal{A}^{(n)}(s, b) = \frac{1}{2\mathrm{i}} \frac{\big(-\chi(s, b)\big)^n}{n!}\,, \tag{1.21}$$

with the *eikonal function*

$$\chi(s, b) = -2\mathrm{i}\mathcal{A}^{(1)}(s, b)\,, \tag{1.22}$$

which is real-valued due to (1.16). The absorptive parts of all multi-pomeron amplitudes with exactly k cut pomerons add up to

$$\sum_{n=k}^{\infty} B_k^n \operatorname{Im} \mathcal{A}^{(n)}(s,b) = \frac{(2\chi)^k}{4k!} \exp(-2\chi) , \tag{1.23}$$

where we use the AGK rules (1.19) for $k > 0$. In (1.23) and throughout we implicitly understand χ as a function of s and b. Using (1.3) and (1.4) one obtains finally the cross section for k cut pomerons in the eikonal model,

$$\sigma_k(s) = \int \mathrm{d}^2 b \frac{(2\chi)^k}{k!} \exp(-2\chi) . \tag{1.24}$$

The integrand in (1.24) is the Poisson probability for k, given 2χ on average. Hence we can interpret $2\chi(s,b)$ as the average subprocess multiplicity density in impact parameter space if we assume uncorrelated scatters. Adding up all cross sections with at least one cut pomeron, one finds the inelastic cross section,

$$\sigma_{\text{inel}}(s) = \sum_{k=1}^{\infty} \sigma_k(s) = \int \mathrm{d}^2 b \left(1 - \mathrm{e}^{-2\chi}\right) . \tag{1.25}$$

The sum of all impact parameter amplitudes with one or more exchanged pomerons is the total elastic amplitude,

$$\mathcal{A}(s,b) = \frac{\mathrm{i}}{2} \left(1 - \mathrm{e}^{-\chi}\right) . \tag{1.26}$$

Accordingly, the total cross section (1.6) reads

$$\sigma_{\text{tot}}(s) = 2 \int \mathrm{d}^2 b \left(1 - \mathrm{e}^{-\chi}\right) . \tag{1.27}$$

All unitarity cuts passing through *no* pomeron contribute to the cross section for elastic scattering,

$$\begin{aligned} \sigma_{\text{el}}(s) &= 4 \int \mathrm{d}^2 b \sum_{n=1}^{\infty} B_0^n \operatorname{Im} \mathcal{A}^{(n)}(s,b) \\ &= \int \mathrm{d}^2 b \left(1 - \mathrm{e}^{-\chi}\right)^2 , \end{aligned} \tag{1.28}$$

in accordance with (1.6) and (1.26). In the eikonal model the slope of the elastic cross section (1.8) reads

$$B_{\text{el}}(s, t=0) = \frac{1}{\sigma_{\text{tot}}(s)} \int \mathrm{d}^2 b \, \boldsymbol{b}^2 \left(1 - \mathrm{e}^{-\chi}\right) , \tag{1.29}$$

with the eikonalized total cross section σ_{tot} from (1.27).

Chapter 2

Multiple parton interactions

A wide range of soft inclusive observables in high-energy hadron collisions can be described by multiple parton interactions (MPI), as first studied in Ref. [3]. There is also direct evidence for the production of multiple *uncorrelated* scatters in hadron collisions [60]. All major Monte Carlo event generators—Herwig++ [4], Pythia [5, 6] and Sherpa [7]—feature MPI models to simulate soft inclusive events and the underlying event in the presence of a hard process. For a recent review of Monte Carlo event generators we refer to Ref. [9].

In this chapter we review the physics of the multiple-parton interaction model in Herwig++ [4, 10, 61] and relate it to the eikonal formalism established in the previous chapter. We discuss the implementation of soft and hard parton subprocesses with focus on hadronization.

2.1 Multiple hard interactions

The inclusive jet production cross section above a fixed transverse momentum is calculated within perturbative QCD according to

$$\begin{aligned}\sigma_{\mathrm{H}}^{\mathrm{inc}}(s, p_{\mathrm{T}}^{\mathrm{min}}) = \int \mathrm{d}x_1\, \mathrm{d}x_2\, \mathrm{d}\hat{t}\, \Theta\Big(p_{\mathrm{T}} - p_{\mathrm{T}}^{\mathrm{min}}\Big) \sum_{i,j,k,l} \frac{1}{1+\delta_{kl}} \\ \times \left(f_{i|h_1}(x_1, \mu^2) f_{j|h_2}(x_2, \mu^2) \frac{\mathrm{d}\hat{\sigma}_{ij\to kl}}{\mathrm{d}\hat{t}}\left(x_1 x_2 s, \hat{t}\right) \right),\end{aligned} \tag{2.1}$$

where the sums run over all partons and $f_{p|h}$ denotes the parton distribution function (PDF) of a parton p in a hadron h. Due to high values of the PDFs at small momentum fractions x, the hadronic cross section $\sigma_{\mathrm{H}}^{\mathrm{inc}}$ rises with the centre-of-mass energy s.

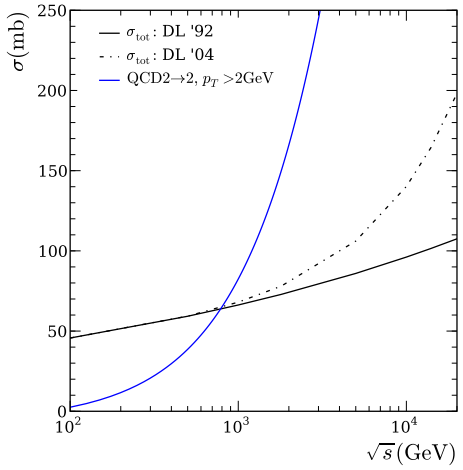

Figure 2.1: Inclusive jet production cross section above 2 GeV, compared to the total pp scattering cross section. Taken from Ref. [63].

The inclusive cross section (2.1) exceeds the measured total cross section at moderate centre-of-mass energies, see Fig. 2.1. This alleged contradiction is resolved by understanding $\sigma_{\text{H}}^{\text{inc}}$ as the jet production cross section in respect of the luminosity of incoming *partons* [62]. Multiple parton interactions thus unitarize the jet cross section.

MPI cross sections are calculated within an eikonal model as introduced in Sec. 1.7, thus taking advantage of the phenomenologically successful description of cross sections in Regge theory. To embed multiple QCD interactions in the eikonal framework, the parton luminosity is assumed to factorize into an impact parameter-dependent factor and the usual PDFs. Furthermore, *uncorrelated* multiple parton interactions are assumed. With these assumptions the average multiplicity at fixed impact parameter factorizes into the hard inclusive cross section, as defined in (2.1), and a factor describing the impact parameter dependence [10],

$$\langle n \rangle(s, b) = A(b)\, \sigma_{\text{H}}^{\text{inc}}(s, p_{\text{T}}^{\text{min}})\,, \tag{2.2}$$

where the overlap function $A(b)$ must satisfy [62]

$$\int \mathrm{d}^2 b\, A(b) = 1\,. \tag{2.3}$$

The overlap function is parametrized in the HERWIG++ MPI model as

$$A(b, \mu) = \frac{\mu^2}{96\pi} (\mu b)^3\, K_3(\mu b)\,, \tag{2.4}$$

where K_3 is the modified Bessel function of the third kind and μ a free parameter.

The cross section for jet production due to k uncorrelated interactions is the Poisson probability for k interactions with an average multiplicity given by (2.2), integrated over all impact parameter space,

$$\sigma_k(s) = \int \mathrm{d}^2 b \, \frac{(A\,\sigma_{\mathrm{H}}^{\mathrm{inc}})^k}{k!} \exp(A\,\sigma_{\mathrm{H}}^{\mathrm{inc}}) \,. \tag{2.5}$$

This expression coincides with its equivalent in the eikonal formalism, (1.24), if the eikonal function is identified as

$$\chi_{\mathrm{H}}(s,b) = \frac{1}{2} A(b,\mu)\, \sigma_{\mathrm{H}}^{\mathrm{inc}}(s, p_{\mathrm{T}}^{\mathrm{min}}) \,. \tag{2.6}$$

The bare hard MPI model has therefore two main parameters directly impacting the MPI multiplicity (2.2), $p_{\mathrm{T}}^{\mathrm{min}}$ and μ.

Multiple hard subprocesses, which correspond to cut pomerons in the eikonal formalism, are implemented as independent dijet processes with transverse momentum greater than $p_{\mathrm{T}}^{\mathrm{min}}$. To that end, parton scatters are generated according to QCD matrix elements and parton showers are generated.

2.2 Soft interactions

The hard MPI model allows a good description [10] of the underlying event in $\mathrm{p\overline{p}}$ events where the leading jet has a transverse momentum greater than 20 GeV [64]. This model, however, cannot describe low-p_{T} jet production. The extension of the hard model to a soft inclusive model introduces multiple independent soft scatters with $p_{\mathrm{T}} < p_{\mathrm{T}}^{\mathrm{min}}$ [8, 61].

As proposed in Ref. [65], the eikonal function is then taken as the sum of the hard eikonal function (2.6) and a soft eikonal function,

$$\begin{aligned} \chi(s,b) &= \chi_{\mathrm{H}}(s,b) + \chi_{\mathrm{S}}(s,b) \\ &= \frac{1}{2}\Big[A(b,\mu)\, \sigma_{\mathrm{H}}^{\mathrm{inc}}(s, p_{\mathrm{T}}^{\mathrm{min}}) + A(b,\mu_{\mathrm{S}})\, \sigma_{\mathrm{S}}^{\mathrm{inc}} \Big] \,, \end{aligned} \tag{2.7}$$

where (2.5) is generalized to the cross section for j soft and k hard uncorrelated interactions,

$$\sigma_{jk}(s) = \int \mathrm{d}^2 b \, \frac{(2\chi_{\mathrm{S}})^j}{j!} \frac{(2\chi_{\mathrm{H}})^k}{k!} \exp[-2\,(\chi_{\mathrm{S}} + \chi_{\mathrm{H}})] \,. \tag{2.8}$$

The soft cross section, $\sigma_{\mathrm{S}}^{\mathrm{inc}}$, is assumed to be a bare nonperturbative cross section and hence not calculable in perturbation theory. Instead,

σ_S^{inc} and the other new parameter, μ_S, are determined in a fit to experimental data: the eikonal approximations of the total cross section (1.27) and the elastic slope (1.29), obtained with the total eikonal function (2.7), are required to be compatible with experimental data [61]. This fit is performed in the beginning of each run once the hard eikonal function is determined by the model parameters μ, p_T^{min} and the PDF choice.

For the Monte Carlo implementation of soft interactions, matrix element calculations cannot be used since perturbative QCD does not apply in the soft regime. Instead, generic gluon-gluon interactions with $p_T < p_T^{\text{min}}$ are generated. The differential p_T distribution of the soft cross section is chosen in such a way as to match the perturbative distribution $\mathrm{d}\sigma_H^{\text{inc}} / \mathrm{d}p_T^2$ at $p_T = p_T^{\text{min}}$ [8].

2.3 Monte-Carlo implementation

2.3.1 Large-N_C limit

Quantum Chromodynamics is an SU(3) gauge theory. Some parts of the event generation, however, simplify if formulated in an SU(N_C) gauge group, where N_C is considered large [9]. In this limit, the dominant part of the full colour index structure of QCD diagrams in the perturbation expansion in $1/N_C$ can be represented in planar form using colour lines [66]. Most notably this implies that the adjoint colour of the gluon is compound of a fundamental and an antifundamental colour.

There are implementations of final-state parton showers based on full SU(3) colour correlations [67]. The corrections due to subleading contributions, however, were found to be small in event shapes and jet shape observables at LEP.

2.3.2 Cluster hadronization

The evolution of jets in perturbative interactions via parton showers results in a preconfined stage, where the invariant mass of pairs of partons connected by colour lines in the large-N_C limit is low [34]. The cluster hadronization model [1], which is with some variations also used in HERWIG++ [4], acts on events at the preconfined stage.

The transition from parton jets to hadron jets is performed in several steps. First, gluons are split up nonperturbatively into light $q\bar{q}$ pairs. The splitting happens isotropically in the gluon rest frame, where the partons are taken as nonperturbative objects with constituent mass [9].

After the gluon splitting, any particle has exactly one colour partner in the large-N_C approximation. These colour-connected particle pairs are called (primary) clusters.

The universality of the cluster hadronization model becomes apparent in the invariant-mass distribution of primary clusters. In e^+e^- annihilation at different centre-of-mass energies this distribution is independent of the hard energy scale [1, 68]. With model parameters tuned to LEP data, the primary-cluster mass distribution in e^+e^- runs is strongly populated at values close to the parton shower cutoff, $\mathcal{O}(1\,\mathrm{GeV})$. These clusters are decayed into hadrons, where flavours and other quantum numbers are selected according to well-motivated models. Clusters too light to decay into two hadrons are converted in single hadrons. Heavy clusters with masses more than a few GeV are not decayed into hadrons directly since that would result in unreasonably highly boosted particles. Instead, these clusters are fissioned into lighter ones, which in turn are either fissioned further or decayed to hadrons.

2.3.3 Hadronization in hadron collisions

The colour structure in hadron collisions is more complicated. Parton interactions with high momentum transfer are governed by perturbative QCD, where colour preconfinement can be assumed to be valid. However, hadrons are compound of colour-charged constituents, which may contribute to particle production also at nonperturbative energy scales.

The diagram in Fig. 2.2 shows the colour topology in an exemplary event with multiple hard subprocesses. At short length scales, these subprocesses are assumed to be uncorrelated. As indicated, the implementation makes use of colour lines also in the nonperturbative phase prior to initial-state parton showers. These colour lines entail clusters that connect different parton subprocesses, giving rise to joint particle production by multiple parton interactions. Furthermore, the beam remnants are colour-charged as well and hence subject to hadronization.

The MPI model allows for two possibilities to create colour connections in soft subprocesses: soft scatters can either be disrupted from the rest of the event (as far as formation of clusters is concerned) or they are colour-connected to the hadron remnants. The model parameter p_{disrupt} steers the probability for disruption of colour lines in soft scatters. The example diagram in Fig. 2.3 shows disrupted colour lines between the beam remnants and the emitted gluons.

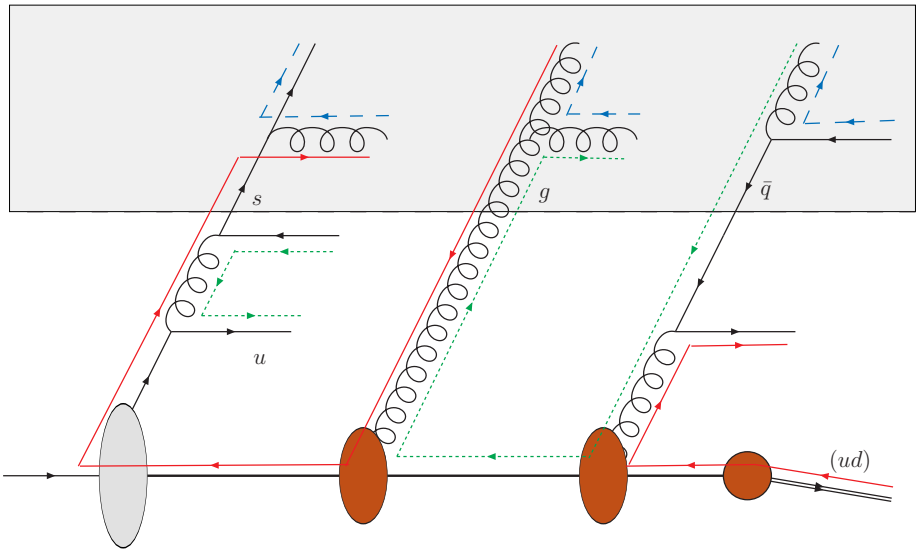

Figure 2.2: Colour structure in a hadron collision with multiple hard interactions. Taken from Ref. [10].

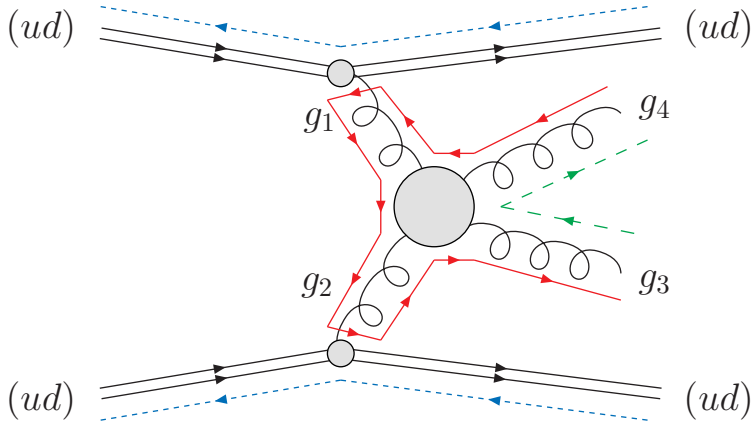

Figure 2.3: Colour structure in soft scatters. Taken from Ref. [4].

Chapter 3

Colour reconnections

This chapter covers the first part of the present work, the implementation and analysis of colour reconnections in the event generator Herwig++. We start with a discussion of the limitations of the bare MPI model and motivate the need for colour reconnections from a phenomenological point of view. Then we describe the implementation details of two colour reconnection models that have been developed in this thesis. Here we focus also on a theoretical motivation for the model ideas. Furthermore, we discuss the effects of colour reconnections on observables at parton level and continue with the validation of the models against LEP data. In comparisons to minimum-bias and underlying-event data from the Tevatron and the LHC, we finally show that colour reconnections improve the nondiffractive soft inclusive and underlying-event models in Herwig++.

Parts of the work described in this chapter are published in *Eur.Phys.J. C72 (2012), p. 2225* [69] and in a number of proceedings, [70–74].

3.1 Limitations of the bare MPI model

The bare multiple-parton interaction model was validated in Ref. [63] against underlying-event data from the Tevatron from Ref. [64]. The considered observables were

- the average charged-particle multiplicity and
- the average scalar p_{T} sum of charged particles,

both as function of the transverse momentum of the leading charged-particle jet, $p_{\mathrm{T}}^{\mathrm{lead}}$. To increase the sensitivity to the underlying event, these observables were measured in kinematic regions that are defined

by the azimuthal angle relative to the leading jet [64]. After tuning of the model parameters, good agreement with the data was found: the MPI model describes the aforementioned observables in all kinematic regions, also in events with only rather soft jets, $p_{\mathrm{T}}^{\mathrm{lead}} < 20\,\mathrm{GeV}$ [63].

The bare MPI model, however, is incompatible (Fig. 3.1) with early minimum-bias data at $\sqrt{s} = 900\,\mathrm{GeV}$ from ATLAS, published in Ref. [11]. This measurement includes observables the MPI model has not been tested with before, e.g. the pseudorapidity distribution of charged particles. Using the default tune of the MPI model in HERWIG++ 2.4.2, i.e. the Tevatron tune mentioned above, we see a notable dependence on the parameter p_{disrupt}. This parameter steers the choice of colour connections in soft parton scatters (see Sec. 2.3.3). Particularly the pseudorapidity distribution of charged particles is sensitive to soft colour connections. With the default value, $p_{\mathrm{disrupt}} = 1$, the colour lines in soft scatters are disrupted from the rest of the event. This disruption leads to a depletion of particle production at central rapidities, $|\eta| < 1.5$, which is in contrast do ATLAS data (Fig. 3.1(a)). All settings, however, give a good description of underlying-event data from the Tevatron. Also a dedicated tuning of the MPI model parameters does not improve the description of minimum-bias data from the LHC [70, 76, 77]. This dependence on the soft colour disruption hints at the importance of colour correlations in a more complete model.

3.2 Implementation

As discussed in Sec. 2.3.3, the multiple-parton interaction model introduces colour lines that connect parton subprocesses to each other and to the hadron remnants. As a result, clusters emerge that link different parts of the hadron collision. Since preconfinement applies only to perturbative jet production, these clusters cannot be expected to feature the same invariant-mass distribution as clusters in dijet production in e^+e^-.

The colour reconnection models studied in this work intervene into the event generation at the stage immediately *before* hadrons are generated from clusters. The models provide the possibility to create clusters in a way that does not strictly follow the actual colour topology: the ends of colour lines can be reconnected, hence resulting in a different cluster configuration (Fig. 3.2). Motivated by the successful role of preconfinement in e^+e^- collisions, we designed the colour reconnection procedure to create clusters with invariant masses lower than the masses of the

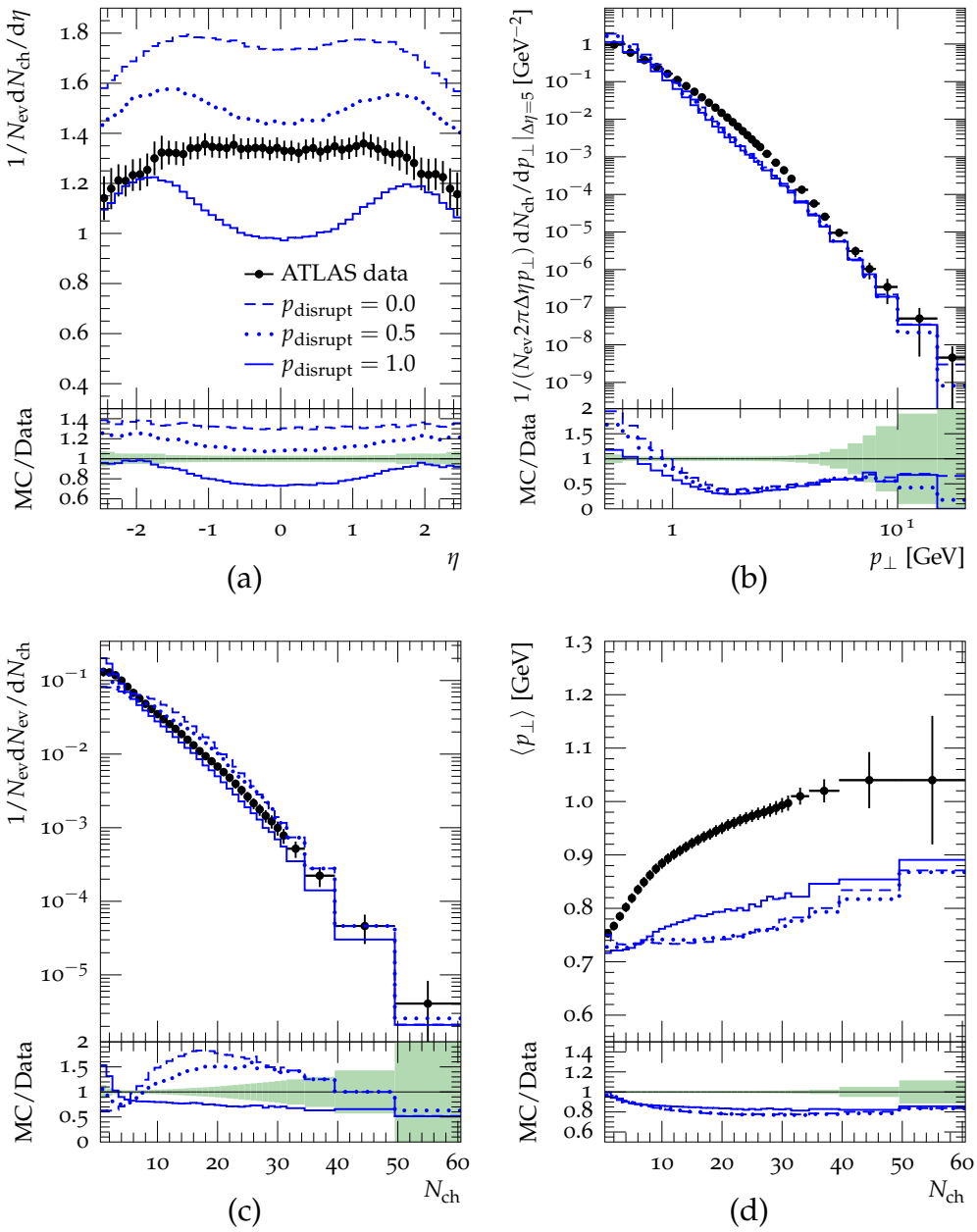

Figure 3.1: Comparison of Herwig++ 2.4.2 to ATLAS minimum-bias distributions at $\sqrt{s} = 0.9\,\text{TeV}$ with $N_{\text{ch}} \geq 2$, $p_{\text{T}} > 500\,\text{MeV}$ and $|\eta| < 2.5$ from Ref. [11]. The Herwig++ results are obtained with a Tevatron tune of the MPI model (see text). The results differ in the parameter p_{disrupt}, the probability for colour disruption of soft scatters. (a) Charged-particle pseudorapidity distribution. (b) Charged-particle transverse momentum distribution. (c) Charged-particle multiplicity distribution. (d) Average transverse momentum of charged particles as a function of the number of charged particles, N_{ch}.

Rivet [75] analysis ID: ATLAS_2010_S8591806

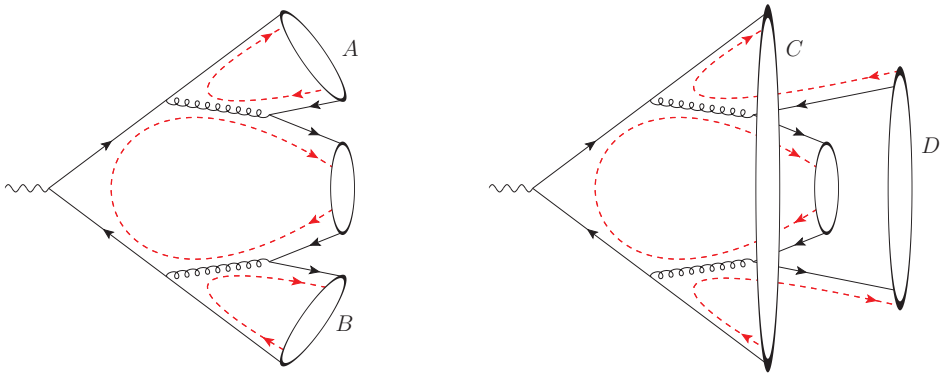

Figure 3.2: Formation of clusters from partons. Colour lines are dashed. The left diagram shows colour-singlet clusters formed according to the dominating colour structure in the $1/N_C$ expansion. The right diagram shows a possible colour-reconnected state: the partons of the clusters A and B are combined in new clusters, C and D.

original clusters. The colour reconnection models studied in this thesis differ only in the algorithm to find alternative cluster configurations.

In the description of the colour reconnection algorithms and the subsequent discussion we often encounter the sum of the invariant masses of all clusters,

$$\lambda = \sum_{i=1}^{N_{\mathrm{cl}}} m_i^2 \,, \tag{3.1}$$

where N_{cl} denotes the number of clusters in the event. We refer to this quantity as *colour length* in this work.

3.2.1 Plain colour reconnection model

The first model studied in this thesis uses a simple procedure to select the clusters that are to be reconnected. We refer to it as the *plain colour reconnection* model (PCR) in this thesis. An implementation of the PCR model is publicly available in HERWIG++ as of version 2.5 [78]. The PCR model applies the following algorithm to each event at the stage at which clusters have just been created:

0. Create a randomly ordered list of all colour triplets (quarks and anti-diquarks) in the event.[1] Perform the remaining steps once for every particle in this list.

1. The current quark is part of a cluster. Label this cluster A.

2. Consider a colour reconnection with all other clusters that exist at that stage. Label the possible reconnection partner B. For the possible new clusters C and D, which would emerge from a reconnection of A and B (cf. Fig. 3.2), the following conditions must be fulfilled:

   - The new clusters are lighter,

     $$m_C + m_D < m_A + m_B \,, \tag{3.2}$$

     where m_k denotes the invariant mass of cluster k.
   - C and D are no colour octets, i.e. do not consist of $q\bar{q}$ pairs produced in gluon splittings.

3. If at least one reconnection possibility was found in step 2, select the one that results in the *lowest* sum of cluster masses, $m_C + m_D$. Accept this colour reconnection with probability p_{reco}. If accepted, replace the clusters A and B by the new clusters C and D.

The parameter p_{reco} steers the strength of colour reconnection and is the only parameter in the PCR model. The iteration in the zeroth step is performed over quarks instead of clusters since the list of clusters changes if a reconnection is accepted in the third step. Because of the selection rule in step 3, the PCR model tends to replace the heaviest clusters by lighter ones.

The algorithm described above is, however, non-deterministic: a different order of the quarks in step 0 leads to different reconnection possibilities being tested. Furthermore, quarks and antiquarks are treated differently in this algorithm because of the iteration over colour triplets in the step 0.

3.2.2 Statistical colour reconnection model

The simple iteration over all colour triplets in the PCR model might bias the selection of cluster pairs for colour reconnection in one way or another. In order to understand whether Monte Carlo results depend on the actual algorithm according to which cluster pairs are selected, we study another model in this thesis. We construct this alternative

[1] For simplicity, we use the terms *quark* and *antiquark* here to refer to colour-charged particles (quarks and anti-diquarks, e.g. antiproton remnants [4]) and anticolour-charged particles (antiquarks and diquarks).

colour reconnection model in such a way that it overcomes the aforementioned conceptual shortcomings of the PCR model. We refer to this model as *statistical colour reconnection* (SCR) throughout this work. An implementation of the SCR model is available in HERWIG++ as of version 2.6 [79].

This algorithm is designed to find a cluster configuration with a preferably low colour length λ, defined in (3.1). In general, it is clearly impossible to locate the global minimum of λ: an event with 100 parton pairs, for instance, implies about $100! \approx 10^{158}$ possible cluster configurations to be tested. Hence we use the simulated-annealing algorithm [80] to solve this minimization problem approximately. The SCR model is an application of this algorithm with the colour length λ as the objective function to be minimized.

The SCR algorithm selects random pairs of clusters and suggests them for colour reconnection. Like in the PCR model, clusters consisting of splitting products of a colour-octet state are vetoed. A reconnection step that reduces λ is always accepted. If a reconnection step, however, would raise the colour length, this step is accepted with the probability

$$\exp\left(-\frac{\lambda_2 - \lambda_1}{T}\right), \tag{3.3}$$

where λ_1 and λ_2 denote the colour lengths before and after the reconnection, respectively. These λ-increasing steps allow the system to escape local minima in the colour length. The "temperature" T, which has the dimension of a mass squared, is a control parameter of the annealing algorithm. It is gradually reduced during the optimization procedure. At high temperatures, $T \geq \mathcal{O}(\lambda_2 - \lambda_1)$, the algorithm is likely to accept steps that raise λ. Low temperatures, on the other hand, imply a small probability for colour length-increasing reconnection steps.

The annealing schedule determines the transition from high to low temperatures. The starting temperature is determined from the typical change in the colour length, $\Delta\lambda = \lambda_2 - \lambda_1$. To this end, a few random dry-run colour reconnection steps S are performed, all starting with the default cluster configuration. The initial temperature is then set to

$$T_{\text{init}} \equiv t_0 \cdot \operatorname*{median}_{i \in S}\{|\Delta\lambda|_i\}, \tag{3.4}$$

where t_0 is a dimensionless free parameter of the model. Using the median instead of the mean value makes this definition less prone to outliers.

The algorithm proceeds in steps at fixed temperature. The annealing schedule was designed to flexibly adapt to the number of clusters N_{cl} in an event: The temperature T is held constant for $f_{\text{isotherm}} \cdot N_{\text{cl}}$ reconnection attempts, where f_{isotherm} is another free parameter. At the end of each temperature step, T is decreased to $f_{\text{anneal}} \cdot T$, where $f_{\text{anneal}} \in (0, 1)$ is another free model parameter. The algorithm stops as soon as no successful colour reconnections happen in a temperature step, but at most N_{steps} temperature steps are processed.

In total, the SCR model has four parameters, all related to the annealing schedule: t_0, f_{isotherm}, f_{anneal} and N_{steps}.

3.3 Results at parton level

The colour reconnection models described above affect the creation of clusters from partons. Hence the models can be expected to modify the kinematics of clusters. In this section we study observables at parton level (more precisely, the level at that the partons are combined in clusters) that allow to understand colour reconnection from an event generator-internal point of view.

The results in this section were obtained with realistic values for the model parameters: the parameters were determined in tunes to LHC data. The tuning procedure is described below in Sec. 3.5.

3.3.1 Colour length

To quantify the effect of colour reconnection at parton level, we define the colour length drop

$$\Delta_{\text{if}} = 1 - \frac{\lambda_{\text{final}}}{\lambda_{\text{init}}} \,, \tag{3.5}$$

where λ_{init} and λ_{final} denote the colour length (3.1) in an event before and after colour reconnection, respectively. The quantity Δ_{if} approximately vanishes in events with no or only minor changes in the colour length due to colour reconnection, where $\lambda_{\text{init}} \approx \lambda_{\text{final}}$. The other extreme, $\Delta_{\text{if}} \approx 1$, indicates a notable drop in the sum of squared cluster masses λ.

The distribution of Δ_{if} in soft inclusive LHC events is strongly peaked around the values 0 and 1 for both the plain and the statistical colour reconnection models (Fig. 3.3(a)). Only a small fraction of events populate the range between the peaks, $0.1 < \Delta_{\text{if}} < 0.9$. Hence we find two important classes of soft inclusive events. The first class consists

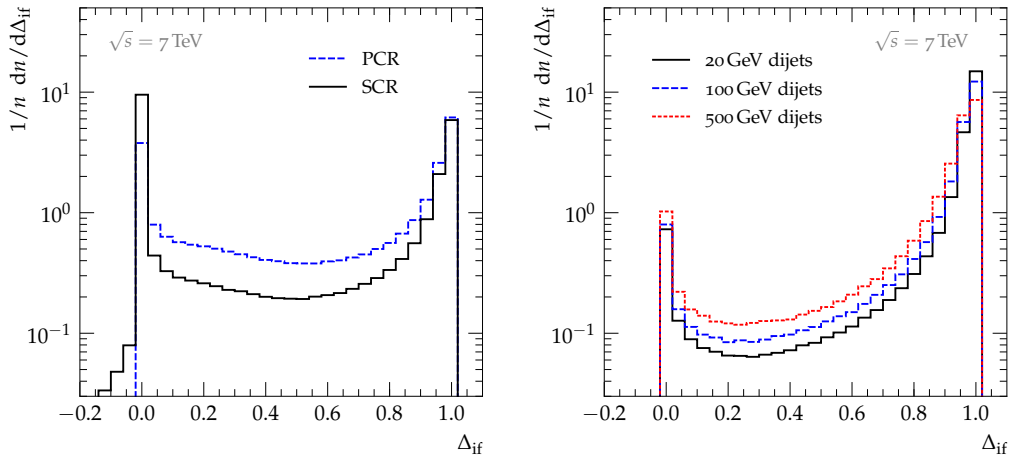

Figure 3.3: Colour length drop distributions in pp collisions at $\sqrt{s} = 7\,\mathrm{TeV}$. (a) Distribution in soft inclusive LHC events. One histogram for each colour reconnection model is shown. (b) Distribution in LHC dijet events with transverse momentum greater than 20, 100 and 500 GeV. The SCR model is used for this plot.

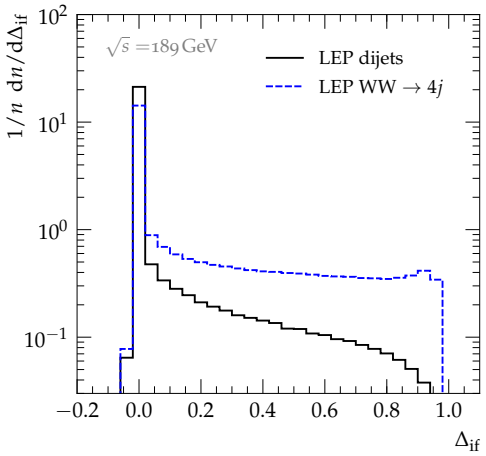

Figure 3.4: Colour length drop distribution in e^+e^- collisions at 189 GeV using the SCR model. The PCR model yields similar distributions. The histograms show the distribution in dijet events and in events with fully hadronically decaying W pairs.

of events where there is no notable change in the colour length due to colour reconnections. In another large fraction of events, however, colour reconnections reduce the colour length λ extremely. An obvious interpretation for this drop is that the colour reconnection procedure replaces disproportionally heavy clusters by way lighter ones.

There is also a small fraction of events with negative Δ_{if}, though. In these events the colour length is low *after* colour reconnection, as is apparent from (3.5). In the SCR algorithm, this can happen since λ-raising steps are explicitly allowed with probability (3.3). However, also the PCR algorithm can occasionally raise λ: in general, the condition (3.2) does not imply the sum of *squared* cluster masses to be higher after colour reconnection. As the fraction of events with negative Δ_{if} is small, however, we ignore this artefact.

Figure 3.3(b) shows the colour length drop distribution in hard dijet events in pp collisions. Independent of the jet p_{T} cut, large colour length drops, $\Delta_{\mathrm{if}} \approx 1$, are more frequent in hard events than in soft inclusive ones. However, the peak at $\Delta_{\mathrm{if}} \approx 1$ decreases with increasing cut on the jet p_{T}. The reason for this decrease is that higher momentum fractions are required for the hard dijet subprocess, whereas in soft events the remaining momentum fraction of the proton remnants is higher. Clusters containing a proton remnant are thus less massive in hard events and therefore less likely to be subject to colour reconnections.

The distribution of the colour length drop in $\mathrm{e}^+\mathrm{e}^-$ annihilation events looks different (Fig. 3.4). We find that the colour reconnection procedure has little impact on the colour length in the bulk of dijet events. These results confirm that the parton shower ends in most cases at a preconfined stage, at which colour singlets form light clusters. In hadronic WW pair production, however, hadrons emerge from two separate colour singlets. If the two parton jet pairs overlap in phase space, the production of hadrons is expected to be sensitive to colour reconnections. We address this question below in Sec. 3.4. Here we want to remark that the fraction of WW events with nonvanishing colour length drop is slightly higher than for the dijet case (Fig. 3.4). Nevertheless, also the majority of WW events is not affected by colour reconnection.

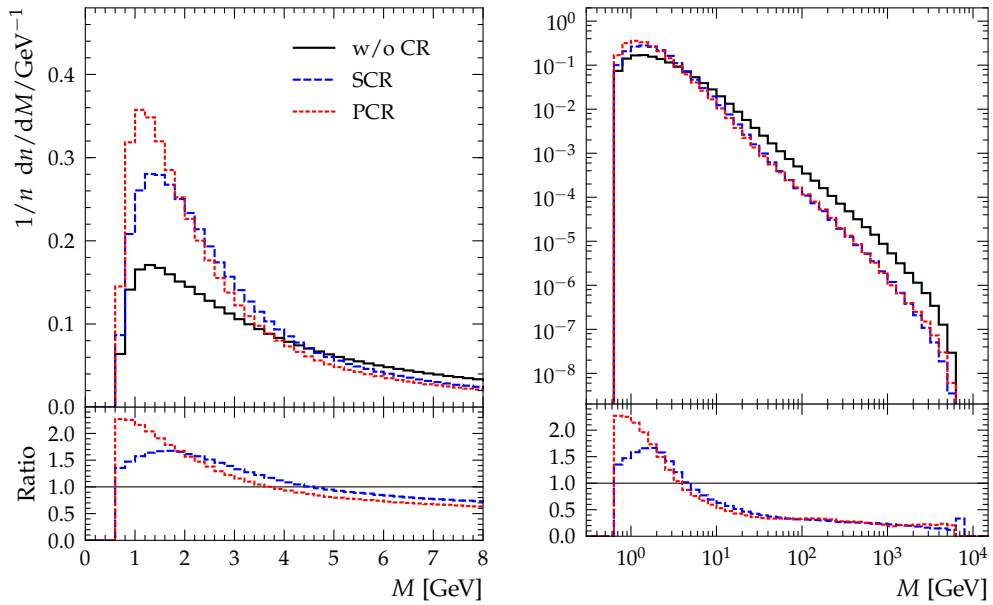

Figure 3.5: Invariant mass of primary clusters in soft inclusive LHC events at 7 TeV. The histograms are normalized to unity, where also invisible bins are taken into account. The histograms in the right plot are binned logarithmically.

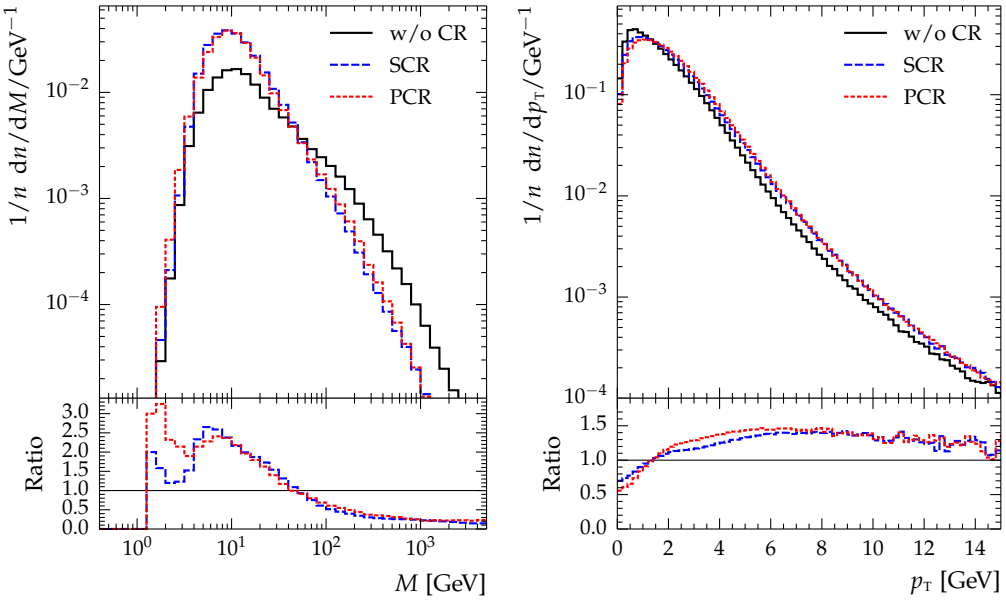

(a) (b)

Figure 3.6: Distributions of clusters in soft inclusive LHC events at 7 TeV. (a) Invariant mass distribution of the heaviest cluster. (b) Transverse momentum distribution of all clusters.

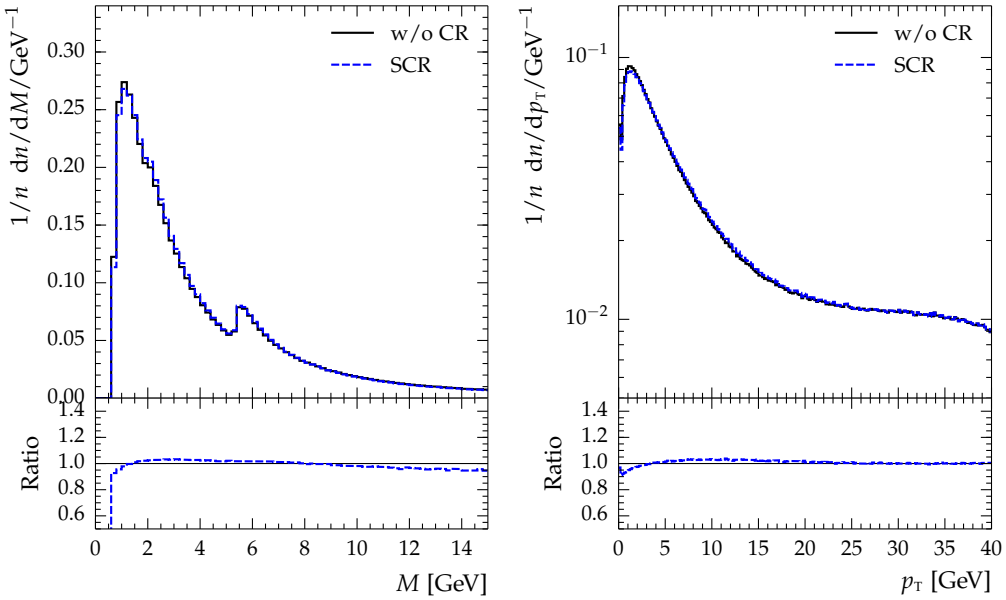

(a) (b)

Figure 3.7: Distribution of clusters in dijet production in e^+e^- collisions at 189 GeV. (a) Invariant-mass distribution. (b) Transverse-momentum distribution.

3.3.2 Differential distributions

The distribution of the invariant mass of clusters in soft inclusive LHC events is significantly changed by colour reconnection (Figure 3.5). As can be expected from the construction of the models, colour reconnections lead to an enhancement in the low-mass region, whereas higher masses are suppressed. We also see that the cluster mass distribution ranges to values of the order of the collider energy, $\sqrt{s} = 7\,\mathrm{TeV}$ in the given example. However, the relative fraction of clusters in that mass region is small.

The invariant mass of only the *heaviest* cluster in the event is distributed as shown in Fig. 3.6(a). The distribution without reconnections is strongly populated at $\mathcal{O}(10\,\mathrm{GeV})$ and ranges to the TeV region. Colour reconnection further enhances the region where the maximum cluster mass is $\mathcal{O}(10\,\mathrm{GeV})$.

The transverse momentum of the clusters is shifted to higher values in the presence of colour reconnection (Fig. 3.6(b)). We can understand this shift qualitatively: Consider two colour-connected partons with transverse momenta in opposite directions. The momentum of the resulting cluster is the vector sum of the parton momenta, so the transverse

components cancel partially. The colour reconnection algorithm tries to find parton pairs with lower invariant mass. The relative momentum of these parton pairs thus tends to be low, which implies less cancellation in the vector sum of the transverse momenta of the partons. Hence, clusters with higher p_T emerge.

The distributions of the invariant mass and transverse momentum in e^+e^- collisions, do not change much in the presence of colour reconnection (Fig. 3.7). Since colour reconnection barely affects the total colour length (see Sec. 3.3.1), strong effects in these distributions would even be surprising. From these observations we conclude that colour reconnection should have also no significant effect in e^+e^- collisions for observables at hadron level.

3.3.3 Classification of clusters

These results raise the question which mechanism in hadron event generation is responsible for heavy clusters. To gain access to this question, we classify all clusters by their ancestors in the event history (Fig. 3.8).

- The first class are the clusters consisting of partons emitted perturbatively in the same partonic subprocess. We refer to these clusters as *hard* clusters.

- The second class of clusters interconnect subprocesses. These clusters consist of partons generated perturbatively in different partonic subprocesses. We refer to them as *interconnecting* clusters.

- All remaining clusters contain at least one "nonperturbative constituent". We refer to these clusters as *nonperturbative* clusters in this thesis. In this connection, we mean by "nonperturbative constituent" either partons produced in soft scatters, or partons produced in nonperturbative splittings during the extraction of partons from remnants (for details see Ref. [10]), or the remnants themselves.

A bin-by-bin breakdown of the contributions of the three cluster classes to the total cluster mass distribution is shown in Fig. 3.9. We see that the relative contribution of hard clusters, which originate in single perturbative parton scatters, is high in the low-mass region. The high-mass tail, $M > \mathcal{O}(100\,\mathrm{GeV})$, on the other hand, is clearly dominated by the contribution of nonperturbative clusters. Hence, colour reconnection acts predominantly on clusters of nonperturbative origin.

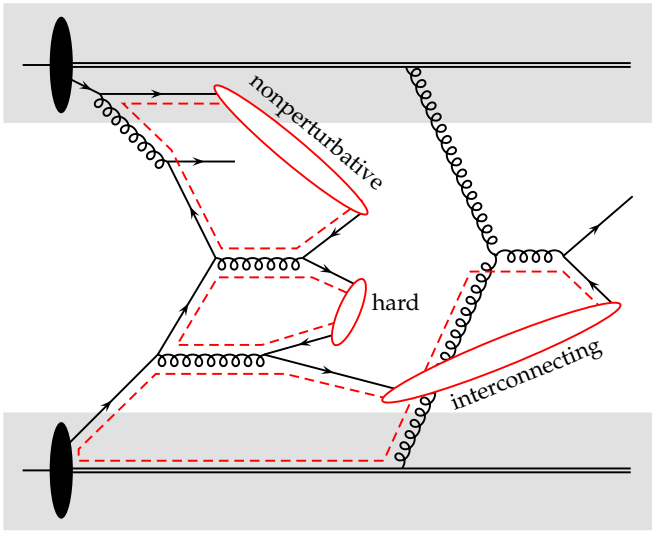

Figure 3.8: Classification of clusters in hadron collisions. The grey-shaded areas indicate nonperturbative parts of the event generation. The three indicated clusters represent the cluster classes that are defined in the text.

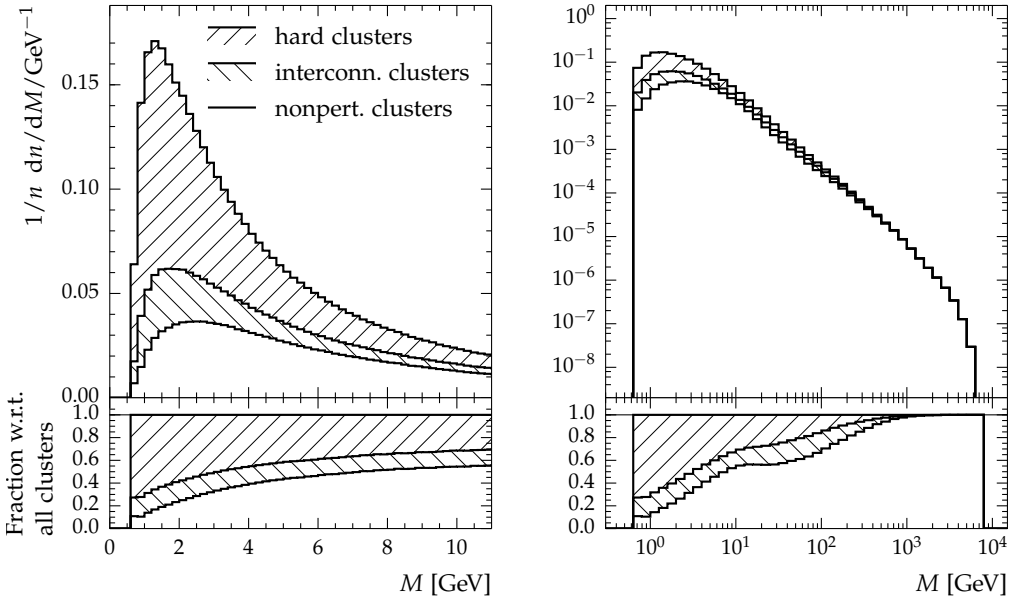

Figure 3.9: Relative contributions of the three cluster classes to the cluster mass distribution without colour reconnection in soft inclusive LHC events at 7 TeV. The histograms are stacked on top of each other. The histograms in the right plot are binned logarithmically.

3.3.4 Resulting physics implications

The observed properties of differential distributions at parton level clearly confirm the physical picture we have started out with. The colour reconnection model in fact reduces the invariant mass of clusters that are mostly of nonperturbative origin. These nonperturbative clusters arise as an artefact of the choice of nonperturbative colour connections of multiple parton interactions with the rest of the event.

At the nonperturbative level we have no handle on the colour information from theory. To account for a physical picture of the evolution of multiple jets in hadron collisions, we introduce nonperturbative colour reconnections, where we use colour preconfinement as a guiding principle.

3.4 Colour reconnections in e^+e^- collisions

We found in Sec. 3.3 that the colour length in e^+e^- events remains to a great extent unchanged by colour reconnections. Furthermore, we found only minor changes in the invariant-mass and transverse-momentum distributions of clusters due to colour reconnections. Based on these results we concluded that only little sensitivity to colour reconnection in e^+e^- observables at hadron level is to be expected.

3.4.1 Hadronization tune

Although colour reconnection certainly affects hadronization, we can expect that the default hadronization parameters are valid also in combination with colour reconnection. We confirm this expectation by comparing results with and without colour reconnection against a wide range of experimental data from LEP [81–89]. We find minor effects on event shape observables (Fig. 3.10(a)). The average multiplicity of charged particles in LEP runs is affected by colour reconnection (Fig. 3.10(b)). Within the experimental errors, however, the results with colour reconnection are also compatible with the experimental data. We conclude that the description of hadronization-related LEP data in HERWIG++ with and without colour reconnections is of the same quality.

3.4.2 Hadronic W pair production

Colour reconnections were first studied in the context of W pair production in e^+e^- collisions [23]. In cases where both W bosons decay hadronically, the production of jets in the two W systems might be affected by colour reconnection effects. Following the original proposal from Ref. [90], colour reconnection in $e^+e^- \to WW \to 4j$ events was studied at LEP [30–32]. In these analyses the W bosons are reconstructed via kinematic cuts on all possible jet pairs in four-jet events. The particle flow between jets originating from different bosons was expected to be enhanced in Monte Carlo models including colour reconnection. However, only moderate sensitivity to the tested colour reconnection models could be found at that time.

We confirm these results with our implementations. Figure 3.11 shows the sensitivity of the particle flow between the identified jets to the reconnection strength in the PCR model, compared to DELPHI data from Ref. [32]. We observe a slight improvement in the description of the data. A number of apparent outliers in the experimental data, however, indicate possibly too optimistic systematic errors in the experimental analysis. For that reason, no clear constraints on the model can be deduced from the data.

In e^+e^- annihilation at $\sqrt{s} = 189\,\text{GeV}$, W bosons are produced on their mass shell and are significantly boosted. The finite W width can thus cause the two W bosons to travel back to back over long distances before decaying. In the limit of a small W width, large colour reconnection effects between the two W systems should thus be suppressed in the model. The observed moderate sensitivity of the particle flow to colour reconnections implies, however, that colour reconnection effects are small in WW events. Also the largely vanishing colour length drop in WW events (Fig. 3.4) supports this conclusion. Hence we retain the described generic reconnection models also for WW events and do not introduce any extra suppression.

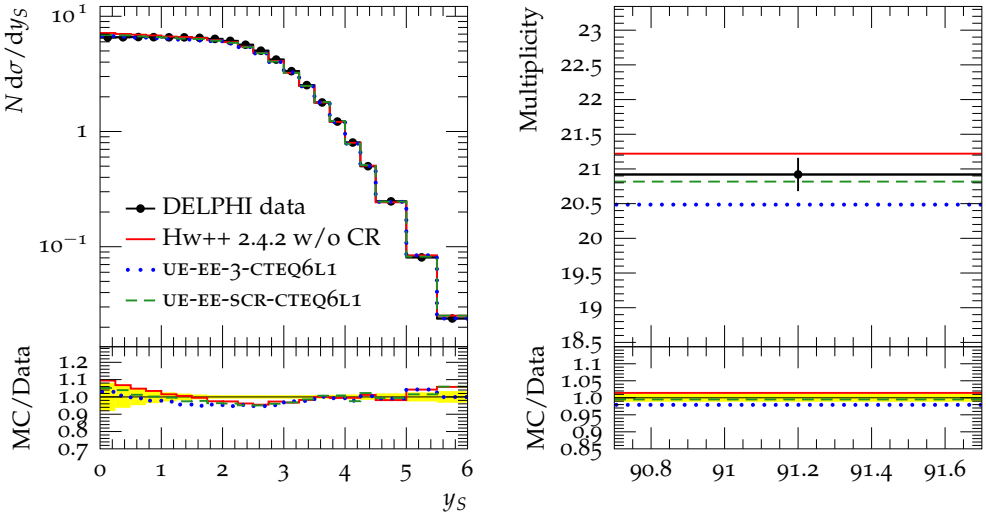

(a) (b)

Figure 3.10: Comparison of HERWIG++ with and without colour reconnection to LEP data measured at $\sqrt{s} = 91.2\,\mathrm{GeV}$ [86]. (a) Exemplary event shape observable: rapidity distribution w.r.t. the sphericity axis. (b) Average number of charged particles. The labels UE-EE-3-CTEQ6L1 and UE-EE-SCR-CTEQ6L1 refer to underlying-event tunes (see Sec. 3.5 below), which use the PCR and SCR models, respectively.

RIVET [75] analysis ID: `DELPHI_1996_S3430090`

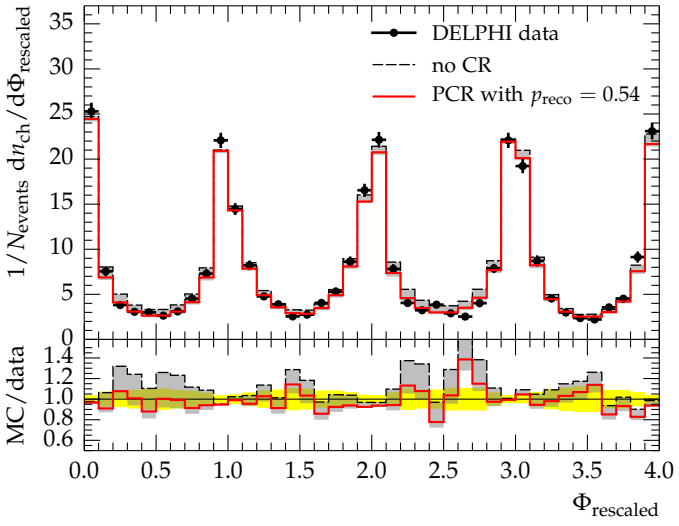

Figure 3.11: Charged-particle flow in hadronic WW events in e^+e^- collisions at $\sqrt{s} = 189\,\mathrm{GeV}$, measured at LEP [32]. The grey band indicates the range that is covered by varying the colour reconnection strength p_{reco} in the PCR model.

3.5 Tuning to data from hadron colliders

We found little sensitivity to colour reconnection in the description of e^+e^- data. This result allows a factorized tuning procedure: The final-state parton shower and hadronization parameters are tuned to e^+e^- data from LEP. Here, we retain the well-tested default tune from Ref. [4]. In subsequent tunes of colour reconnection and multiple-parton interaction parameters we use only hadron collider data.

3.5.1 General tuning procedure

The tuning of the bare MPI model (without colour reconnections) to underlying-event data from the Tevatron [64] included two tune parameters, μ^2 and $p_T^{\min}$ [8, 10]. The tuning was performed by subdividing the parameter space into a grid. The best parameter point was found by calculating the total χ^2 for each parameter point on this grid.

In combination with new parameters from the colour reconnection models, a larger number N of tune parameters has to be determined. In the case of the PCR model, we have $N = 4$ parameters (p_{disrupt}, p_{reco}, $p_T^{\min}$ and μ^2). For the SCR model there are even 7 parameters (p_{disrupt}, $p_T^{\min}$, μ^2, f_{isotherm}, t_0, f_{anneal} and N_{steps}). Therefore a simple parameter scan as described above is ineffective: for instance, a comprehensive scan of 7 parameters with 10 divisions in each parameter would require 10^7 event samples to be generated.

Instead, we use a more efficient parametrization-based method. This tuning procedure starts with the selection of a range $[p_i^{\min}, p_i^{\max}]$ for each of the N tune parameters p_i. Event samples are generated for random points of this N-dimensional hypercube in the parameter space. To achieve a well converging behaviour in the determination of the final tune, we adapt the number of sampled parameter points to the number of input parameters. The observables that construct the input for the tuning process are obtained from the generated event samples, where we use the Rivet analysis framework [91].

We achieve the main part of the tuning procedure using the Professor framework [75]. Professor parametrizes the generator response to the probed parameter points. In that way it finds the set of parameters that fits the selected observables best. The user is able to weight the observables, hence specifying their impact on the tuning process.

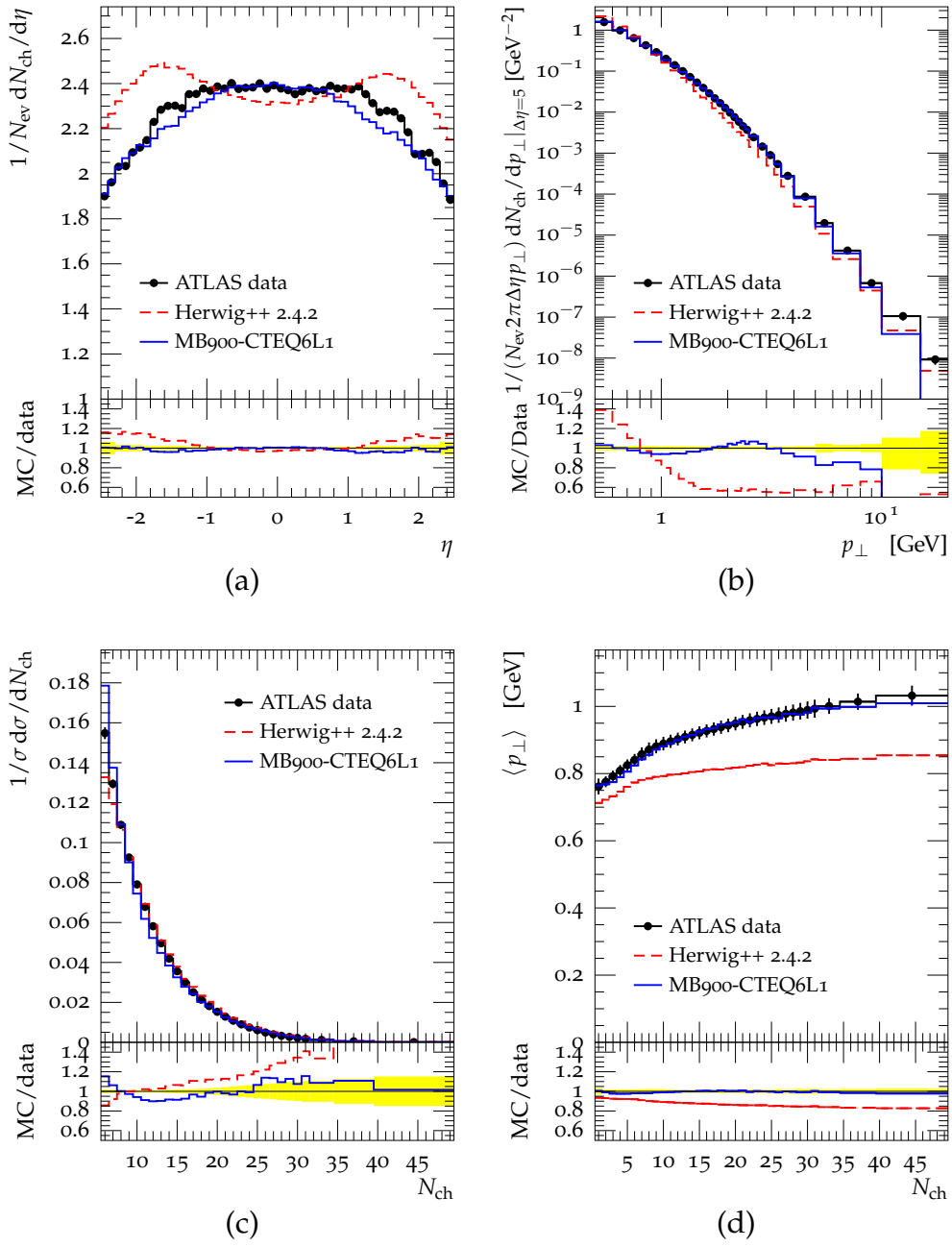

Figure 3.12: Comparison of HERWIG++ 2.5 with the MB900-CTEQ6L1 tune and HERWIG++ 2.4.2 (without colour reconnection, $\mu^2 = 1.0\,\text{GeV}^2$, $p_T^{\min} = 3.0\,\text{GeV}$) to diffraction-reduced minimum-bias data from ATLAS [13] at $\sqrt{s} = 900\,\text{GeV}$. (a) Charged-particle pseudorapidity distribution for $N_{ch} \geq 6$. (b) Transverse momentum distribution for $N_{ch} \geq 6$. (c) Charged-particle multiplicity distribution. (d) Average transverse momentum of charged particles as a function of N_{ch}.

RIVET [75] analysis ID: ATLAS_2010_S8918562

3.5.2 Tuning to diffraction-reduced minimum-bias data

We first tune the PCR model to minimum-bias data by ATLAS at $\sqrt{s} = 900\,\text{GeV}$. As the soft inclusive model in Herwig++ does not include diffractive final states, we use the diffraction-reduced ATLAS minimum-bias measurement from Ref. [13]. This data set contains events with at least six charged particles with $p_\text{T} > 500\,\text{MeV}$ and $|\eta| < 2.5$. We use four observables for the tuning with equal weights,

1. the pseudorapidity distribution of the charged particles,
2. the charged-particle multiplicity distribution,
3. the charged-particle transverse momentum distribution and
4. the average transverse momentum measured as a function of the number of charged particles.

We refer to the resulting tune as mb900-cteq6l1. As the name indicates, this tune uses the CTEQ6L1 PDF set [92]. The multiple-parton interaction model depends on the PDFs, e.g. in the calculation of the hard inclusive cross section (2.1). Hence, we prepare tunes of the MPI model in combination with several PDF sets. In the tune to minimum-bias data at 900 GeV we find better results if we use CTEQ6L1 instead of the default PDFs in Herwig++, MRST LO** [93].

The description of all minimum-bias observables improves in comparison to the Tevatron tune (Fig. 3.12). We conclude therefore that colour reconnections are a necessary component of the multiple-parton interaction model in Herwig++ in the description of nondiffractive soft events.

3.5.3 Tuning to underlying-event data

Next we study whether the PCR model can improve the description of the underlying event. For that purpose we tune the model parameters to underlying-event data from ATLAS at $\sqrt{s} = 7\,\text{TeV}$ [12].

The observables in this analysis are defined as follows: In each event, the azimuthal distance ϕ with respect to the leading track, i.e. the track with the highest transverse momentum, defines three kinematic regions,

- the "toward" region, where $|\phi| < \pi/3$,
- the "away" region, where $|\phi| > 2\pi/3$, and

- the remaining "transverse" region, where $\pi/3 < |\phi| < 2\pi/3$.

The toward and away regions typically contain jets than can be accounted to the hard parton interaction. In contrast, the region transverse to the leading object contains little activity from the hard subprocess. Hence, this region is most sensitive to the underlying event. The observables for the tune are

1. the average number and
2. the average scalar p_T sum

of charged particles per unit of $\eta\phi$, as a function of the transverse momentum of the leading track, p_T^{lead}.

We refer to the resulting tune as UE7-2. In comparison to the HERWIG++ 2.4.2 model without colour reconnections and with a tune to Tevatron data, the UE7-2 tune achieves an improved description of the average charged-particle multiplicity in all regions (Fig. 3.13). In general, we find good agreement with experimental data in all considered observables for p_T^{lead} greater than approximately 3 GeV. Below this value, the results for the average multiplicity and transverse momentum are too low. However, since the soft inclusive model in HERWIG++ includes no diffractive final states, we cannot expect a proper description of arbitrarily soft events.

3.5.4 Energy dependence of underlying-event tunes

The underlying-event tune UE7-2 applies for $\sqrt{s} = 7$ TeV, but is not guaranteed to describe the underlying event at other centre-of-mass energies. It is, however, possible to tune the underlying event at each energy separately. To enable predictions for other centre-of-mass energies, we parametrize the energy dependence of the model parameters.

For that purpose, we examine a set of underlying-event observables at different centre-of-mass energies. All data sets should be obtained in similar phase-space regions and measured under not too different trigger conditions. These requirements are met by the two observables introduced in Sec. 3.5.3, the average charged-particle multiplicity and the average scalar p_T sum, both as a function of the transverse momentum of the leading object.

We use measurements of these two observables by ATLAS for $\sqrt{s} =$ 900 GeV and 7000 GeV from Ref. [12] and by CDF for $\sqrt{s} = 1800$ GeV from Ref. [64]. The ATLAS analysis uses the hardest track as the leading

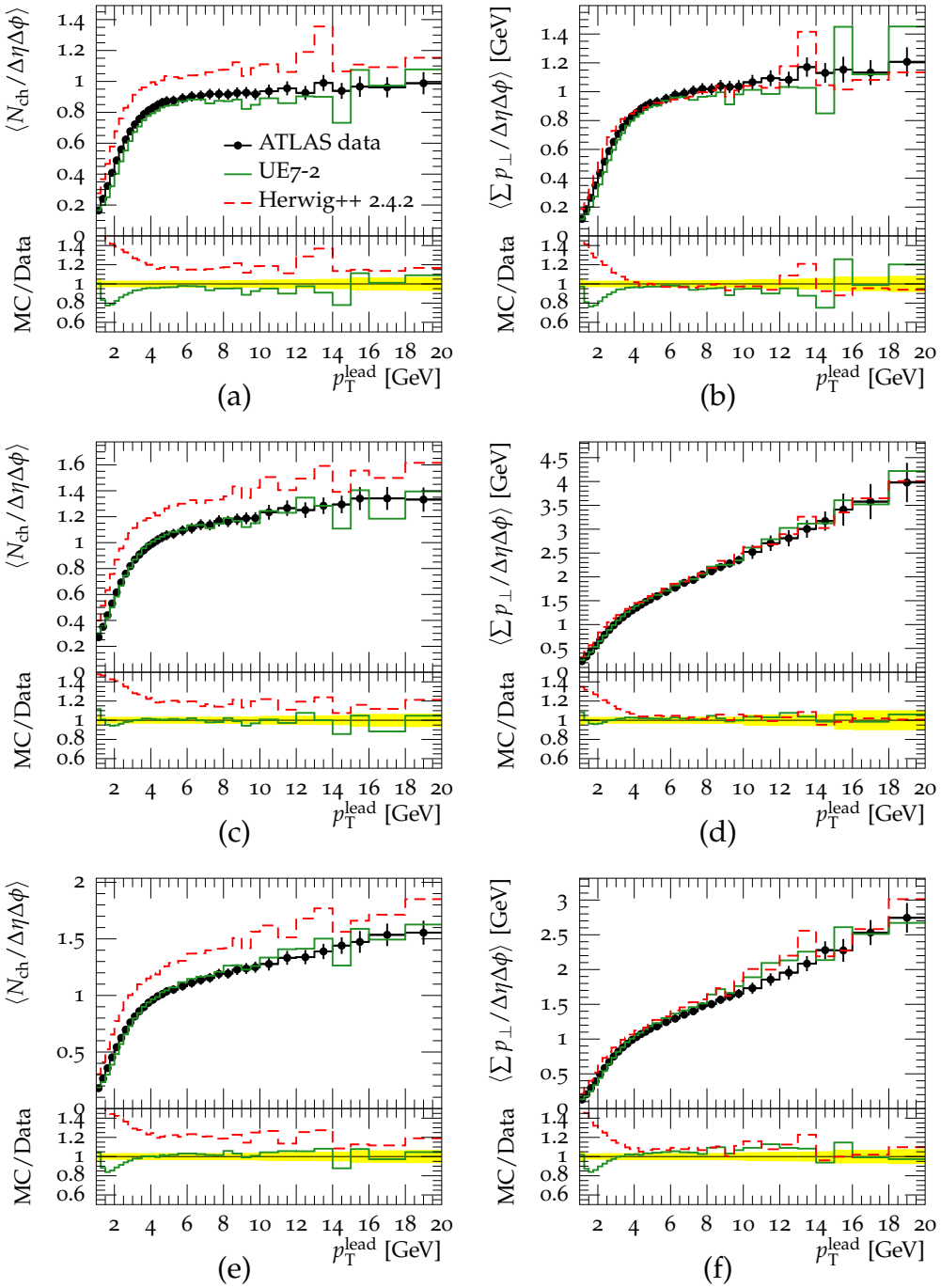

Figure 3.13: Comparison of the UE7-2 tune and Herwig++ 2.4.2 (no colour reconnection, default Tevatron tune) to underlying-event data from ATLAS [12] at 7 TeV. (a), (c) and (e): Charged-particle multiplicity per unit of $\eta\phi$ as a function of p_T^{lead} in the transverse, toward and away regions. (b), (d) and (f): Scalar p_T sum per unit of $\eta\phi$ as a function of p_T^{lead} in the transverse, toward and away regions. Rivet [75] analysis ID: ATLAS_2010_S8894728

object. In contrast, in the CDF analysis the hardest *jet* is taken as the leading object. We denote the transverse momentum of the leading object in both cases as $p_{\mathrm{T}}^{\mathrm{lead}}$.

First we focus on the PCR model, in which we have four free model parameters, p_{disrupt}, p_{reco}, $p_{\mathrm{T}}^{\mathrm{min}}$ and μ^2. In the first step, we perform separate tunings for each centre-of-mass energy. The tune results reveal that the 7 TeV data constrains the parameters more than the data at 900 GeV (Fig. 3.14). In addition, we find that the data prefers different values of $p_{\mathrm{T}}^{\mathrm{min}}$ for the two centre-of-mass energies. Hence the same set of parameters cannot describe the data at all energies. The preferred tune values of the other parameters overlap for both analyses.

This result hints at the possibility to project the complete centre-of-mass energy dependence of underlying-event tunes onto an energy-dependent $p_{\mathrm{T}}^{\mathrm{min}}$ parameter. We thus create tunes in which $p_{\mathrm{T}}^{\mathrm{min}}$ varies with the centre-of-mass energy, whereas all other parameters are fixed (Tables 3.1 and 3.2). We refer to the resulting "energy extrapolation" tunes for the MRST LO** and the CTEQ6L1 PDFs as UE-EE-3 and UE-EE-3-CTEQ6L1, respectively.

We repeat this tuning procedure for the SCR model. One of the model parameters, N_{steps}, is an integer number. We carry out fifty separate tunes for different fixed values of N_{steps}, starting from 1 to 50. We identify regions in the parameter space in which predictions using the parametrized generator response differ significantly from actual generator results. Since increasing the order of the interpolation polynomials to four does not solve this problem, we exclude the problematic parameter space regions from the tuning procedure. We refer to the resulting underlying-event tune for the SCR model (Tables 3.1 and 3.2) as UE-EE-SCR-CTEQ6L1.

The energy extrapolation tunes agree well with underlying-event data at $\sqrt{s} = 900\,\mathrm{GeV}$, 1.8 TeV and 7 TeV (Figs. 3.16–3.18). We therefore conclude that we can describe the centre-of-mass energy dependence of the underlying-event model in fact with only an energy dependent $p_{\mathrm{T}}^{\mathrm{min}}$ parameter.

In the last step, we parametrize the dependence of $p_{\mathrm{T}}^{\mathrm{min}}$ on the centre-of-mass energy. This parametrization enables underlying-event tunes for energies other than the three energies explicitly considered in the tunes. We choose a power law ansatz for the s-dependence of $p_{\mathrm{T}}^{\mathrm{min}}$,

$$p_{\mathrm{T}}^{\mathrm{min}}(s) = p_{\mathrm{T},0}^{\mathrm{min}} \left(\frac{\sqrt{s}}{E_0} \right)^{b} , \tag{3.6}$$

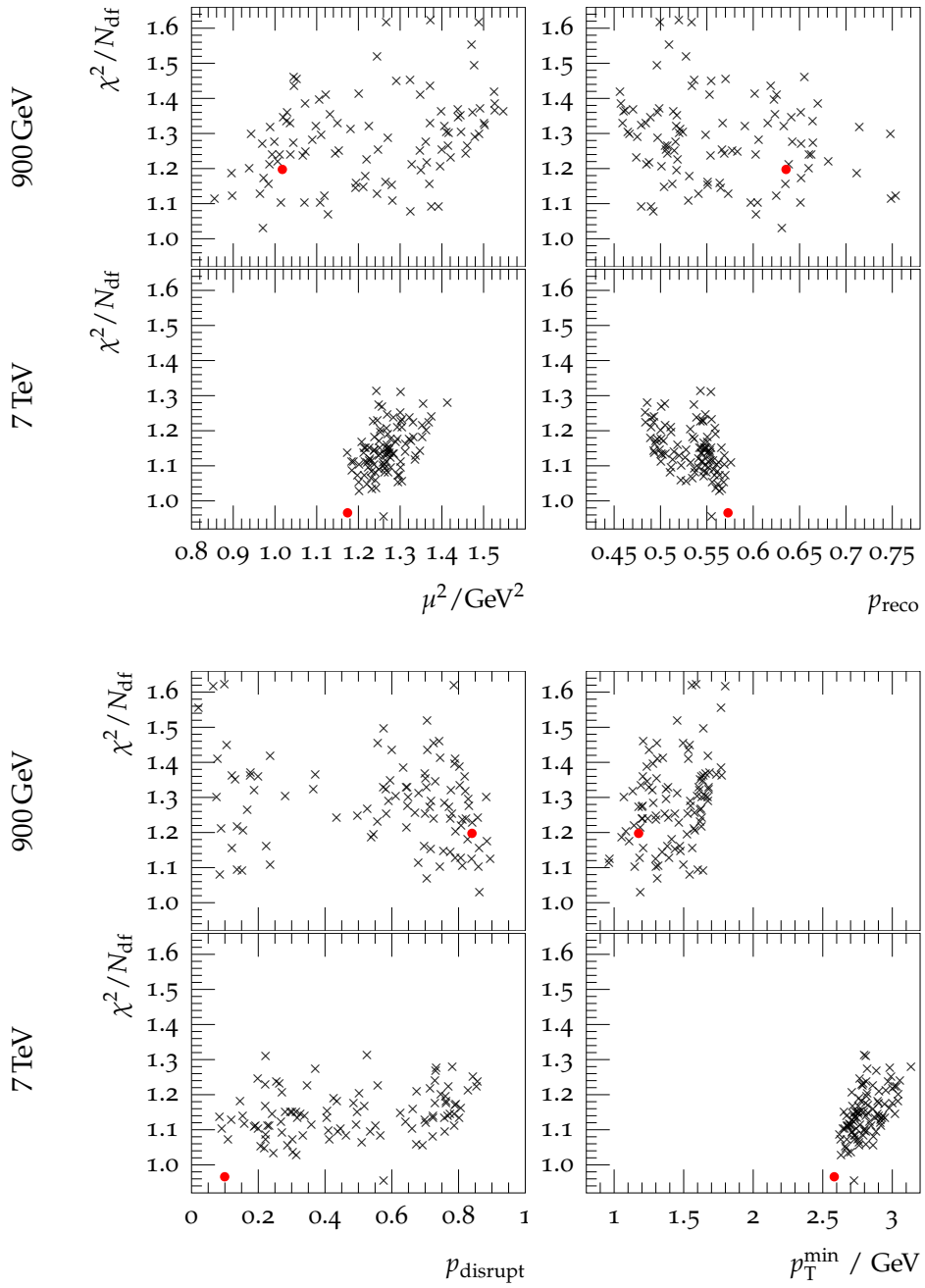

Figure 3.14: Distribution of the UE-EE-3-CTEQ6L1 tuning results for the tune parameters in the PCR model. The points are the minimization results based on different subsets of generator runs (black crosses) or on all generator runs (red circles). The generator response was interpolated with cubic polynomials. For each parameter, the figures for 900 GeV and 7 TeV share a common horizontal axis.

Table 3.1: Tune values and parametrization of p_T^{min}.

p_T^{min} / GeV				parametrization	
	$\sqrt{s}$ / GeV			$p_{T,0}^{min}$ / GeV	b
	900	1800	7000		
UE-EE-3	1.55	2.26	2.75	3.11	0.21
UE-EE-3-CTEQ6L1	1.86	2.55	3.06	2.81	0.24
UE-EE-SCR-CTEQ6L1	1.58	2.14	2.60	2.64	0.21

Table 3.2: Tune values of the energy-independent parameters.

	PCR model		SCR model
	UE-EE-3	UE-EE-3-CTEQ6L1	UE-EE-SCR-CTEQ6L1
μ^2/GeV^2	1.11	1.35	1.5
p_{disrupt}	0.80	0.75	0.8
p_{reco}	0.54	0.61	
t_0			0.01
f_{anneal}			0.21
N_{steps}			10
f_{isotherm}			0.66

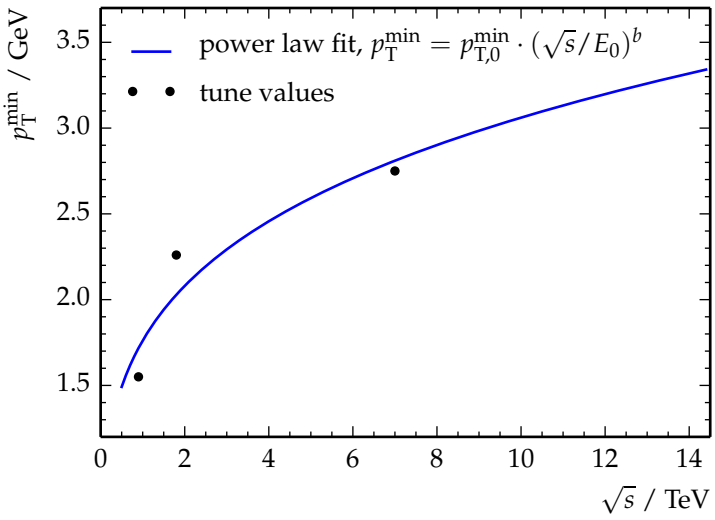

Figure 3.15: Parametrization of p_T^{min} in the UE-EE-3-CTEQ6L1 tune.

with $E_0 = 7\,\text{TeV}$. This is the default parametrization of p_T^{min} in HERWIG++ as of release 2.6 [79]. The parametric form of $p_T^{min}(s)$ is determined in a fit to the tune values at the three tune energies. We summarize the fit results also in Table 3.1. The dependence of p_T^{min} on the centre-of-mass energy in the UE-EE-3-CTEQ6L1 is shown in Fig. 3.15.

3.5.5 Minimum-bias data at 7 TeV

ATLAS provides minimum-bias measurements at 7 TeV in Ref. [13]. To reduce the fraction of diffractive events, they provide data from measurements in a restricted phase space region, where at least six charged particles in the kinematic range $|\eta| < 2.5$ and $p_T > 500\,\text{MeV}$ are required. ATLAS shows also results from a more inclusive measurement, which requires only two charged particles with $|\eta| < 2.5$ and with $p_T > 100\,\text{MeV}$.

In the preparation of the energy extrapolation tunes we used only underlying-event data. Still we find a reasonable description of the diffraction-reduced minimum-bias data using the UE-EE-3-CTEQ6L1 and UE-EE-3-CTEQ6L1 tunes (Fig. 3.19). The tunes, however, fail to reproduce the aforementioned more inclusive data set (Fig. 3.20). We expect better results with a model that includes diffractive events. The discrepancy in the average transverse momentum in high-multiplicity events may also indicate missing physics in the model.

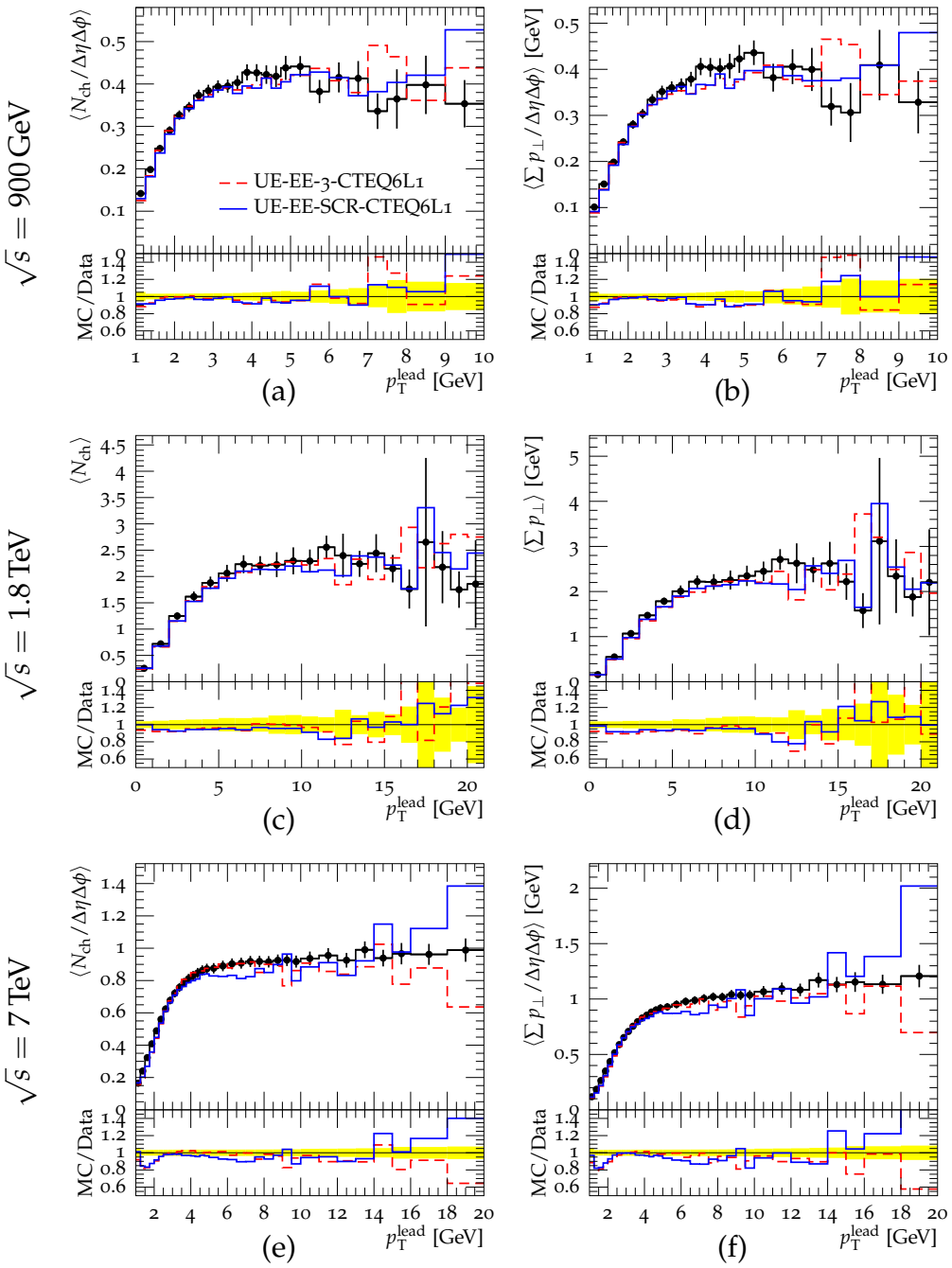

Figure 3.16: Results of energy extrapolation tunes at different c.m. energies in the **transverse region**. The data for 900 GeV and 7 TeV is from ATLAS [12], the data for 1.8 TeV is from CDF [64]. (a), (c) and (e): Average charged-particle multiplicity at 900 GeV, 1.8 TeV and 7 TeV. (b), (d) and (f): Average charged-particle scalar p_T sum at the aforementioned energies. The ATLAS observables are normalized to one unit of $\eta\phi$. The η-ϕ area in the CDF data is $\Delta\eta\Delta\phi = 4\pi/3$.

RIVET [75] analysis IDs: `ATLAS_2010_S8894728`, `CDF_2001_S4751469`

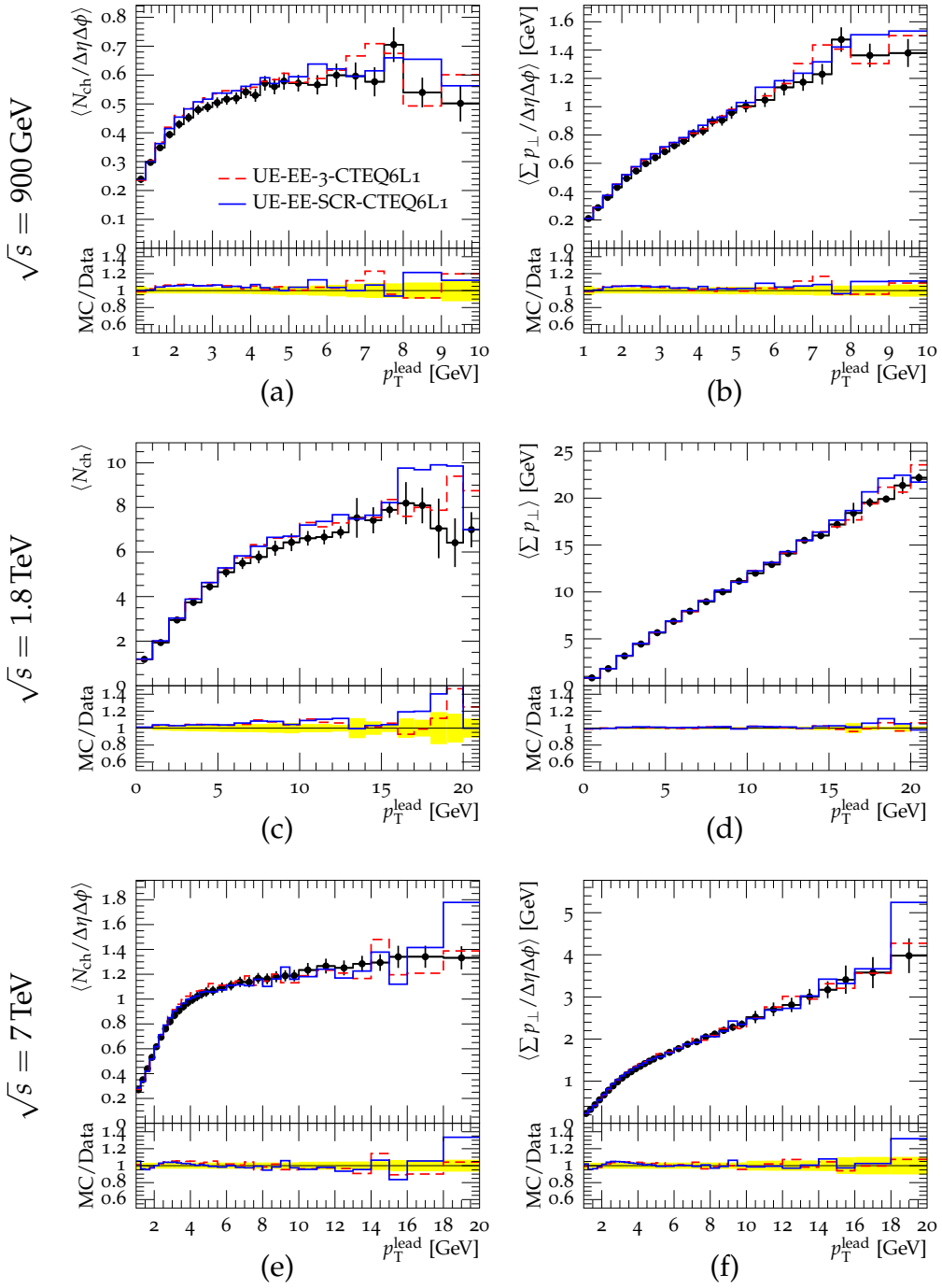

Figure 3.17: Observables from Fig. 3.16 in the **toward region**.

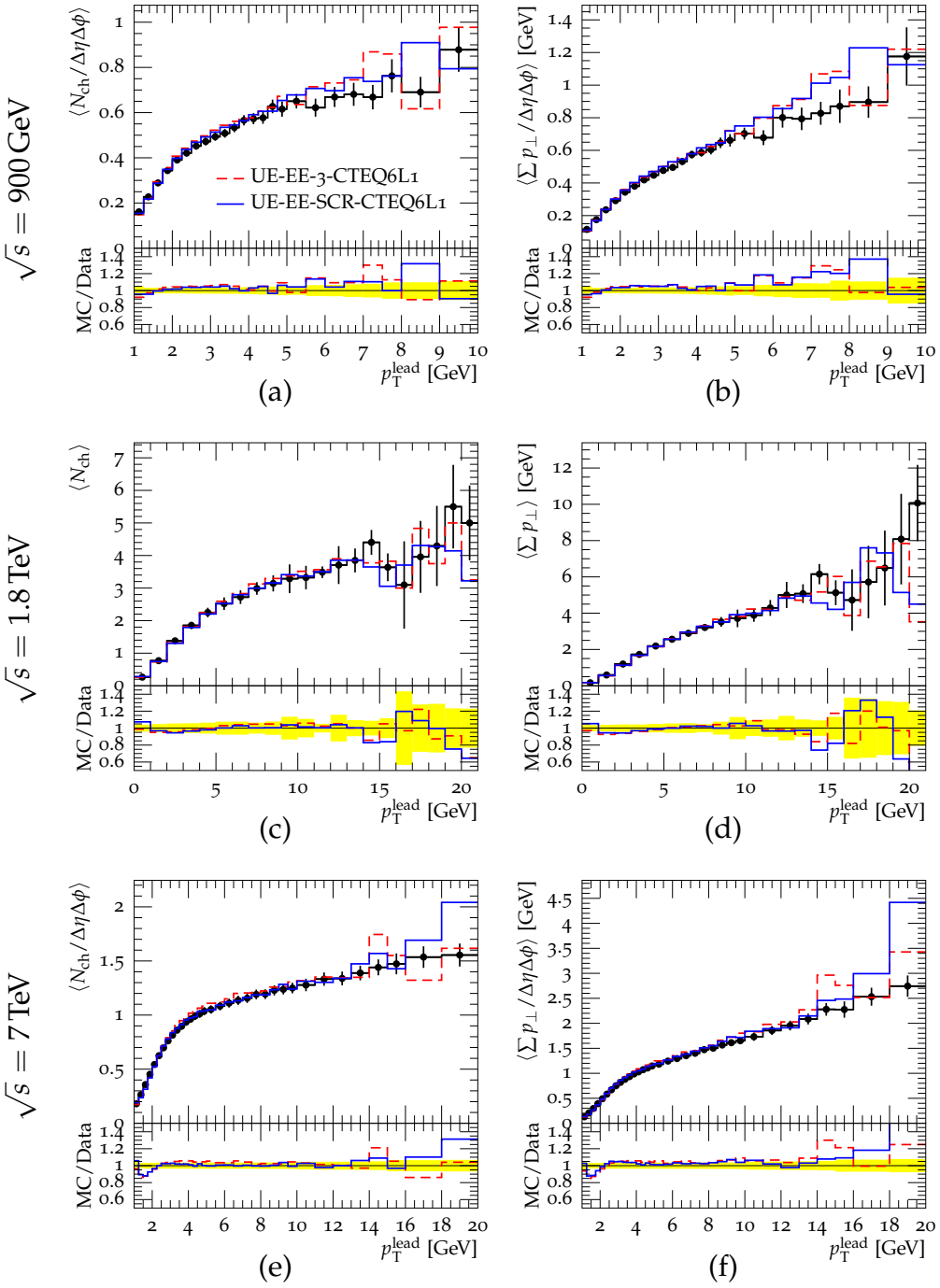

Figure 3.18: Observables from Fig. 3.16 in the **away region**.

3.6 Conclusions

We have introduced two models for nonperturbative colour reconnections in Herwig++. The models are of slightly different computational complexity but give very similar results. The tuning results have shown that the SCR is preferred to have parameters that force a quick "cooling" of the system and therefore results in a very similar model evolution as in the simpler PCR model. We therefore consider the PCR model as a special case of the SCR model for quick cooling and keep the SCR model as the more flexible one for future versions of Herwig++. As a consequence, we understand that the data demands a final state that does not obey a perfectly minimized colour length. We interpret this as a model limitation. Colour lines approximate the colour structure only up to leading order in the large-N_C limit. Furthermore, the mechanism addresses the nonperturbative regime. In this regime, the picture of the colour triplet charges is already a model by itself and possibly completely washed out.

We have studied the mechanism of colour reconnection at the level where clusters are formed from partons. We found that in fact the nonperturbative parts of the simulation demand the colour reconnection mechanism to repair the lack of information on the colour flow. The intuitive picture we have based our model on could be verified. Colour preconfinement is meaningful in the context of the cluster hadronization model. The implications of preconfinement, however, have to be rectified when a model of multiple parton interactions is applied without further information on the colour structure between the multiple scatters.

Furthermore, we have shown that the MPI model with colour reconnection can properly describe nondiffractive minimum-bias data from ATLAS. Moreover, we could show that the model is in good agreement with underlying-event data from CDF at the Tevatron and ATLAS at the LHC. Finally, we have unified the underlying-event tunes at Tevatron and LHC energies into a simple parametrization of a single model parameter in the centre-of-mass energy. This parametrization allows to estimate the underlying-event activity at future LHC energies.

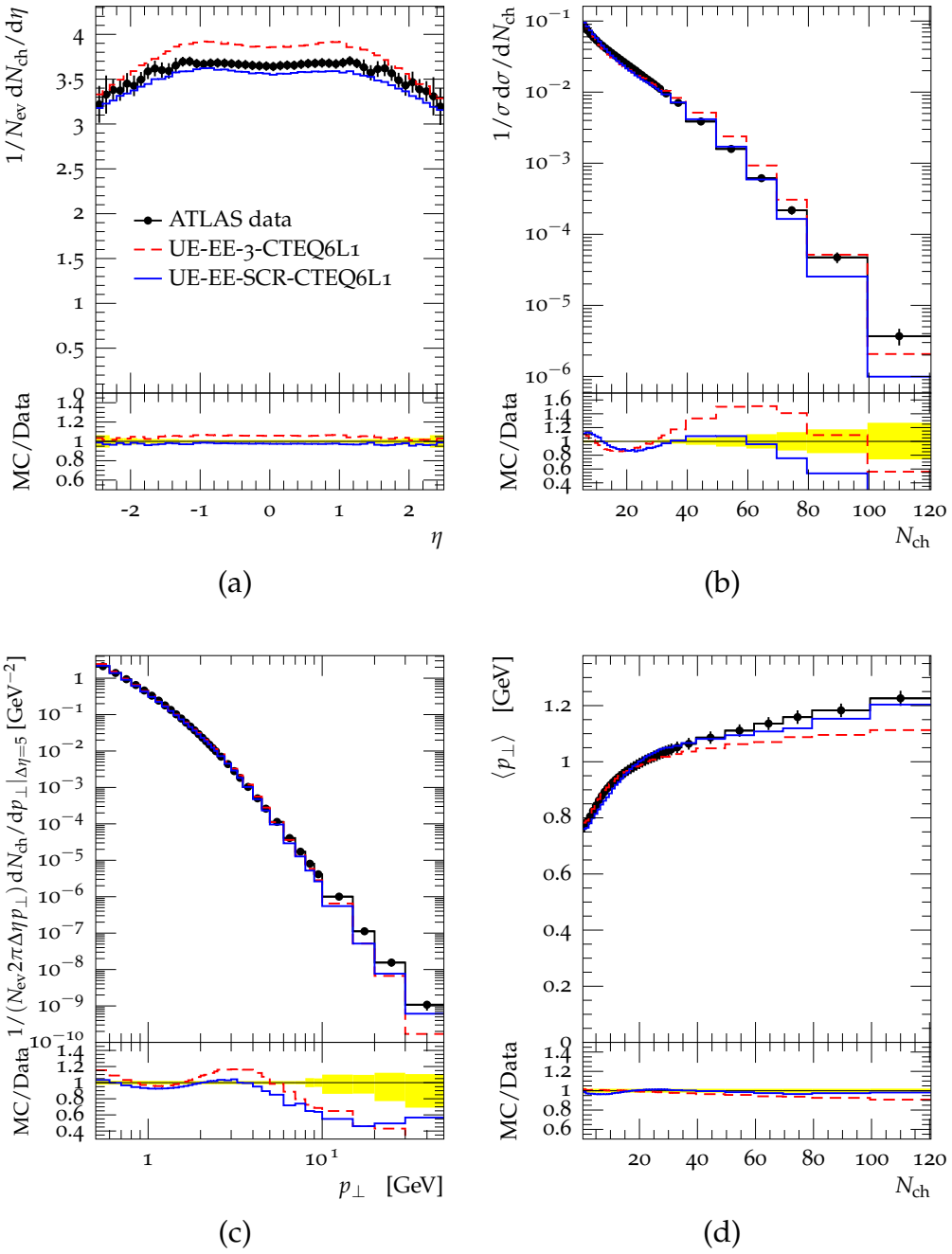

Figure 3.19: Comparison of energy extrapolation tunes to minimum-bias data by ATLAS from Ref. [13], where $\sqrt{s} = 7\,\text{TeV}$ and track $p_\text{T} > 500\,\text{MeV}$. (a) Charged-particle pseudorapidity for $N_\text{ch} \geq 6$. (b) Charged-particle multiplicity. (c) Charged-particle transverse momentum for $N_\text{ch} \geq 6$. (d) Average charged-particle transverse momentum.

RIVET [75] analysis ID: ATLAS_2010_S8918562

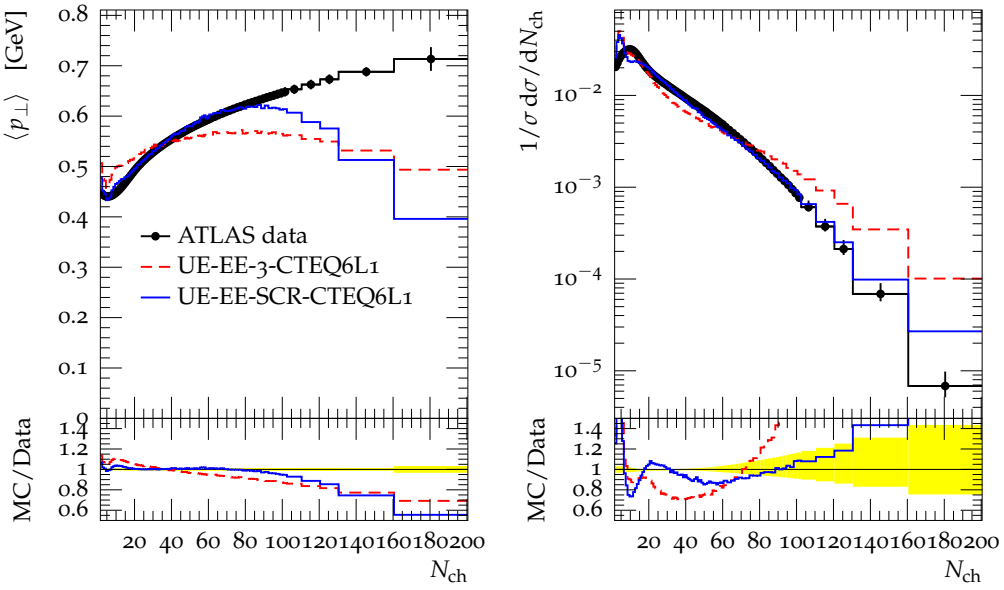

(a) (b)

Figure 3.20: Comparison of energy extrapolation tunes to minimum-bias data by ATLAS from Ref. [13], where $\sqrt{s} = 7\,\text{TeV}$ and track $p_\text{T} > 100\,\text{MeV}$. (a) Average charged-particle transverse momentum. (b) Charged-particle multiplicity.

Rivet [75] analysis ID: ATLAS_2010_S8918562

Chapter 4

Diffractive cross sections in the eikonal model

The second part of this thesis covers the implementation and analysis of a model for diffractive cross sections in the event generator Herwig++. We start with a detailed description of the formalism that is used for the calculation of hadronic cross sections. We are able to connect many parts of the model to the underlying formalism of the multiple-parton interactions model in Herwig++. Finally, we report on the determination of the model parameters in a fit to collider and cosmic-ray data.

4.1 Two-channel eikonal model

The eikonal model for multiple-parton interactions from Sec. 1.7 is based on the elastic-rescattering approximation of the elastic multi-pomeron amplitude (1.18). Physical quantities like the elastic (1.28), inelastic (1.25) and total cross sections (1.27) are expressed in the eikonal model in terms of the eikonal function

$$\chi(s,b) = -2\mathrm{i}\mathcal{A}^{(1)}(s,b)\,, \qquad \text{(1.22 revisited)}$$

where $\mathcal{A}^{(1)}(s,b)$ denotes the elastic single-pomeron amplitude. We discussed in Chapter 2 how the standard eikonal model is used in Herwig++ as a model for multiple hard and soft interactions, where the eikonal function is separated into a soft and a hard part,

$$\chi(s,b) = \chi_{\mathrm{S}}(s,b) + \chi_{\mathrm{H}}(s,b)\,. \qquad \text{(2.7 revisited)}$$

In order to include low-mass diffraction in the existing eikonal framework for multiple soft and hard parton interactions in Herwig++, we

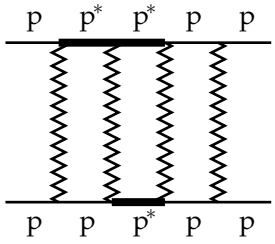

Figure 4.1: Sample diagram with resonances p^* in the intermediate state.

introduce a two-channel eikonal model [36, 37, 56]. This model distinguishes two states of the scattering protons:[1] A ground state $|p\rangle$ and a diffractive resonance $|p^*\rangle$, which approximates diffractive inelastic states [56]. The process $pp \to pp^*$ corresponds, for instance, to low-mass single diffraction dissociation of one of the protons. Diffractive resonances also occur in intermediate states in diagrams with several pomerons (Fig. 4.1).

4.1.1 Matrix formalism

All contributions for the calculation of amplitudes and cross sections in the two-channel eikonal model can conveniently be taken into account using the matrix formalism from Ref. [56]. Therefore, we introduce a matrix of eikonal functions with respect to all possible combinations of external states $|p\rangle$ and $|p^*\rangle$ of two protons. This matrix is defined as

$$\langle ij|\hat{\chi}(s,b)|kl\rangle \equiv \chi_{ij\to kl}(s,b) \equiv -2i\mathcal{A}^{(1)}_{ij\to kl}(s,b)\,, \tag{4.1}$$

where $i,j,k,l \in \{p,p^*\}$ and $\mathcal{A}^{(1)}_{ij\to kl}(s,b)$ denotes the $ij \to kl$ amplitude with one pomeron in the t-channel. We refer to $\hat{\chi}(s,b)$ as the eikonal matrix. For clarity, matrices are indicated with the symbol $\hat{}$ in this discussion.

For the elastic eikonal function, $\chi_{pp\to pp}(s,b)$, we retain the Herwig++ parametrization (2.7) and denote it shortly as $\chi(s,b)$. We parametrize the eikonal functions $\chi_{ij\to kl}(s,b)$ for general i, j, k and l in terms of $\chi(s,b)$: following Ref. [36], we define the real-valued enhancement factor λ as the coupling of the pomeron $\mathbb{P}$ to a proton p and a resonance p^* in units of the pp$\mathbb{P}$ coupling,

$$g_{pp^*\mathbb{P}} = g_{p^*p\mathbb{P}} = \lambda\, g_{pp\mathbb{P}}\,. \tag{4.2}$$

[1] For simplicity, we restrict the discussion to pp scattering. The results, however, apply to $p\bar{p}$ as well.

The enhancement factor λ is a free parameter of the two-channel model. For simplicity, we assume $g_{\mathrm{p^*p^*\mathbb{P}}} = g_{\mathrm{pp}\mathbb{P}}$, similar to Refs. [36, 94]. A model without this simplification is described in Ref. [95]. The parametrization (4.2) results, for example, in

$$\chi_{\mathrm{pp}\to\mathrm{pp^*}}(s,b) = \lambda\,\chi(s,b)\,. \tag{4.3}$$

The complete eikonal matrix (4.1) reads

$$\hat{\chi}(s,b) = \begin{pmatrix} 1 & \lambda & \lambda & \lambda^2 \\ \lambda & 1 & \lambda^2 & \lambda \\ \lambda & \lambda^2 & 1 & \lambda \\ \lambda^2 & \lambda & \lambda & 1 \end{pmatrix} \chi(s,b)\,, \tag{4.4}$$

where the rows and columns of the matrix correspond to the basis

$$|\mathrm{pp}\rangle = \begin{pmatrix}1\\0\\0\\0\end{pmatrix},\ |\mathrm{p^*p}\rangle = \begin{pmatrix}0\\1\\0\\0\end{pmatrix},\ |\mathrm{pp^*}\rangle = \begin{pmatrix}0\\0\\1\\0\end{pmatrix} \text{ and } |\mathrm{p^*p^*}\rangle = \begin{pmatrix}0\\0\\0\\1\end{pmatrix}. \tag{4.5}$$

The n-pomeron amplitude (1.21) is generalized in the two-channel eikonal model to

$$\hat{\mathcal{A}}^{(n)}(s,b) = \frac{1}{2\mathrm{i}}\frac{\big(-\hat{\chi}(s,b)\big)^n}{n!}\,. \tag{4.6}$$

This expression adds up all possible intermediate states. For instance, the two-pomeron contribution to the elastic amplitude is

$$\begin{aligned} \big\langle \mathrm{pp}\big|\hat{\mathcal{A}}^{(2)}(s,b)\big|\mathrm{pp}\big\rangle &= \Big\langle \mathrm{pp}\Big|\frac{1}{2\mathrm{i}}\frac{\big(-\hat{\chi}(s,b)\big)^2}{2!}\Big|\mathrm{pp}\Big\rangle \\ &= \Big(1+2\lambda^2+\lambda^4\Big)\,\frac{1}{2\mathrm{i}}\frac{\big(-\chi(s,b)\big)^2}{2!} \\ &= \Big(1+2\lambda^2+\lambda^4\Big)\,\mathcal{A}^{(2)}(s,b)\,, \end{aligned} \tag{4.7}$$

taking into account (1.21) and (4.4). The last line coincides in fact with the sum of all possible $\mathrm{pp}\to\mathrm{pp}$ diagrams with two pomerons (Fig. 4.2).

Analogous to the elastic amplitude in the "single-channel" eikonal model, (1.26), we obtain the amplitudes for elastic and low-mass diffractive scattering by adding up all n-pomeron amplitude matrices (4.6), which results in

$$\hat{\mathcal{A}}(s,b) = \frac{\mathrm{i}}{2}\Big(1-\mathrm{e}^{-\hat{\chi}(s,b)}\Big)\,. \tag{4.8}$$

The elastic amplitude is the $\mathrm{pp}\to\mathrm{pp}$ component,

$$\mathcal{A}_{\mathrm{el}}(s,b) = \Big\langle \mathrm{pp}\Big|\,\frac{\mathrm{i}}{2}\Big(1-\mathrm{e}^{-\hat{\chi}(s,b)}\Big)\,\Big|\mathrm{pp}\Big\rangle\,. \tag{4.9}$$

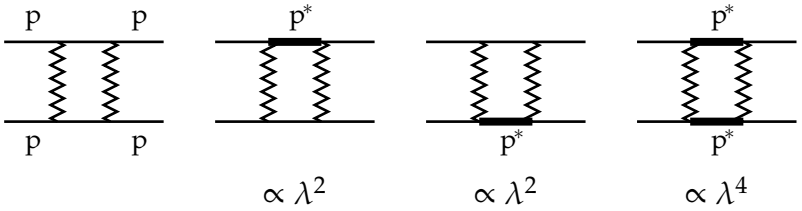

Figure 4.2: All two-pomeron diagrams contributing to the elastic scattering amplitude in the two-channel eikonal model.

4.1.2 Cross sections in the two-channel eikonal model

With the elastic amplitude (4.9), the total cross section (1.6) reads

$$\sigma_{\text{tot}}(s) = 2\int \mathrm{d}^2b \left\langle \mathrm{pp}\middle|1 - \mathrm{e}^{-\hat{\chi}(s,b)}\middle|\mathrm{pp}\right\rangle \tag{4.10}$$

The cross section for nondiffractive exclusive production of j soft and k hard interactions (2.8) is in the two-channel eikonal model

$$\sigma_{jk}(s) = \int \mathrm{d}^2b \left\langle \mathrm{pp}\middle|\frac{(2\hat{\chi}_{\mathrm{S}})^j}{j!}\frac{(2\hat{\chi}_{\mathrm{H}})^k}{k!}\exp[-2\left(\hat{\chi}_{\mathrm{S}}+\hat{\chi}_{\mathrm{H}}\right)]\middle|\mathrm{pp}\right\rangle, \tag{4.11}$$

where $\hat{\chi}_{\mathrm{S}}$ and $\hat{\chi}_{\mathrm{H}}$ are the eikonal matrices (4.4) with the soft and hard amplitudes separated ($\hat{\chi} = \hat{\chi}_{\mathrm{S}} + \hat{\chi}_{\mathrm{H}}$). The nondiffractive inelastic cross section (1.25), i.e. the sum of all nondiffractive exclusive cross sections σ_{jk} with $j + k \geq 1$, is

$$\sigma_{\text{inel}}^{\text{nd}}(s) = \int \mathrm{d}^2b \left\langle \mathrm{pp}\middle|1 - \mathrm{e}^{-2\hat{\chi}(b,s)}\middle|\mathrm{pp}\right\rangle. \tag{4.12}$$

Finally, the cross sections for elastic scattering and, analogously, for resonance production, i.e. low-mass diffraction, are obtained from (1.6),

$$\sigma_{\text{el}}(s) = \int \mathrm{d}^2b \left|\left\langle \mathrm{pp}\middle|1 - \mathrm{e}^{-\hat{\chi}(s,b)}\middle|\mathrm{pp}\right\rangle\right|^2, \tag{4.13}$$

$$\sigma_{\text{sd,a}}^{\text{lm}}(s) = \int \mathrm{d}^2b \left|\left\langle \mathrm{p^*p}\middle|1 - \mathrm{e}^{-\hat{\chi}(s,b)}\middle|\mathrm{pp}\right\rangle\right|^2, \tag{4.14}$$

$$\sigma_{\text{sd,b}}^{\text{lm}}(s) = \int \mathrm{d}^2b \left|\left\langle \mathrm{pp^*}\middle|1 - \mathrm{e}^{-\hat{\chi}(s,b)}\middle|\mathrm{pp}\right\rangle\right|^2, \tag{4.15}$$

$$\sigma_{\text{dd}}^{\text{lm}}(s) = \int \mathrm{d}^2b \left|\left\langle \mathrm{p^*p^*}\middle|1 - \mathrm{e}^{-\hat{\chi}(s,b)}\middle|\mathrm{pp}\right\rangle\right|^2. \tag{4.16}$$

4.1.3 Eikonal matrix diagonalization

The cross sections (4.10)–(4.16) can be evaluated by diagonalizing the eikonal matrix [36]. For the total cross sections one finds, for instance,

$$\sigma_{\text{tot}}(s) = \frac{1}{2}\int \mathrm{d}^2b \sum_{\alpha=1}^{4} \left(1 - \mathrm{e}^{-\chi^{(\alpha)}(s,b)}\right) , \tag{4.17}$$

where $\chi^{(\alpha)}(s,b)$ are the eigenvalues of the eikonal matrix (4.4),

$$\begin{aligned} \chi^{(1)}(s,b) &= (1-\lambda)^2\,\chi(s,b)\,, \\ \chi^{(2)}(s,b) &= (1+\lambda)^2\,\chi(s,b)\,, \\ \chi^{(3)}(s,b) &= \chi^{(4)}(s,b) = (1-\lambda^2)\,\chi(s,b)\,. \end{aligned} \tag{4.18}$$

We elaborate on the diagonalization of eikonal matrices in Appendix A. The results for the cross sections (4.11)–(4.16) are summarized in Appendix B.1.

4.2 Impact parameter amplitudes

For the construction of the soft and hard eikonal functions we retain the overlap function $A(b,\mu)$ from the MPI model, which is defined in (2.4). The hard eikonal function is hence

$$\chi_{\text{H}}(s,b) = \frac{1}{2} A(b,\mu_{\text{H}})\,\sigma_{\text{H}}^{\text{inc}}(s,p_{\text{T}}^{\min})\,, \tag{2.6 revisited}$$

with $\sigma_{\text{H}}^{\text{inc}}$ calculated within perturbative QCD according to (2.1). We keep μ_{H} as a free parameter, which specifies the width of the hard-pomeron amplitude in impact parameter space.

The soft eikonal function is constructed analogously,

$$\chi_{\text{S}}(s,b) = \frac{1}{2} A(b,\mu_{\text{S}})\,\sigma_{\text{S}}^{\text{inc}}(s)\,. \tag{4.19}$$

As discussed in Sec. 2.2, the MPI model determines μ_{S} and $\sigma_{\text{S}}^{\text{inc}}(s)$ in a fit of the total cross section (1.27) and the elastic slope (1.29) with $\chi = \chi_{\text{S}} + \chi_{\text{H}}$ to experimental data. Instead, we fix the s-dependence of the soft cross section according to the single-pomeron amplitude (1.16) in Regge theory,

$$\sigma_{\text{S}}^{\text{inc}}(s) = g_{\text{p}\mathbb{P}}^2 \left(\frac{s}{s_0}\right)^{\alpha(0)-1} , \tag{4.20}$$

where the proton-pomeron coupling $g_{\mathrm{p}\mathbb{P}}$ and the soft-pomeron intercept $\alpha(0)$ are model parameters. Additionally, μ_{S} in (4.19) is treated as a free parameter. For simplicity, we neglect reggeon contributions and parametrize the soft cross section only with a pomeron term. We assume this ansatz to be valid at high centre-of-mass energies, particularly at LHC energies.

4.3 Enhanced pomeron diagrams

As customary, we include the description of high-mass diffraction by means of enhanced pomeron diagrams [56]. The diagrams in Fig. 4.3 are considered as contributions to the elastic-scattering amplitude. Following Refs. [36, 38], we take contributions due to multiple enhanced diagrams into account by including eikonal functions for enhanced pomeron diagrams in the eikonal model.

The triple pomeron (TP) diagram accounts for diffractive dissociation of one of the incoming particles into a high-mass state [56]. The loop pomeron (LP) diagram corresponds to diffractive production of two high-mass states [56]. Furthermore, we include the double pomeron (DP) diagram [38]. This diagram is the dominant correction to the loop and triple pomeron diagrams [94, 96]. The double pomeron diagram accounts for the production of high-mass states via scattering of two pomerons.

The aforementioned enhanced diagrams contain only triple pomeron self couplings. A more general model with n pomerons coupling to m pomerons, where $n + m > 3$, is discussed in Ref. [97]. As there is little knowledge about quartic and higher-order pomeron couplings, further modelling would be required here. To keep the model as simple as possible, we do not include these contributions to the elastic scattering amplitude.

4.3.1 Eikonal functions of enhanced processes

Analogous to the hard and soft eikonal functions (2.7) in the MPI model, we construct the eikonal functions of the triple pomeron, loop pomeron and double pomeron amplitudes as

$$\chi_i(s,b) = \frac{1}{2} A(b,\mu_i)\,\sigma_i(s)\,, \quad \text{with } i = \mathrm{TP_a}, \mathrm{TP_b}, \mathrm{LP}, \mathrm{DP}\,. \tag{4.21}$$

In order to account for the asymmetric shape of the triple pomeron diagram, we distinguish two different eikonal functions in the formalism,

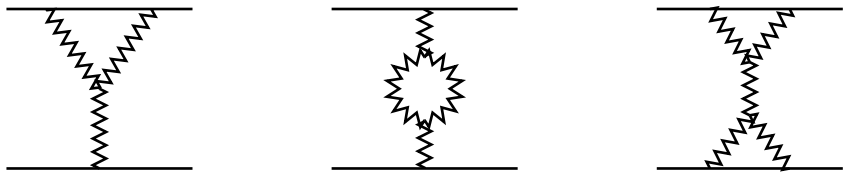

(a) (b) (c)

Figure 4.3: Enhanced pomeron diagrams. (a) Triple pomeron diagram. (b) Loop pomeron diagram. (c) Double pomeron diagram.

$\mathrm{TP_a}$ and $\mathrm{TP_b}$. The forward elastic amplitudes of the considered enhanced diagrams and, via the optical theorem, the cross sections σ_i can be calculated using reggeon field theory [55]. The result for the triple pomeron cross section is [94]

$$\begin{aligned}\sigma_{\mathrm{TP}}(s) = &-\frac{g_{\mathrm{p}\mathbb{P}}^3\, g_{3\mathbb{P}}}{2\alpha' \, 16\pi(\hbar c)^2}\left(\frac{s}{s_0}\right)^{\Delta_{\mathbb{P}}} \exp\left(-\frac{b_{\mathrm{p}\mathbb{P}}+b_{3\mathbb{P}}}{2\alpha'}\Delta_{\mathbb{P}}\right) \\ &\times\left\{\mathrm{Ei}\left[\left(\frac{b_{\mathrm{p}\mathbb{P}}+b_{3\mathbb{P}}}{2\alpha'}+\ln\frac{s}{\Sigma_{\mathrm{L}}}\right)\Delta_{\mathbb{P}}\right]\right. \\ &\left.-\mathrm{Ei}\left[\left(\frac{b_{\mathrm{p}\mathbb{P}}+b_{3\mathbb{P}}}{2\alpha'}+\ln\Sigma_{\mathrm{U}}\right)\Delta_{\mathbb{P}}\right]\right\},\end{aligned} \tag{4.22}$$

where Ei denotes the exponential integral and

$$\Delta_{\mathbb{P}} = \alpha(0) - 1\,. \tag{4.23}$$

In the derivation of (4.22) the squared diffractive mass M_{D}^2 has been integrated over the range

$$\Sigma_{\mathrm{L}} \leq M_{\mathrm{D}}^2 \leq \frac{s}{\Sigma_{\mathrm{U}}}\,, \tag{4.24}$$

where we adopt the bounds from Ref. [94],

$$\Sigma_{\mathrm{L}} = 5\,\mathrm{GeV}^2 \;\text{ and }\; \Sigma_{\mathrm{U}} = 2.5\,. \tag{4.25}$$

For brevity, the expressions for $\sigma_{\mathrm{LP}}(s)$ and $\sigma_{\mathrm{DP}}(s)$ are given in Equations (C.1) and (C.3) in Appendix C.

4.3.2 Coupling matrices of enhanced processes

The triple pomeron and double pomeron diagrams contain several proton-pomeron couplings. In order to obtain consistent rates for low-mass resonance production in the two-channel eikonal model, we have

to modify the parametrization of eikonal matrix elements (4.1) in terms of enhancement factors (4.2). Hence the eikonal matrix (4.4) describes resonance production only for diagrams in which a single pomeron couples to both protons, i.e. for single-pomeron (χ_S and χ_H) and loop pomeron diagrams.

The eikonal matrix of the triple pomeron amplitude, where two pomerons couple to the second proton (in the sense of the numbering in (4.5)), reads

$$\hat{\chi}_{TP_a}(s,b) = \begin{pmatrix} 1+\lambda^2 & 2\lambda & \lambda\left(1+\lambda^2\right) & 2\lambda^2 \\ 2\lambda & 1+\lambda^2 & 2\lambda^2 & \lambda\left(1+\lambda^2\right) \\ \lambda\left(1+\lambda^2\right) & 2\lambda^2 & 1+\lambda^2 & 2\lambda \\ 2\lambda^2 & \lambda\left(1+\lambda^2\right) & 2\lambda & 1+\lambda^2 \end{pmatrix} \chi_{TP_a}(s,b). \tag{4.26}$$

The matrix elements can be derived by counting the number of couplings of the pomeron to the proton or resonance and summing over all possible diagrams. For instance, the elastic-scattering element

$$\langle pp|\hat{\chi}_{TP_a}|pp\rangle = (1+\lambda^2)\chi_{TP_a} \tag{4.27}$$

contains a term proportional to λ^2. This term corresponds to production of a resonance between the two pomeron couplings (similar to the second or third diagram in Fig. 4.2). We derive (4.26) and the other eikonal matrices in Appendix A.1.

4.3.3 Inclusive cross sections

The expressions (4.10) and (4.13)–(4.16) for the total, elastic and low-mass diffraction cross sections in the two-channel eikonal model apply in the presence of enhanced diagrams as well, where the total eikonal matrix is defined as

$$\hat{\chi} = \hat{\chi}_S + \hat{\chi}_H + \hat{\chi}_{TP_a} + \hat{\chi}_{TP_b} + \hat{\chi}_{LP} + \hat{\chi}_{DP}\,. \tag{4.28}$$

For the evaluation of the cross sections we can use the fact that all eikonal matrices commute pairwise, as described in Appendix A.2. The resulting expressions are summarized in Appendix B.2.

4.3.4 Unitarity cuts of enhanced amplitudes

The imaginary parts of enhanced pomeron amplitudes at vanishing momentum transfer arise from unitarity cuts that can be assigned to

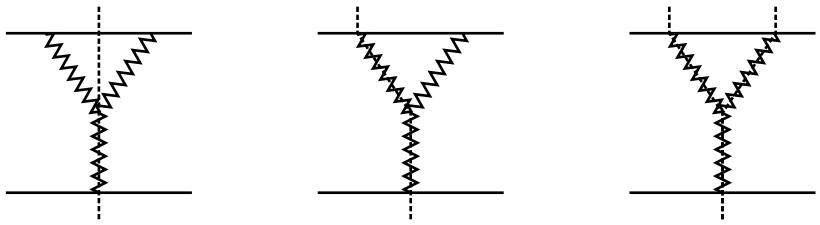

Figure 4.4: Unitarity cuts of the triple pomeron diagram. (a) Diffractive cut. (b) One-pomeron cut. (c) Two-pomeron cut.

several final states [58]. For the calculation of inelastic cross sections we thus have to distribute the cross sections due to enhanced amplitudes to these final states.

In order to illustrate the distribution of the absorptive parts of enhanced amplitudes according to the respective final-state configuration, we first focus on the elastic triple-pomeron amplitude. Figure 4.4 shows the unitarity cuts of this diagram that do not vanish at large centre-of-mass energies. The diffractive cut in Fig. 4.4(a) corresponds to high-mass diffractive dissociation of one proton, i.e. single diffraction. The other two relevant unitarity cuts, namely the one-pomeron cut (Fig. 4.4(b)) and the two-pomeron cut (Fig. 4.4(c)), correspond to multi-peripheral hadron production. The contributions of these three unitarity cuts to the total cross section are proportional to the total absorptive part of the amplitude [58]. Using the optical theorem (1.3), these contributions can be expressed in terms of the triple-pomeron cross section (4.22),

$$\begin{aligned} \sigma_{\text{TP}}^{(\text{a})} &= B_0^2\,\sigma_{\text{TP}} = \;\; (-1)\,\sigma_{\text{TP}}\,, \\ \sigma_{\text{TP}}^{(\text{b})} &= B_1^2\,\sigma_{\text{TP}} = \;\;\;\; 4\;\;\sigma_{\text{TP}}\,, \\ \sigma_{\text{TP}}^{(\text{c})} &= B_2^2\,\sigma_{\text{TP}} = \;\; (-2)\,\sigma_{\text{TP}}\,, \end{aligned} \tag{4.29}$$

where the superscripts (a), (b) and (c) refer to the labels in Fig. 4.4 and B_k^n are the AGK factors introduced in (1.19). Note that this division into several inelastic final states retains unitarity,

$$\sigma_{\text{TP}}^{(\text{a})} + \sigma_{\text{TP}}^{(\text{b})} + \sigma_{\text{TP}}^{(\text{c})} = \sigma_{\text{TP}}\,, \tag{4.30}$$

which directly follows from (1.20).

For simplicity, we identify both the one-pomeron and the two-pomeron cut with the production of a *single* soft subprocess. Alternatively, one could contribute the two-pomeron cut to the production

of two soft subprocesses [94] or even introduce a new subprocess. Our treatment of the two-pomeron cut simplifies the summation of all final-state contributions in amplitudes with multiple enhanced diagrams (see Sec. 4.3.5 below). The correction to the cross section for one soft interaction due to a cut triple pomeron diagram is thus

$$\sigma_{\rm TP}^{\rm soft} = \sigma_{\rm TP}^{\rm (b)} + \sigma_{\rm TP}^{\rm (c)} = 2\,\sigma_{\rm TP}\,. \tag{4.31}$$

This correction is absorptive since the triple pomeron cross section (4.22) is a negative quantity. The TP contribution to the single diffraction cross section is

$$\sigma_{\rm TP}^{\rm sd} = \sigma_{\rm TP}^{\rm (a)} = -\sigma_{\rm TP}\,. \tag{4.32}$$

We can treat the loop pomeron diagram equivalently [36]. In this case, the diffractive cut, proportional to B_0^2, contributes to the cross section for high-mass double diffraction.

The AGK factors for the double pomeron diagram (Fig. 4.3(c)) can be derived by considering it as a triple pomeron diagram in another triple pomeron diagram [94]. This way one finds AGK factors for nine classes of final states,

$$B_i^2 B_j^2 \;\text{ with }\; i,j = 0,1,2. \tag{4.33}$$

Again, we simplify the model by distinguishing only four classes of final states. We consider contributions of the DP diagram to the cross sections for single diffractive excitation. We define these contributions as the sum of cuts passing diffractively through one triple pomeron "subdiagram" (as in Fig. 4.4(a)) and nondiffractively through the other one (as in Figs. 4.4(b) and 4.4(c)),

$$\begin{aligned} \sigma_{\rm DP}^{\rm sd,a} &= \left(B_1^2 + B_2^2\right) B_0^2\,\sigma_{\rm DP} = -2\,\sigma_{\rm DP}\,, \\ \sigma_{\rm DP}^{\rm sd,b} &= -2\,\sigma_{\rm DP}\,. \end{aligned} \tag{4.34}$$

Nondiffractive cuts in both subdiagrams are taken as contribution to single soft interactions,

$$\sigma_{\rm DP}^{\rm soft} = \left(2B_1^2B_2^2 + B_1^2B_1^2 + B_2^2B_2^2\right)\,\sigma_{\rm DP} = 4\,\sigma_{\rm DP}\,. \tag{4.35}$$

Finally, the cut passing nondiffractively through both subdiagrams corresponds to central diffraction,

$$\sigma_{\rm DP}^{\rm cd} = B_0^2 B_0^2\,\sigma_{\rm DP} = \sigma_{\rm DP}\,. \tag{4.36}$$

Table 4.1: Notation for unresolved and resolved cross sections.

Index	$\tilde{\sigma}_{jklmno}$	σ_{jklmno}
j	soft pomerons	soft interactions
k	hard pomerons	hard interactions
l	$\mathrm{TP_a}$ diagrams	single-diffractive excitations of particle a
m	$\mathrm{TP_b}$ diagrams	single-diffractive excitations of particle b
n	LP diagrams	double-diffractive excitations
o	DP diagrams	double pomeron interactions

4.3.5 AGK weights for multiple enhanced diagrams

The cross section corresponding to the imaginary part of the elastic scattering amplitude arising from j soft pomerons, k hard pomerons, l $\mathrm{TP_a}$ diagrams, m $\mathrm{TP_b}$ diagrams, n loop pomeron diagrams and o double pomeron diagrams can be expressed as

$$\tilde{\sigma}_{jklmno}(s) = \frac{1}{4}\sum_{\alpha=1}^{4}\int \mathrm{d}^2b\, I^{(\alpha)}_{jklmno}(s,b), \tag{4.37}$$

with

$$I^{(\alpha)}_{jklmno}(s,b) = \frac{(2\chi^{(\alpha)}_{\mathrm{S}})^j}{j!}\frac{(2\chi^{(\alpha)}_{\mathrm{H}})^k}{k!}\frac{(2\chi^{(\alpha)}_{\mathrm{TP_a}})^l}{l!}\frac{(2\chi^{(\alpha)}_{\mathrm{TP_b}})^m}{m!}\frac{(2\chi^{(\alpha)}_{\mathrm{LP}})^n}{n!}\frac{(2\chi^{(\alpha)}_{\mathrm{DP}})^o}{o!}\mathrm{e}^{-2\chi^{(\alpha)}}. \tag{4.38}$$

In general, the cross sections in (4.37) correspond to several final states. For instance, $\tilde{\sigma}_{001000}$ denotes the cross section due to single cut $\mathrm{TP_a}$ diagram. However, as discussed in Sec. 4.3.4, a cut $\mathrm{TP_a}$ diagram contributes to different final states. We refer to the cross sections in (4.37) thus as unresolved cross sections and reserve the notation σ_{jklmno} (without the tilde superscript) for inelastic cross sections with identified final states.

Similar to Ref. [36], we obtain the resolved inelastic cross section for the *jklmno* final state (see Table 4.1) by adding up all contributing unresolved cross sections (4.37) weighted with counting factors and AGK weights as derived in Sec. 4.3.4. Collecting all partial cross sections that contribute to the *jklmno* final state , we find

$$\begin{aligned}\sigma_{jklmno}(s) = \sum_{\alpha=0}^{j}\sum_{\beta=0}^{j-\alpha}\sum_{\gamma=0}^{j-\alpha-\beta}\sum_{\delta=0}^{j-\alpha-\beta-\gamma}\sum_{\epsilon=0}^{l}\sum_{\zeta=0}^{m} \\ \times A^{\alpha}_{l+\alpha-\epsilon}\, A^{\beta}_{m+\beta-\zeta}\, A^{\gamma}_{n+\gamma}\, C^{\delta\epsilon\zeta}_{o+\delta+\epsilon+\zeta} \\ \times \tilde{\sigma}_{j-\alpha-\beta-\gamma-\delta,k,l+\alpha-\epsilon,m+\beta-\zeta,n+\gamma,o+\delta+\epsilon+\zeta}(s)\,,\end{aligned} \tag{4.39}$$

where we define the factors A_l^α and $C_o^{\alpha\beta\gamma}$ below in (4.40) and (4.41). The summation indices α, β, γ and δ denote the number of soft interactions due to nondiffractive cuts of $\mathrm{TP_a}$, $\mathrm{TP_b}$, LP and DP diagrams, respectively. Hence, the number of cuts soft pomerons, which is given by the first index $(j-\alpha-\beta-\gamma-\delta)$ in the unresolved cross section $\tilde{\sigma}$ (cf. Table 4.1), plus the number of soft interactions due to enhanced diagrams yields exactly j. The indices ϵ and ζ denote the number of single-diffractive excitations of particles a and b.

The factors A_l^α in (4.39) denote the AGK weight for the production of α soft interactions due to a total of k $\mathrm{TP_a}$, $\mathrm{TP_b}$ or LP diagrams. From (4.31) and (4.32) we can derive

$$A_k^\alpha = \binom{k}{\alpha} 2^\alpha (-1)^{k-\alpha}\,, \tag{4.40}$$

where the factor $\binom{k}{\alpha}$ is the number of possibilities to choose α from k. By analogy, we derive the AGK weight factor for the production of α soft interactions and β (γ) single-diffractive excitations of particle a (particle b) due to a total of k double pomeron diagrams from Equations (4.34)–(4.36),

$$C_k^{\alpha\beta\gamma} = \binom{k}{\alpha}\binom{k-\alpha}{\beta}\binom{k-\alpha-\beta}{\gamma} 4^\alpha (-2)^{\beta+\gamma}\,. \tag{4.41}$$

To illustrate the AGK summation in (4.39), we consider the cross section for the production of a single soft interaction. The sum expands to

$$\begin{aligned}\sigma_{100000} &= \left(A_0^0\right)^3 C_0^{000}\,\tilde{\sigma}_{100000} + \left(A_0^0\right)^3 C_1^{100}\,\tilde{\sigma}_{000001} \\ &\quad + A_1^1 \left(A_0^0\right)^2 C_0^{000}\left(\tilde{\sigma}_{001000} + \tilde{\sigma}_{000100} + \tilde{\sigma}_{000010}\right) \\ &= \tilde{\sigma}_{100000} + 4\left(\tilde{\sigma}_{001000} + \tilde{\sigma}_{000100} + \tilde{\sigma}_{000010} + \tilde{\sigma}_{000001}\right),\end{aligned} \tag{4.42}$$

which is made up of the soft-pomeron cross section $\tilde{\sigma}_{100000}$ and one correction term per enhanced diagram. The terms $\tilde{\sigma}_{001000}$, $\tilde{\sigma}_{000100}$ and $\tilde{\sigma}_{000010}$ are negative corrections to the first term since they contain an odd number of (negative) triple and loop pomeron cross sections. However, the last term in (4.42), which results from nondiffractive cuts of a double pomeron diagram, is a positive correction. In total, the corrections from enhanced diagrams are thus reduced by the double pomeron diagram in this example. Generally, we find better convergence of the AGK series (4.39), i.e. positive and decreasing cross sections (for large enough

multiplicities $j, \ldots, o$), if we include the double pomeron diagram in the eikonal model.

We are now ready to define the cross sections for high-mass single diffraction, double diffraction and central diffraction as

$$\begin{aligned} \sigma_{\mathrm{sd,a}}^{\mathrm{hm}}(s) &= \sigma_{001000}(s)\,, \\ \sigma_{\mathrm{sd,b}}^{\mathrm{hm}}(s) &= \sigma_{000100}(s)\,, \\ \sigma_{\mathrm{dd}}^{\mathrm{hm}}(s) &= \sigma_{000010}(s)\,, \\ \sigma_{\mathrm{cd}}(s) &= \sigma_{000001}(s)\,. \end{aligned} \tag{4.43}$$

4.4 Fit to hadron collider and cosmic-ray data

We determine the model parameters in a global fit to hadronic cross sections of proton-proton and proton-antiproton collisions. Since the model contains no reggeon contributions, we restrict the fit to high-energy data. The total pp and $\mathrm{p\overline{p}}$ cross sections are almost identical for $\sqrt{s} > 250\,\mathrm{GeV}$ [48]. Hence we choose this centre-of-mass energy as a lower limit on the input data for the fit (Table 4.2). We add all errors in quadrature if systematic and statistical uncertainties are specified for the measurements. In case of asymmetric errors the higher one is taken.

4.4.1 Definition of observables for comparison with data

We fit the model parameters to the data listed in Table 4.2, which includes the total, elastic, inelastic, single- and double-diffractive cross sections and the elastic slope, measured in proton-proton and proton-antiproton collisions at different centre-of-mass energies. In this connection, the inelastic cross section is calculated as the difference between the total and elastic cross sections, (4.10) and (4.13), which explicitly includes diffractive cross sections. The elastic slope, which also enters the fit, is calculated according to (B.11).

For comparisons of the model to experimental data in the description of single- and double-diffractive cross sections we combine the low-mass and high-mass cross sections, (4.14)–(4.16) and (4.43),

$$\begin{aligned} \sigma_{\mathrm{sd}}(s) &= \sigma_{\mathrm{sd,a}}^{\mathrm{lm}}(s) + \sigma_{\mathrm{sd,b}}^{\mathrm{lm}}(s) + \sigma_{\mathrm{sd,a}}^{\mathrm{hm}}(s) + \sigma_{\mathrm{sd,b}}^{\mathrm{hm}}(s)\,, \\ \sigma_{\mathrm{dd}}(s) &= \sigma_{\mathrm{dd}}^{\mathrm{lm}}(s) + \sigma_{\mathrm{dd}}^{\mathrm{hm}}(s)\,. \end{aligned} \tag{4.44}$$

Table 4.2: Hadronic cross section and elastic slope data used as fit input. Data points marked with an asterisk (*) are taken from Ref. [44].

Total cross section

	$\sqrt{s}$/GeV	σ_{tot}/mb	ref.
pp	273.3	56.0 ± 13.6	[98] *
pp	386.1	54.0 ± 15.5	[98] *
$p\bar{p}$	540.0	66.0 ± 8.6	[99] *
$p\bar{p}$	540.0	66.8 ± 7.1	[100] *
$p\bar{p}$	541.0	63.0 ± 2.1	[101] *
$p\bar{p}$	546.0	61.26 ± 0.93	[102] *
$p\bar{p}$	547.0	61.9 ± 1.8	[103] *
$p\bar{p}$	900.0	65.3 ± 2.4	[104] *
$p\bar{p}$	1800.0	72.8 ± 3.1	[105] *
$p\bar{p}$	1800.0	80.03 ± 2.24	[102] *
pp	6164.1	93.0 ± 14.0	[106] *
pp	7000.0	98.0 ± 2.5	[107]
pp	7000.0	98.6 ± 2.2	[108]
pp	8000.0	101.7 ± 2.9	[43]
pp	8125.8	101.0 ± 16.0	[106] *
pp	10 712.0	117.0 ± 18.0	[106] *
pp	14 121.0	104.0 ± 26.0	[106] *
pp	18 615.0	100.0 ± 27.0	[106] *
pp	24 539.4	124.0 ± 34.0	[106] *
pp	30 000.0	120.0 ± 15.0	[109] *
pp	57 000.0	133.0 ± 29.0	[110]

Single diffraction cross section

	$\sqrt{s}$/GeV	σ_{sd}/mb	ref.
$p\bar{p}$	546.0	7.89 ± 0.33	[111]
$p\bar{p}$	546.0	9.4 ± 0.7	[112]
$p\bar{p}$	900.0	7.8 ± 1.2	[113]
pp	900.0	11.2 ± 2.1	[35]
$p\bar{p}$	1800.0	11.7 ± 2.3	[114]
$p\bar{p}$	1800.0	8.1 ± 1.7	[115]
$p\bar{p}$	1800.0	9.46 ± 0.44	[111]
pp	2760.0	12.2 ± 5.3	[35]
pp	7000.0	14.9 ± 5.9	[35]

Inelastic cross section

	$\sqrt{s}$/GeV	σ_{inel}/mb	ref.
pp	2760.0	62.8 ± 4.2	[35]
pp	7000.0	73.2 ± 5.3	[35]
pp	7000.0	69.4 ± 7.3	[116]
pp	7000.0	68.0 ± 5.1	[117]

Elastic cross section

	$\sqrt{s}$/GeV	σ_{el}/mb	ref.
$p\bar{p}$	546.0	12.87 ± 0.30	[118] *
$p\bar{p}$	547.0	13.3 ± 1.2	[103] *
$p\bar{p}$	1800.0	15.79 ± 0.87	[119] *
$p\bar{p}$	1800.0	16.6 ± 1.6	[114] *
$p\bar{p}$	1800.0	19.70 ± 0.85	[118] *
pp	7000.0	25.1 ± 1.1	[107]
pp	7000.0	25.4 ± 1.1	[108]
pp	8000.0	27.1 ± 1.4	[43]

Elastic slope

	$\sqrt{s}$/GeV	B_{el}/GeV^{-2}	ref.
$p\bar{p}$	540.0	17.2 ± 1.0	[120]
$p\bar{p}$	546.0	15.28 ± 0.58	[118]
$p\bar{p}$	1020.0	16.2 ± 0.7	[121]
$p\bar{p}$	1800.0	16.98 ± 0.25	[118]
$p\bar{p}$	1800.0	16.99 ± 0.47	[105]
pp	7000.0	19.9 ± 0.3	[108]
pp	8000.0	19.9 ± 0.3	[43]

Double diffraction cross section

	$\sqrt{s}$/GeV	σ_{dd}/mb	ref.
pp	900.0	5.6 ± 2.0	[35]
pp	2760.0	7.8 ± 3.2	[35]
pp	7000.0	9.0 ± 2.6	[35]

4.4.2 Model parameters

The two-channel eikonal model including enhanced pomeron contributions involves a number of model parameters. The expressions for the soft, triple, loop and double pomeron cross sections in reggeon field theory depend on

- the proton-pomeron coupling $g_{p\mathbb{P}}$ and the slope describing its t-dependence, $b_{p\mathbb{P}}$;
- the triple pomeron coupling $g_{3\mathbb{P}}$ and the slope describing its t-dependence, $b_{3\mathbb{P}}$; and
- the soft-pomeron intercept $\alpha(0)$ and the soft-pomeron trajectory slope α'.

In order to simplify the fitting procedure, we fix some parameters by making further model assumptions. Following Ref. [94], we fix the soft-pomeron slope to the value from Ref. [48], $\alpha' = 0.25\,\mathrm{GeV}^2$. For the slope of the triple pomeron coupling we use $b_{3\mathbb{P}} = 0.5\,\mathrm{GeV}^{-2}$ [37]. The two-channel formalism brings in a further parameter, the enhancement factor λ.

Another set of parameters is connected with the shape of the impact parameter amplitudes. The widths of the soft, hard and enhanced eikonal functions (2.6), (4.19) and (4.21) in impact parameter space are determined by one parameter each,

$$\mu_i \text{ with } i = \mathrm{S}, \mathrm{H}, \mathrm{TP_a}, \mathrm{TP_b}, \mathrm{LP}, \mathrm{DP}\,. \tag{4.45}$$

We retain μ_H and μ_S as free parameters in the model. For simplicity, we assume a common impact parameter shape for all soft processes,

$$\mu_\mathrm{S} = \mu_{\mathrm{TP_a}} = \mu_{\mathrm{TP_b}} = \mu_\mathrm{LP} = \mu_\mathrm{DP}\,. \tag{4.46}$$

Finally, the hard cross section $\sigma_\mathrm{H}^\mathrm{inc}$ has been defined in (2.1) as the cross section for jet production with transverse momentum greater than $p_\mathrm{T}^\mathrm{min}$. With a constant value of $p_\mathrm{T}^\mathrm{min}$ the inclusive cross section rises with the centre-of-mass energy. In order to study the dependence of the results on the perturbative parts of the model, we create fits for several choices of $p_\mathrm{T}^\mathrm{min}(s)$. Firstly, we create two fits using constant values of $p_\mathrm{T}^\mathrm{min}$ (2.5 GeV and 5.0 GeV). Furthermore, we fit the model for an energy dependence of the cutoff as proposed in Ref. [122],

$$p_\mathrm{T}^\mathrm{min}(s) = 2.5\,\mathrm{GeV} + 0.12\,\mathrm{GeV}\left(\log_{10}\frac{\sqrt{s}}{50\,\mathrm{GeV}}\right)^3\,. \tag{4.47}$$

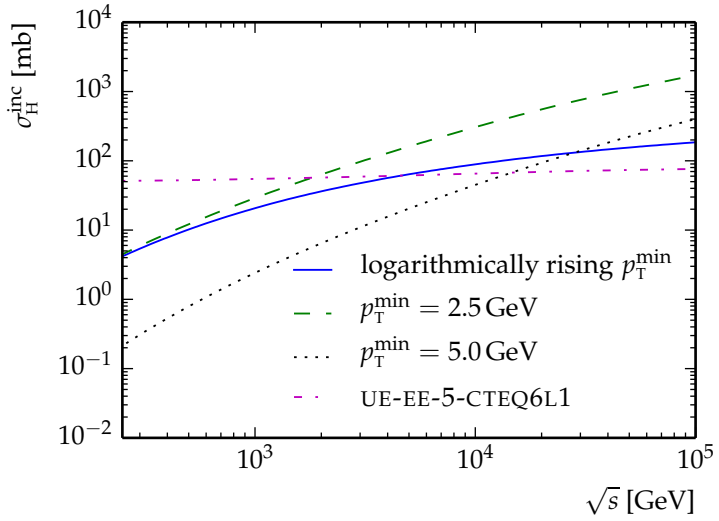

Figure 4.5: Hard inclusive dijet cross section in pp collisions for several energy dependences in the transverse-momentum cutoff, $p_T^{min}(s)$. All results were obtained using the CTEQ6L1 PDF set [92]. The logarithmic energy dependence of p_T^{min} (solid line) is defined in (4.47). The energy dependence of p_T^{min} in the UE-EE-5-CTEQ6L1 tune [123] is given by (3.6), where $p_{T,0}^{min} = 3.92\,GeV$ and $b = 0.33$.

The transverse-momentum cutoff in this formula ranges from $p_T^{min} = 2.5\,GeV$ at $\sqrt{s} = 50\,GeV$ to approximately 5.9 GeV at the highest energy considered in the fit, $\sqrt{s} = 57\,TeV$.

Finally, we adopt a further possibility to vary p_T^{min} with the centre-of-mass energy from our analysis of the underlying event at several energies (see Sec. 3.5.4). Using the multiple-parton interactions model without diffractive components, we found that underlying-event data prefers a rise of the p_T cutoff with the centre-of-mass energy that can be parametrized by a power law,

$$p_T^{min}(s) = p_{T,0}^{min} \left(\frac{\sqrt{s}}{E_0} \right)^b . \qquad \text{(3.6 revisited)}$$

For the fit we use the parameters of the UE-EE-5-CTEQ6L1 tune [123], $p_{T,0}^{min} = 3.92\,GeV$ and $b = 0.33$.

In Fig. 4.5 we can see the jet cross section as a function of the centre-of-mass energy obtained with the mentioned choices of $p_T^{min}(s)$. In comparison to the results with constant p_T^{min}, the logarithmic rise according to (4.47) slightly reduces the growth of the cross section. The power-law parametrization of p_T^{min} in the underlying-event tune yields an almost constant hard inclusive cross section.

Table 4.3: Fit results. (a) $p_T^{\min} = 2.5\,\text{GeV}$. (b) $p_T^{\min} = 5.0\,\text{GeV}$. (c) Energy dependence of $p_T^{\min}$ as in (4.47). (d) Energy dependence of $p_T^{\min}$ from the UE-EE-5-CTEQ6L1 tune [123], which is given by (3.6), where $p_{T,0}^{\min} = 3.92\,\text{GeV}$ and $b = 0.33$.

	$\alpha(0)$	$g_{p\mathbb{P}}$ $\sqrt{\text{mb}}$	$b_{p\mathbb{P}}$ GeV^{-2}	$g_{3\mathbb{P}}$ $\sqrt{\text{mb}}$	λ	μ_H^2 GeV^2	μ_S^2 GeV^2	$\chi^2/\text{d.o.f.}$
(a)	1.12	7.22	5.07	0.05	0.83	0.78	0.97	1.21
(b)	1.23	4.10	4.62	0.03	0.84	0.50	0.98	1.89
(c)	1.10	5.51	5.79	0.21	0.07	0.50	0.62	1.14
(d)	1.29	4.08	4.97	0.00	0.95	1.89	1.40	1.18

4.4.3 Fitting procedure and results

All data points enter the chi-square fit with equal weights. The model allows a good fit to the data ($\chi^2/\text{d.o.f.} < 2$) for all considered energy dependences of $p_T^{\min}$ (Table 4.3). The dependence of the eikonalized cross sections and the elastic slope on $p_T^{\min}$ is thus effectively balanced by the fit parameters.

Figures 4.6–4.9 show the fit results of the considered observables in comparison to experimental data. The total, the inelastic and the elastic cross sections can be well reproduced by the model in the entire energy range. Furthermore, the elastic slope and the single-diffractive cross section are well described by the model. The double-diffractive cross section, however, is underestimated by all fits. We attribute this underestimation to too low values of $g_{3\mathbb{P}}$ or λ (Table 4.3).

Compared to fits using a constant $p_T^{\min}$ or the UE-EE-5-CTEQ6L1 parametrization, the fit using the logarithmic $p_T^{\min}$ dependence (labelled as (c) in Table 4.3) yields a large triple pomeron coupling and a small enhancement factor. However, in all fits the results for the triple pomeron coupling are in tension with the estimation $g_{3\mathbb{P}} \approx 0.2\, g_{p\mathbb{P}}$ from Ref. [124]. In the fit based on the UE-EE-5-CTEQ6L1 parametrization the coupling even vanishes effectively. In this case, the diffractive cross sections completely result from the low-mass parts.

Including additional low-energy data in the fit could help resolving these ambiguities. This would, however, require the inclusion of reggeon contributions in the model. An additional reggeon term in the soft cross section (4.20) brings in further parameters like the reggeon intercept and the coupling of the reggeon to the proton or antiproton. Because of the larger number of parameters, the fitting procedure would be more

elaborate. On the other hand, much low-energy data on the considered observables is available, which could further constrain the parameter space.

4.5 Conclusions

We have studied a model for diffractive cross sections. The model extends the framework that underlies the calculation of hadronic cross sections in the multiple-parton interactions (MPI) model in Herwig++. After relating the MPI model to basic results from scattering theory, we formulated a two-channel eikonal model of production cross sections of diffractive resonances. In this connection, we have cast the results into analytic expressions in terms of the soft and hard eikonal functions from the MPI model. In order to account for processes with higher diffractive masses, we have furthermore included contributions of enhanced pomeron amplitudes in the eikonal model. In preparation for a future Monte Carlo implementation of final states on the basis of this model, we have formulated analytic expressions for exclusive inelastic cross sections. The types of subprocesses to be generated in the final state can be sampled from these cross sections.

The model presented in this chapter has been implemented in Herwig++ in the course of this thesis. The implementation features the possibility to realize arbitrary single-channel or two-channel eikonal models. This way little effort is required to add further enhanced diagrams to the eikonalization. We have determined the model parameters in a global fit to experimental cross section data. With this implementation Herwig++ is ready to calculate cross sections for the proposed single-diffractive, double-diffractive and central-diffractive subprocesses. In particular, the model allows for hadron collisions containing diffractive *and* nondiffractive subprocesses. Since the additional nondiffractive interactions will generally fill the rapidity gap, the presence of these new subprocesses can be expected to affect properties of nondiffractive soft inclusive event samples as well.

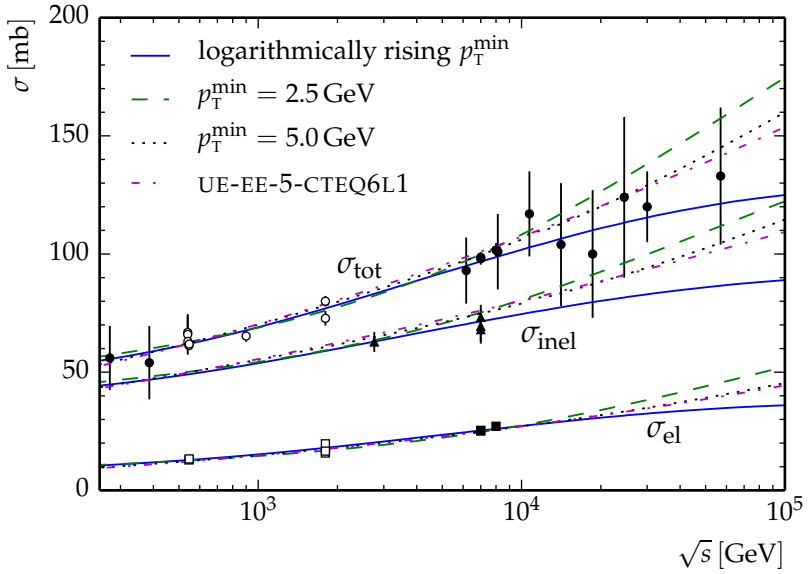

Figure 4.6: Fit results for the total, elastic and inelastic pp cross sections in comparison to experimental data listed in Table 4.2. Total, elastic and inelastic cross section data are indicated with circles, squares and triangles, respectively. Full symbols represent pp data, open ones $p\bar{p}$ data.

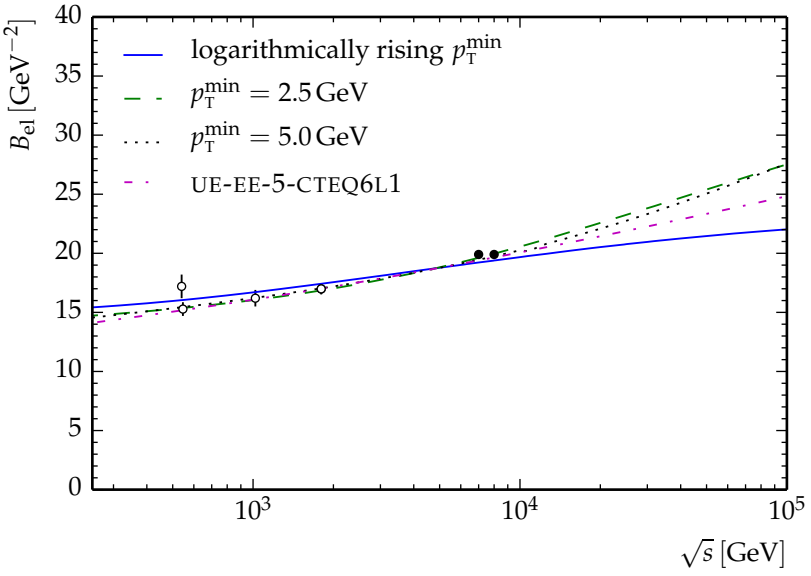

Figure 4.7: Fit results for the elastic slope in pp collisions compared to pp data (full circles) and $p\bar{p}$ data (open circles) listed in Table 4.2.

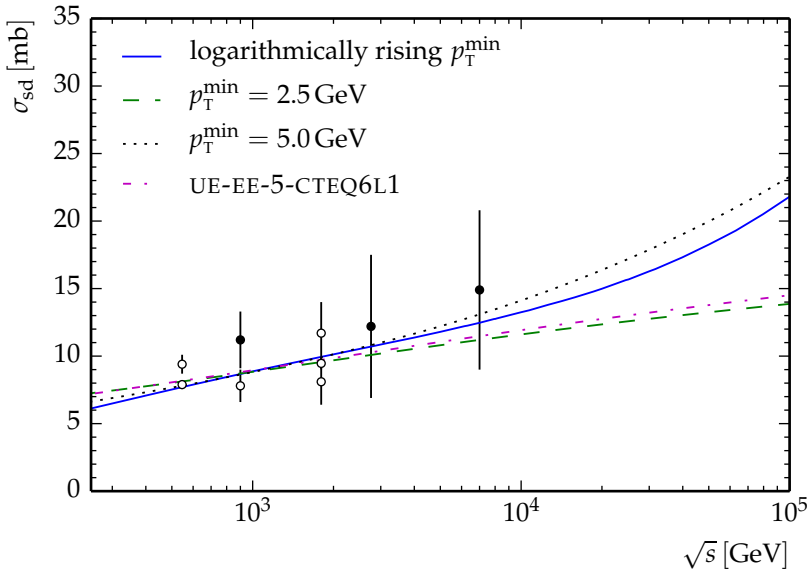

Figure 4.8: Fit results for the single-diffractive pp cross section in comparison to pp data (full circles) and $p\bar{p}$ data (open circles) listed in Table 4.2.

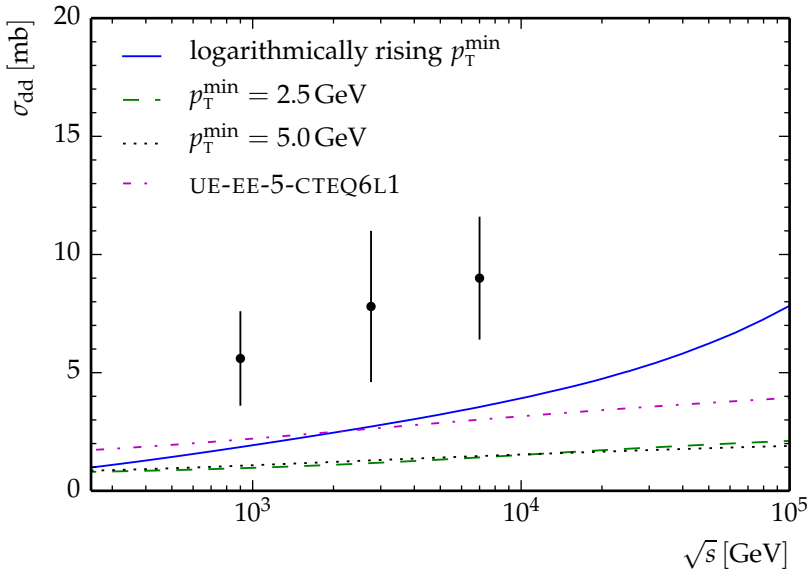

Figure 4.9: Fit results for the double-diffractive pp cross section results in comparison to pp data listed in Table 4.2.

Chapter 5

Summary

In this thesis the simulation of soft inclusive hadron collisions at high energies has been studied. We have addressed this topic in two projects: the analysis of colour reconnections in the presence of multiple parton interactions (MPI) and the joint description of diffractive and MPI cross sections.

The effect of nonperturbative colour reconnections has been investigated in lepton and hadron collider environments. An implementation has been developed in the course of this thesis, which is available in public versions of the event generator Herwig++ [78, 79]. The model redefines colour singlets in the partonic final state after all perturbative modelling has been completed. We find little impact of this algorithm on LEP final states and conclude from this result that the parameters of the hadronization model, which have originally been determined in a fit to LEP data, may remain unchanged.

Regarding soft inclusive hadron collisions, however, we find high sensitivity of the simulation results to colour reconnections. In tunes of the parameters of the colour reconnection and MPI models to diffraction-reduced minimum-bias data from LHC measurements good agreement with the experimental data can be achieved. Moreover, we find an improved description of the underlying event at the Tevatron and the LHC after having adapted the model parameters in further dedicated tunes. In this connection, we find that the model allows for a simple parametrization of its dependence on the centre-of-mass energy. This parametrization is particularly useful for estimating the underlying-event activity at higher collider energies.

In analyses of parton-level final states in lepton and hadron collisions we have shown that the colour reconnection model acts mainly on clusters of nonperturbative origin. These clusters occur in the hadronization

of hadron remnants or of partons that emerge in nonperturbative parts of the event generation. In conclusion, colour reconnection improves the applicability of the MPI model in the simulation of soft inclusive events and of the underlying event in hadron collisions. However, we stress the need for separate tunes for the simulation of soft inclusive events and the underlying event in hard collisions.

The MPI model in HERWIG++ accounts for hadron production in hadron collisions without large rapidity gaps. Diffraction is thus neglected in the simulation of soft inclusive events. We have studied a model for diffractive cross sections in this thesis. This model has been implemented in the event generator HERWIG++ as a special case of a framework for general eikonal models. It extends the existing MPI model with soft and hard nondiffractive parton interactions by modelling cross sections for further "diffractive subprocesses", i.e. for subprocesses that make for hadron production with large rapidity gaps. In fits of the model parameters to experimental data on hadronic cross sections we find a weak dependence of the model predictions on the hard cross section, which is calculated within perturbative QCD. We assess this model as the basis for a future Monte Carlo implementation of diffractive events in soft inclusive event samples.

In order to exploit the full potential of the LHC within the next years and decades, an accurate description of both the hard and the soft aspects of high-energy hadron collisions is inevitable. On the one hand, precise calculations at the perturbative frontier must enter the simulation of LHC final states using Monte Carlo event generators. Given the busy environment in hadron collisions, on the other hand, event generators also should provide reliable results in regimes that are driven by nonperturbative effects. In this thesis we have taken a step forward in the latter direction by studying models that improve the simulation of soft inclusive events and the underlying event in high-energy hadron collisions. The insights we have gained open the door for further event generator developments in this challenging field, which will be necessary to continue the successful LHC programme.

Appendix A

Eikonal matrices

Parts of the calculation presented in this chapter (the discussion in Appendix A.2) are similarly described in Sec. A.2 of Ref. [94]. However, we use different conventions here.

A.1 Derivation of eikonal matrices

With the coupling matrix

$$\hat{g} = \begin{pmatrix} 1 & \lambda \\ \lambda & 1 \end{pmatrix} \tag{A.1}$$

we can write the parametrized pomeron couplings (4.2) in the two-channel eikonal model compactly as

$$g_{ij\mathbb{P}} = g_{\mathrm{pp}\mathbb{P}} \langle i|\hat{g}|j\rangle, \text{ with } i,j \in \{\mathrm{p}, \mathrm{p}^*\}\,, \tag{A.2}$$

where

$$|\mathrm{p}\rangle = \begin{pmatrix} 1 \\ 0 \end{pmatrix} \text{ and } |\mathrm{p}^*\rangle = \begin{pmatrix} 0 \\ 1 \end{pmatrix}. \tag{A.3}$$

We defined the eikonal matrices in Sec. 4.1 with respect to the two-particle basis,

$$|\mathrm{pp}\rangle = \begin{pmatrix} 1 \\ 0 \\ 0 \\ 0 \end{pmatrix},\ |\mathrm{p}^*\mathrm{p}\rangle = \begin{pmatrix} 0 \\ 1 \\ 0 \\ 0 \end{pmatrix},\ |\mathrm{pp}^*\rangle = \begin{pmatrix} 0 \\ 0 \\ 1 \\ 0 \end{pmatrix},\ |\mathrm{p}^*\mathrm{p}^*\rangle = \begin{pmatrix} 0 \\ 0 \\ 0 \\ 1 \end{pmatrix}, \tag{4.5 revisited}$$

which we can understand as the direct product of the one-particle basis (A.3) with itself. The couplings in diagrams with one pomeron coupling appearing on either proton line, i.e. the soft, hard and loop pomeron diagrams, are thus given by the Kronecker product of two coupling matrices (A.1),

$$\hat{\chi}_{\mathrm{S}}(s,b) = (\hat{g} \otimes \hat{g})\, \chi_{\mathrm{S}}(s,b)\,, \tag{A.4}$$

$$\hat{\chi}_{\mathrm{H}}(s,b) = (\hat{g} \otimes \hat{g})\, \chi_{\mathrm{H}}(s,b)\,, \tag{A.5}$$

$$\hat{\chi}_{\mathrm{LP}}(s,b) = (\hat{g} \otimes \hat{g})\, \chi_{\mathrm{LP}}(s,b)\,. \tag{A.6}$$

In a triple-pomeron diagram two pomerons couple to one proton and one to the other one. The respective eikonal matrices are thus

$$\hat{\chi}_{\mathrm{TP_a}}(s,b) = (\hat{g} \otimes \hat{g}^2)\, \chi_{\mathrm{TP,a}}(s,b)\,, \tag{A.7}$$

and

$$\hat{\chi}_{\mathrm{TP,b}}(s,b) = (\hat{g}^2 \otimes \hat{g})\, \chi_{\mathrm{TP,b}}(s,b)\,. \tag{A.8}$$

Finally, the double-pomeron diagram, which has two pomeron couplings on both protons, has an eikonal matrix proportional to $\hat{g}^2 \otimes \hat{g}^2$,

$$\hat{\chi}_{\mathrm{DP}}(s,b) = (\hat{g}^2 \otimes \hat{g}^2)\, \chi_{\mathrm{DP}}(s,b)\,. \tag{A.9}$$

The expanded Kronecker products in (A.4)–(A.9) are

$$\hat{g} \otimes \hat{g} = \begin{pmatrix} 1 & \lambda & \lambda & \lambda^2 \\ \lambda & 1 & \lambda^2 & \lambda \\ \lambda & \lambda^2 & 1 & \lambda \\ \lambda^2 & \lambda & \lambda & 1 \end{pmatrix}, \tag{A.10}$$

$$\hat{g} \otimes \hat{g}^2 = \begin{pmatrix} 1+\lambda^2 & 2\lambda & \lambda\left(1+\lambda^2\right) & 2\lambda^2 \\ 2\lambda & 1+\lambda^2 & 2\lambda^2 & \lambda\left(1+\lambda^2\right) \\ \lambda\left(1+\lambda^2\right) & 2\lambda^2 & 1+\lambda^2 & 2\lambda \\ 2\lambda^2 & \lambda\left(1+\lambda^2\right) & 2\lambda & 1+\lambda^2 \end{pmatrix}, \tag{A.11}$$

$$\hat{g}^2 \otimes \hat{g} = \begin{pmatrix} 1+\lambda^2 & \lambda\left(1+\lambda^2\right) & 2\lambda & 2\lambda^2 \\ \lambda\left(1+\lambda^2\right) & 1+\lambda^2 & 2\lambda^2 & 2\lambda \\ 2\lambda & 2\lambda^2 & 1+\lambda^2 & \lambda\left(1+\lambda^2\right) \\ 2\lambda^2 & 2\lambda & \lambda\left(1+\lambda^2\right) & 1+\lambda^2 \end{pmatrix}, \tag{A.12}$$

$$\hat{g}^2 \otimes \hat{g}^2 = \begin{pmatrix} \left(1+\lambda^2\right)^2 & 2\lambda\left(1+\lambda^2\right) & 2\lambda\left(1+\lambda^2\right) & 4\lambda^2 \\ 2\lambda\left(1+\lambda^2\right) & \left(1+\lambda^2\right)^2 & 4\lambda^2 & 2\lambda\left(1+\lambda^2\right) \\ 2\lambda\left(1+\lambda^2\right) & 4\lambda^2 & \left(1+\lambda^2\right)^2 & 2\lambda\left(1+\lambda^2\right) \\ 4\lambda^2 & 2\lambda\left(1+\lambda^2\right) & 2\lambda\left(1+\lambda^2\right) & \left(1+\lambda^2\right)^2 \end{pmatrix}. \tag{A.13}$$

A.2 Eikonal matrix diagonalization

The matrices in (A.10)–(A.13) commute pairwise, e.g.

$$\left[\hat{g}\otimes\hat{g}, \hat{g}\otimes\hat{g}^2\right] = 0, \tag{A.14}$$

and hence can be diagonalized simultaneously. The unitary transformation matrix

$$S = \frac{1}{2}\begin{pmatrix} 1 & 1 & -1 & 1 \\ -1 & 1 & -1 & -1 \\ -1 & 1 & 1 & 1 \\ 1 & 1 & 1 & -1 \end{pmatrix} \tag{A.15}$$

diagonalizes the eikonal matrices,

$$\begin{aligned}
&S^\dagger(\hat{g}\otimes\hat{g})S = \\
&\quad \mathrm{diag}\left[(1-\lambda)^2, (1+\lambda)^2, 1-\lambda^2, 1-\lambda^2\right], \\
&S^\dagger(\hat{g}\otimes\hat{g}^2)S = \\
&\quad \mathrm{diag}\left[(1-\lambda)^3, (1+\lambda)^3, (1-\lambda)(1+\lambda)^2, (1-\lambda)^2(1+\lambda)\right], \\
&S^\dagger(\hat{g}^2\otimes\hat{g})S = \\
&\quad \mathrm{diag}\left[(1-\lambda)^3, (1+\lambda)^3, (1-\lambda)^2(1+\lambda), (1-\lambda)(1+\lambda)^2\right], \\
&S^\dagger(\hat{g}^2\otimes\hat{g}^2)S = \\
&\quad \mathrm{diag}\left[(1-\lambda)^4, (1+\lambda)^4, (1-\lambda)^2(1+\lambda)^2, (1-\lambda)^2(1+\lambda)^2\right].
\end{aligned} \tag{A.16}$$

The eigenvalues of the eikonal matrices (A.4)–(A.9), corresponding to soft pomeron (S), hard pomeron (H) and loop pomeron exchange (LP), as well as to triple-pomeron (TP) and double pomeron exchange (DP), are thus

$$\left.\begin{aligned}
\chi_\kappa^{(1)} &= (1-\lambda)^2\,\chi_\kappa\,, \\
\chi_\kappa^{(2)} &= (1+\lambda)^2\,\chi_\kappa\,, \\
\chi_\kappa^{(3)} &= \chi_\kappa^{(4)} = (1-\lambda^2)\,\chi_\kappa\,,
\end{aligned}\right\} \quad \text{for } \kappa = \mathrm{S}, \mathrm{H}, \mathrm{LP}\,; \tag{A.17}$$

$$\begin{aligned}
\chi_{\mathrm{TP,a}}^{(1)} &= (1-\lambda)^3\,\chi_{\mathrm{TP,a}}\,, \\
\chi_{\mathrm{TP,a}}^{(2)} &= (1+\lambda)^3\,\chi_{\mathrm{TP,a}}\,, \\
\chi_{\mathrm{TP,a}}^{(3)} &= (1-\lambda)(1+\lambda)^2\,\chi_{\mathrm{TP,a}}\,, \\
\chi_{\mathrm{TP,a}}^{(4)} &= (1-\lambda)^2(1+\lambda)\,\chi_{\mathrm{TP,a}}\,;
\end{aligned} \tag{A.18}$$

$$\begin{aligned}
\chi^{(1)}_{\mathrm{TP,b}} &= (1-\lambda)^3\,\chi_{\mathrm{TP,b}}\,,\\
\chi^{(2)}_{\mathrm{TP,b}} &= (1+\lambda)^3\,\chi_{\mathrm{TP,b}}\,,\\
\chi^{(3)}_{\mathrm{TP,b}} &= (1-\lambda)^2(1+\lambda)\,\chi_{\mathrm{TP,b}}\,,\\
\chi^{(4)}_{\mathrm{TP,b}} &= (1-\lambda)(1+\lambda)^2\,\chi_{\mathrm{TP,b}}\,;
\end{aligned} \tag{A.19}$$

$$\begin{aligned}
\chi^{(1)}_{\mathrm{DP}} &= (1-\lambda)^4\,\chi_{\mathrm{DP}}\,,\\
\chi^{(2)}_{\mathrm{DP}} &= (1+\lambda)^4\,\chi_{\mathrm{DP}}\,,\\
\chi^{(3)}_{\mathrm{DP}} &= \chi^{(4)}_{\mathrm{DP}} = (1-\lambda)^2(1+\lambda)^2\,\chi_{\mathrm{DP}}\,.
\end{aligned} \tag{A.20}$$

By virtue of (A.16), S diagonalizes any polynomial $p(\hat{\chi}_i)$ of eikonal matrices,

$$S^\dagger\, p(\hat{\chi}_i)\, S = p(S^\dagger \hat{\chi}_i S)\,, \tag{A.21}$$

and the exponential function of eikonal matrices,

$$S^\dagger\, \exp(c\hat{\chi}_i)\, S = \mathrm{diag}\left[\exp c\chi_i^{(1)}, \exp c\chi_i^{(2)}, \exp c\chi_i^{(3)}, \exp c\chi_i^{(4)}\right]\,, \tag{A.22}$$

with $c \in \mathbb{R}$. The matrix elements

$$\langle ij|f(\hat{\chi}_i)|\mathrm{pp}\rangle = \left\langle ij\middle|SS^\dagger f(\hat{\chi}_i) SS^\dagger\middle|\mathrm{pp}\right\rangle\,, \tag{A.23}$$

with $i,j \in \{\mathrm{p},\mathrm{p}^*\}$ and $f(\hat{\chi}_i)$ being a product of polynomials and exponential functions, can then be evaluated with

$$S\ \mathrm{diag}(a,b,c,d)\, S^\dagger\, |\mathrm{pp}\rangle = \frac{1}{4}\begin{pmatrix} a+b+c+d\\ -a+b+c-d\\ -a+b-c+d\\ a+b-c-d\end{pmatrix}\,. \tag{A.24}$$

Appendix B

Cross sections in the two-channel eikonal model

B.1 Only single-pomeron amplitudes

The cross sections (4.10)–(4.16) can be evaluated using the relations (A.21)–(A.24). In a model containing only single-pomeron amplitudes the total eikonal matrix reads

$$\hat{\chi} = \hat{\chi}_{\mathrm{S}} + \hat{\chi}_{\mathrm{H}}\,, \tag{B.1}$$

with the eigenvalues

$$\chi^{(\alpha)} = \chi_{\mathrm{S}}^{(\alpha)} + \chi_{\mathrm{H}}^{(\alpha)}\,. \tag{B.2}$$

The resulting total, nondiffractive inelastic and elastic cross sections, and the low-mass single-diffractive and double-diffractive cross sections are

$$\sigma_{\mathrm{tot}}(s) = \frac{1}{2}\int \mathrm{d}^2b \sum_{\alpha=1}^{4} \left(1 - \mathrm{e}^{-\chi^{(\alpha)}}\right)\,, \tag{B.3}$$

$$\sigma_{\mathrm{inel}}^{\mathrm{nd}}(s) = \frac{1}{4}\int \mathrm{d}^2b \sum_{\alpha=1}^{4} \left(1 - \mathrm{e}^{-2\chi^{(\alpha)}}\right)\,, \tag{B.4}$$

$$\sigma_{\mathrm{el}}(s) = \frac{1}{16}\int \mathrm{d}^2b \left|\sum_{\alpha=1}^{4} \left(1 - \mathrm{e}^{-\chi^{(\alpha)}}\right)\right|^2\,, \tag{B.5}$$

$$\sigma_{\mathrm{sd,a}}^{\mathrm{lm}}(s) = \frac{1}{16}\int \mathrm{d}^2b \left|\mathrm{e}^{-\chi^{(1)}} - \mathrm{e}^{-\chi^{(2)}} - \mathrm{e}^{-\chi^{(3)}} + \mathrm{e}^{-\chi^{(4)}}\right|^2\,, \tag{B.6}$$

$$\sigma_{\mathrm{sd,b}}^{\mathrm{lm}}(s) = \frac{1}{16}\int \mathrm{d}^2b \left|\mathrm{e}^{-\chi^{(1)}} - \mathrm{e}^{-\chi^{(2)}} + \mathrm{e}^{-\chi^{(3)}} - \mathrm{e}^{-\chi^{(4)}}\right|^2\,, \tag{B.7}$$

$$\sigma_{\mathrm{dd}}^{\mathrm{lm}}(s) = \frac{1}{16}\int \mathrm{d}^2b \left|\mathrm{e}^{-\chi^{(1)}} + \mathrm{e}^{-\chi^{(2)}} - \mathrm{e}^{-\chi^{(3)}} - \mathrm{e}^{-\chi^{(4)}}\right|^2\,. \tag{B.8}$$

For the cross section for exclusive production of j soft and k hard interactions (4.11), we find

$$\sigma_{jk}(s) = \frac{1}{4}\sum_{\alpha=1}^{4}\int \mathrm{d}^2b \frac{(2\chi_{\mathrm{S}}^{(\alpha)})^j}{j!}\frac{(2\chi_{\mathrm{H}}^{(\alpha)})^k}{k!}\mathrm{e}^{-2\chi^{(\alpha)}}\,. \tag{B.9}$$

B.2 Full model including enhanced diagrams

In the two-channel eikonal model including enhanced pomeron diagrams the eikonal matrix is composed like

$$\hat{\chi} = \hat{\chi}_{\mathrm{S}} + \hat{\chi}_{\mathrm{H}} + \hat{\chi}_{\mathrm{TP_a}} + \hat{\chi}_{\mathrm{TP_b}} + \hat{\chi}_{\mathrm{LP}} + \hat{\chi}_{\mathrm{DP}}\,. \tag{4.28 revisited}$$

The eigenvalues of this matrix are

$$\chi^{(\alpha)} = \chi_{\mathrm{S}}^{(\alpha)} + \chi_{\mathrm{H}}^{(\alpha)} + \chi_{\mathrm{TP_a}}^{(\alpha)} + \chi_{\mathrm{TP_b}}^{(\alpha)} + \chi_{\mathrm{LP}}^{(\alpha)} + \chi_{\mathrm{DP}}^{(\alpha)}\,, \tag{B.10}$$

with $\chi_i^{(\alpha)}$ from (A.17)–(A.20).

The formulae for the total, elastic and low-mass diffraction cross sections, (B.3) and (B.5)–(B.8), apply also for the model including enhanced diagrams, where the eigenvalues (B.2) are to be replaced by (B.10).

We calculate the elastic slope (1.29) in the two-channel model according to

$$B_{\mathrm{el}}(s, t=0)\,\sigma_{\mathrm{tot}}(s) = \frac{1}{4}\int \mathrm{d}^2b\, \boldsymbol{b}^2 \sum_{\alpha=1}^{4}\left(1-\mathrm{e}^{-\chi^{(\alpha)}}\right)\,. \tag{B.11}$$

Appendix C

Enhanced pomeron amplitudes

As discussed above in Sec. 4.3.1, the triple pomeron cross section in reggeon field theory reads [94]

$$\begin{aligned}\sigma_{\mathrm{TP}}(s) = &-\frac{g_{\mathrm{p}\mathbb{P}}^3\, g_{3\mathbb{P}}}{2\alpha' \, 16\pi(\hbar c)^2} \left(\frac{s}{s_0}\right)^{\Delta_{\mathbb{P}}} \exp\left(-\frac{b_{\mathrm{p}\mathbb{P}} + b_{3\mathbb{P}}}{2\alpha'}\Delta_{\mathbb{P}}\right) \\ &\times \left\{ \mathrm{Ei}\left[\left(\frac{b_{\mathrm{p}\mathbb{P}} + b_{3\mathbb{P}}}{2\alpha'} + \ln\frac{s}{\Sigma_{\mathrm{L}}}\right)\Delta_{\mathbb{P}}\right]\right. \\ &\left. - \mathrm{Ei}\left[\left(\frac{b_{\mathrm{p}\mathbb{P}} + b_{3\mathbb{P}}}{2\alpha'} + \ln\Sigma_{\mathrm{U}}\right)\Delta_{\mathbb{P}}\right]\right\},\end{aligned} \tag{4.22 revisited}$$

with $\Delta_{\mathbb{P}} = \alpha(0) - 1$, which we repeat here for completeness. Here, Ei denotes the exponential integral. The loop pomeron cross section is [94]

$$\begin{aligned}\sigma_{\mathrm{LP}}(s) = &-\frac{g_{\mathrm{p}\mathbb{P}}^2\, g_{3\mathbb{P}}^2}{2\alpha' \, 16\pi(\hbar c)^2} \left(\frac{s}{s_0}\right)^{\Delta_{\mathbb{P}}} \exp\left(-\frac{b_{3\mathbb{P}}}{\alpha'}\Delta_{\mathbb{P}}\right) \\ &\times \left[C_1 \,\mathrm{Ei}(C_1\Delta_{\mathbb{P}}) - C_1 \,\mathrm{Ei}(C_2\Delta_{\mathbb{P}})\right. \\ &\left. + \frac{1}{\Delta_{\mathbb{P}}}\exp(C_2\Delta_{\mathbb{P}}) - \frac{1}{\Delta_{\mathbb{P}}}\exp(C_1\Delta_{\mathbb{P}})\right],\end{aligned} \tag{C.1}$$

with

$$\begin{aligned}C_1 &= \frac{b_{3\mathbb{P}}}{\alpha'} + \ln\frac{s s_0}{\Sigma_{\mathrm{L}}^2}\,, \\ C_2 &= \frac{b_{3\mathbb{P}}}{\alpha'} + \ln\Sigma_{\mathrm{U}}\,.\end{aligned} \tag{C.2}$$

where we use the integration bounds $\Sigma_L = 5\,\mathrm{GeV}^2$ and $\Sigma_U = 2.5$. Finally, we calculate the double pomeron cross section according to [94]

$$\begin{aligned}\frac{\mathrm{d}\sigma_{DP}}{\mathrm{d}M_{CD}^2} = &\frac{g_{p\mathbb{P}}^4}{512\pi^2(\hbar c)^4\,\alpha'\,M_{CD}^2}\,\sigma_{\mathbb{P}\mathbb{P}}\left(M_{CD}^2\right)\left(\frac{s}{M_{CD}^2}\right)^{2\Delta_{\mathbb{P}}} \\ &\times\left(b_{p\mathbb{P}} + b_{3\mathbb{P}} + \alpha'\ln\left(s/M_{CD}^2\right)\right)^{-1} \\ &\times\ln\left(\frac{b_{p\mathbb{P}} + b_{3\mathbb{P}} + 2\alpha'\ln\left((1-x_F^{\min})s/M_{CD}^2\right)}{b_{p\mathbb{P}} + b_{3\mathbb{P}} - 2\alpha'\ln(1-x_F^{\min})}\right),\end{aligned} \tag{C.3}$$

with

$$\sigma_{\mathbb{P}\mathbb{P}}(\hat{s}) = g_{3\mathbb{P}}^2\left(\frac{\hat{s}}{s_0}\right)^{\Delta_{\mathbb{P}}}. \tag{C.4}$$

The integration over the squared invariant mass of the central diffractive system, M_{CD}^2, is performed numerically over the range

$$M_{\min}^2 < M_{CD}^2 < \left(1 - x_F^{\min}\right)^2 s\,. \tag{C.5}$$

Following Ref. [94], we use use $M_{\min} = 2\,\mathrm{GeV}$ as the minimum mass of the diffractive system, and $x_F^{\min} = 0.9$ as the minimum Feynman-x of the scattered protons in the central diffractive process.

Bibliography

[1] B. R. Webber. "A QCD Model for Jet Fragmentation Including Soft Gluon Interference". *Nucl. Phys.* B238 (1984), p. 492.

[2] B. Andersson et al. "Parton Fragmentation and String Dynamics". *Phys. Rept.* 97 (1983), pp. 31–145. DOI: 10.1016/0370-1573(83)90080-7.

[3] T. Sjöstrand and M. van Zijl. "A Multiple Interaction Model for the Event Structure in Hadron Collisions". *Phys. Rev.* D36 (1987), p. 2019. DOI: 10.1103/PhysRevD.36.2019.

[4] M. Bähr et al. "Herwig++ Physics and Manual". *Eur. Phys. J.* C58 (2008), pp. 639–707. DOI: 10.1140/epjc/s10052-008-0798-9. arXiv: 0803.0883 [hep-ph].

[5] T. Sjöstrand, S. Mrenna, and P. Z. Skands. "PYTHIA 6.4 Physics and Manual". *JHEP* 05 (2006), p. 026. arXiv: hep-ph/0603175.

[6] T. Sjöstrand, S. Mrenna, and P. Z. Skands. "A Brief Introduction to PYTHIA 8.1". *Comput. Phys. Commun.* 178 (2008), pp. 852–867. DOI: 10.1016/j.cpc.2008.01.036. arXiv: 0710.3820 [hep-ph].

[7] T. Gleisberg et al. "Event generation with SHERPA 1.1". *JHEP* 02 (2009), p. 007. DOI: 10.1088/1126-6708/2009/02/007. arXiv: 0811.4622 [hep-ph].

[8] M. Bähr et al. "Soft interactions in Herwig++". (2009). arXiv: 0905.4671 [hep-ph].

[9] A. Buckley et al. "General-purpose event generators for LHC physics". *Phys. Rept.* 504 (2011), pp. 145–233. DOI: 10.1016/j.physrep.2011.03.005. arXiv: 1101.2599 [hep-ph].

[10] M. Bähr, S. Gieseke, and M. H. Seymour. "Simulation of multiple partonic interactions in Herwig++". *JHEP* 07 (2008), p. 076. DOI: 10.1088/1126-6708/2008/07/076. arXiv: 0803.3633 [hep-ph].

[11] G. Aad et al. "Charged-particle multiplicities in pp interactions at $\sqrt{s} = 900\,\text{GeV}$ measured with the ATLAS detector at the LHC". *Phys. Lett.* B688 (2010), pp. 21–42. DOI: 10.1016/j.physletb.2010.03.064. arXiv: 1003.3124 [hep-ex].

[12] G. Aad et al. "Measurement of underlying event characteristics using charged particles in pp collisions at $\sqrt{s} = 900\,\text{GeV}$ and $7\,\text{TeV}$ with the ATLAS detector". *Phys. Rev. D* 83 (2011), p. 112001. DOI: 10.1103/PhysRevD.83.112001. arXiv: 1012.0791 [hep-ex].

[13] G. Aad et al. "Charged-particle multiplicities in pp interactions measured with the ATLAS detector at the LHC". *New J. Phys.* 13 (2011), p. 053033. DOI: 10.1088/1367-2630/13/5/053033. arXiv: 1012.5104 [hep-ex].

[14] G. Aad et al. "Measurements of underlying-event properties using neutral and charged particles in pp collisions at 900 GeV and 7 TeV with the ATLAS detector at the LHC". *Eur. Phys. J.* C71 (2011), p. 1636. DOI: 10.1140/epjc/s10052-011-1636-z. arXiv: 1103.1816 [hep-ex].

[15] V. Khachatryan et al. "Transverse momentum and pseudorapidity distributions of charged hadrons in pp collisions at $\sqrt{s} = 0.9$ and $2.36\,\text{TeV}$". *JHEP* 1002 (2010), p. 041. DOI: 10.1007/JHEP02(2010)041. arXiv: 1002.0621 [hep-ex].

[16] V. Khachatryan et al. "Transverse-momentum and pseudorapidity distributions of charged hadrons in pp collisions at $\sqrt{s} = 7\,\text{TeV}$". *Phys. Rev. Lett.* 105 (2010), p. 022002. DOI: 10.1103/PhysRevLett.105.022002. arXiv: 1005.3299 [hep-ex].

[17] V. Khachatryan et al. "First Measurement of Hadronic Event Shapes in pp Collisions at $\sqrt{s} = 7\,\text{TeV}$". *Phys. Lett.* B699 (2011), pp. 48–67. DOI: 10.1016/j.physletb.2011.03.060. arXiv: 1102.0068 [hep-ex].

[18] S. Chatrchyan et al. "Measurement of the Underlying Event Activity at the LHC with $\sqrt{s} = 7\,\text{TeV}$ and Comparison with $\sqrt{s} = 0.9\,\text{TeV}$". *JHEP* 1109 (2011), p. 109. DOI: 10.1007/JHEP09(2011)109. arXiv: 1107.0330 [hep-ex].

[19] K. Aamodt et al. "Charged-particle multiplicity measurement in proton-proton collisions at $\sqrt{s} = 0.9$ and $2.36\,\text{TeV}$ with ALICE at LHC". *Eur. Phys. J.* C68 (2010), pp. 89–108. DOI: 10.1140/epjc/s10052-010-1339-x. arXiv: 1004.3034 [hep-ex].

[20] K. Aamodt et al. "Charged-particle multiplicity measurement in proton-proton collisions at $\sqrt{s} = 7\,\text{TeV}$ with ALICE at LHC". *Eur. Phys. J.* C68 (2010), pp. 345–354. DOI: 10.1140/epjc/s10052-010-1350-2. arXiv: 1004.3514 [hep-ex].

[21] K. Aamodt et al. "Transverse momentum spectra of charged particles in proton-proton collisions at $\sqrt{s} = 900\,\text{GeV}$ with ALICE at the LHC". *Phys. Lett.* B693 (2010), pp. 53–68. DOI: 10.1016/j.physletb.2010.08.026. arXiv: 1007.0719 [hep-ex].

[22] P. Z. Skands and D. Wicke. "Non-perturbative QCD effects and the top mass at the Tevatron". *Eur. Phys. J.* C52 (2007), pp. 133–140. DOI: 10.1140/epjc/s10052-007-0352-1. arXiv: hep-ph/0703081.

[23] G. Gustafson, U. Pettersson, and P. M. Zerwas. "Jet Final States in WW Pair Production and Color Screening in the QCD Vacuum". *Phys. Lett.* B209 (1988), p. 90. DOI: 10.1016/0370-2693(88)91836-9.

[24] T. Sjöstrand and V. A. Khoze. "Does the W mass reconstruction survive QCD effects?" *Phys. Rev. Lett.* 72 (1994), pp. 28–31. DOI: 10.1103/PhysRevLett.72.28. arXiv: hep-ph/9310276 [hep-ph].

[25] T. Sjöstrand and V. A. Khoze. "On Color rearrangement in hadronic W^+W^- events". *Z. Phys.* C62 (1994), pp. 281–310. DOI: 10.1007/BF01560244. arXiv: hep-ph/9310242.

[26] G. Gustafson and J. Häkkinen. "Color interference and confinement effects in W pair production". *Z. Phys.* C64 (1994), pp. 659–664. DOI: 10.1007/BF01957774.

[27] L. Lönnblad. "Reconnecting colored dipoles". *Z. Phys.* C70 (1996), pp. 107–114. DOI: 10.1007/s002880050087.

[28] C. Friberg, G. Gustafson, and J. Häkkinen. "Color connections in e+ e- annihilation". *Nucl. Phys.* B490 (1997), pp. 289–305. DOI: 10.1016/S0550-3213(97)00064-3. arXiv: hep-ph/9604347 [hep-ph].

[29] B. R. Webber. "Colour reconnection and Bose-Einstein effects". *J. Phys.* G24 (1998), pp. 287–296. DOI: 10.1088/0954-3899/24/2/003. arXiv: hep-ph/9708463.

[30] P. Achard et al. "Search for color reconnection effects in $e^+e^- \to W^+W^- \to$ hadrons through particle flow studies at LEP". *Phys. Lett.* B561 (2003), pp. 202–212. DOI: 10.1016/S0370-2693(03)00490-8. arXiv: hep-ex/0303042.

[31] G. Abbiendi et al. "Colour reconnection in $e^+e^- \to W^+W^-$ at $\sqrt{s} =$ 189–209 GeV". *Eur. Phys. J.* C45 (2006), pp. 291–305. DOI: 10.1140/epjc/s2005-02439-x. arXiv: hep-ex/0508062.

[32] J. Abdallah et al. "Investigation of Colour Reconnection in WW Events with the DELPHI detector at LEP-2". *Eur. Phys. J.* C51 (2007), pp. 249–269. DOI: 10.1140/epjc/s10052-007-0304-9. arXiv: 0704.0597 [hep-ex].

[33] P. Z. Skands. "Tuning Monte Carlo Generators: The Perugia Tunes". *Phys. Rev.* D82 (2010), p. 074018. DOI: 10.1103/PhysRevD.82.074018. arXiv: 1005.3457 [hep-ph].

[34] D. Amati and G. Veneziano. "Preconfinement as a Property of Perturbative QCD". *Phys. Lett.* B83 (1979), p. 87. DOI: 10.1016/0370-2693(79)90896-7.

[35] B. Abelev et al. "Measurement of inelastic, single- and double-diffraction cross sections in proton-proton collisions at the LHC with ALICE". *Eur. Phys. J.* C73 (2013), p. 2456. DOI: 10.1140/epjc/s10052-013-2456-0. arXiv: 1208.4968 [hep-ex].

[36] P. Aurenche et al. "Multiparticle production in a two-component dual parton model". *Phys.Rev.* D45 (1992), pp. 92–105. DOI: 10.1103/PhysRevD.45.92.

[37] R. Engel. "Photoproduction within the two component dual parton model. 1. Amplitudes and cross-sections". *Z. Phys.* C66 (1995), pp. 203–214. DOI: 10.1007/BF01496594.

[38] R. Engel and J. Ranft. "Hadronic photon-photon interactions at high-energies". *Phys. Rev.* D54 (1996), pp. 4244–4262. DOI: 10.1103/PhysRevD.54.4244. arXiv: hep-ph/9509373 [hep-ph].

[39] J. R. Forshaw and D. Ross. "Quantum Chromodynamics and the Pomeron". *Camb. Lect. Notes Phys.* 9 (1997), pp. 1–248.

[40] S. Donnachie et al. "Pomeron physics and QCD". *Camb. Monogr. Part. Phys. Nucl. Phys. Cosmol.* 19 (2002), pp. 1–347.

[41] V. Barone and E. Predazzi. *High-Energy Particle Diffraction*. Springer, 2002. ISBN: 9783540421078.

[42] M. Block and R. Cahn. "High-Energy $p\bar{p}$ and pp Forward Elastic Scattering and Total Cross-Sections". *Rev. Mod. Phys.* 57 (1985), p. 563. DOI: 10.1103/RevModPhys.57.563.

[43] G. Antchev et al. "Luminosity-Independent Measurement of the Proton-Proton Total Cross Section at $\sqrt{s} = 8\,\text{TeV}$". *Phys. Rev. Lett.* 111.1 (2013), p. 012001. DOI: 10.1103/PhysRevLett.111.012001.

[44] J. Beringer et al. "Review of Particle Physics (RPP)". *Phys. Rev.* D86 (2012), p. 010001. DOI: 10.1103/PhysRevD.86.010001.

[45] T. Regge. "Introduction to complex orbital momenta". *Nuovo Cim.* 14 (1959), p. 951. DOI: 10.1007/BF02728177.

[46] G. Chew and S. C. Frautschi. "Principle of Equivalence for All Strongly Interacting Particles Within the S Matrix Framework". *Phys. Rev. Lett.* 7 (1961), pp. 394–397. DOI: 10.1103/PhysRevLett.7.394.

[47] G. Chew and S. C. Frautschi. "Regge Trajectories and the Principle of Maximum Strength for Strong Interactions". *Phys. Rev. Lett.* 8 (1962), pp. 41–44. DOI: 10.1103/PhysRevLett.8.41.

[48] A. Donnachie and P. V. Landshoff. "Total cross-sections". *Phys. Lett.* B296 (1992), pp. 227–232. DOI: 10.1016/0370-2693(92)90832-O. arXiv: hep-ph/9209205.

[49] J.-R. Cudell, K. Kang, and S. K. Kim. "Bounds on the soft pomeron intercept". *Phys. Lett.* B395 (1997), pp. 311–317. arXiv: hep-ph/9601336.

[50] J.-R. Cudell et al. "Benchmarks for the forward observables at RHIC, the Tevatron Run II and the LHC". *Phys. Rev. Lett.* 89 (2002), p. 201801. DOI: 10.1103/PhysRevLett.89.201801. arXiv: hep-ph/0206172.

[51] L. Lipatov. "Reggeization of the Vector Meson and the Vacuum Singularity in Nonabelian Gauge Theories". *Sov. J. Nucl. Phys.* 23 (1976), pp. 338–345.

[52] V. S. Fadin, E. Kuraev, and L. Lipatov. "On the Pomeranchuk Singularity in Asymptotically Free Theories". *Phys. Lett.* B60 (1975), pp. 50–52. DOI: 10.1016/0370-2693(75)90524-9.

[53] E. Kuraev, L. Lipatov, and V. S. Fadin. "The Pomeranchuk Singularity in Nonabelian Gauge Theories". *Sov. Phys. JETP* 45 (1977), pp. 199–204.

[54] I. Balitsky and L. Lipatov. "The Pomeranchuk Singularity in Quantum Chromodynamics". *Sov. J. Nucl. Phys.* 28 (1978), pp. 822–829.

[55] V. Gribov. "A Reggeon Diagram Technique". *Sov. Phys. JETP* 26 (1968), pp. 414–422.

[56] A. Kaidalov. "Diffractive Production Mechanisms". *Phys. Rept.* 50 (1979), pp. 157–226. DOI: 10.1016/0370-1573(79)90043-7.

[57] D. Amati, A. Stanghellini, and S. Fubini. "Theory of high-energy scattering and multiple production". *Nuovo Cim.* 26 (1962), pp. 896–954. DOI: 10.1007/BF02781901.

[58] V. Abramovsky, V. Gribov, and O. Kancheli. "Character of Inclusive Spectra and Fluctuations Produced in Inelastic Processes by Multi-Pomeron Exchange". *Yad. Fiz.* 18 (1973), pp. 595–616.

[59] M. Baker and K. Ter-Martirosian. "Gribov's Reggeon Calculus: Its Physical Basis and Implications". *Phys. Rept.* 28 (1976), pp. 1–143. DOI: 10.1016/0370-1573(76)90002-8.

[60] F. Abe et al. "Double parton scattering in $\overline{\mathrm{p}}\mathrm{p}$ collisions at $\sqrt{s} = 1.8\,\mathrm{TeV}$". *Phys. Rev.* D56 (1997), pp. 3811–3832. DOI: 10.1103/PhysRevD.56.3811.

[61] M. Bähr, J. M. Butterworth, and M. H. Seymour. "The Underlying Event and the Total Cross Section from Tevatron to the LHC". *JHEP* 01 (2009), p. 065. DOI: 10.1088/1126-6708/2009/01/065. arXiv: 0806.2949 [hep-ph].

[62] J. Butterworth, J. R. Forshaw, and M. Seymour. "Multiparton interactions in photoproduction at HERA". *Z. Phys.* C72 (1996), pp. 637–646. DOI: 10.1007/s002880050286. arXiv: hep-ph/9601371.

[63] M. Bähr. "Underlying Event Simulation in the Herwig++ Event Generator". PhD thesis. 2008. URL: http://digbib.ubka.uni-karlsruhe.de/volltexte/1000010075.

[64] A. A. Affolder et al. "Charged jet evolution and the underlying event in $p\bar{p}$ collisions at 1.8 TeV". *Phys. Rev.* D65 (2002), p. 092002. DOI: 10.1103/PhysRevD.65.092002.

[65] I. Borozan and M. H. Seymour. "An eikonal model for multiparticle production in hadron hadron interactions". *JHEP* 09 (2002), p. 015. arXiv: hep-ph/0207283.

[66] G. 't Hooft. "A planar diagram theory for strong interactions". *Nucl. Phys.* B72 (1974), p. 461. DOI: 10.1016/0550-3213(74)90154-0.

[67] S. Plätzer and M. Sjödahl. "Subleading N_c improved Parton Showers". *JHEP* 1207 (2012), p. 042. DOI: 10.1007/JHEP07(2012)042. arXiv: 1201.0260 [hep-ph].

[68] S. Gieseke et al. "Herwig++ 1.0: An Event Generator for e^+e^- Annihilation". *JHEP* 02 (2004), p. 005. arXiv: hep-ph/0311208.

[69] S. Gieseke, C. Röhr, and A. Siódmok. "Colour reconnections in Herwig++". *Eur. Phys. J.* C72 (2012), p. 2225. DOI: 10.1140/epjc/s10052-012-2225-5. arXiv: 1206.0041 [hep-ph].

[70] S. Gieseke et al. "Minimum bias and underlying event developments in Herwig++". (2010), pp. 194–198. DOI: 10.3204/DESY-PROC-2010-01/236.

[71] S. Gieseke, C. A. Röhr, and A. Siódmok. "Tuning of the multiple parton interaction model in Herwig++ using early LHC data". (2012), pp. 67–74. DOI: 10.3204/DESY-PROC-2012-03/48.

[72] S. Gieseke, C. Röhr, and A. Siódmok. "The Underlying Event in Herwig++". (2012), pp. 785–788. DOI: 10.3204/DESY-PROC-2012-02/367. arXiv: 1206.2205 [hep-ph].

[73] S. Gieseke, C. Röhr, and A. Siódmok. "Multiparton interactions in Herwig++". (2012), pp. 51–56. DOI: 10.3204/DESY-PROC-2012-03/45.

[74] S. Gieseke, C. Röhr, and A. Siódmok. "Multiple Partonic Interactions in Herwig++". *Acta Phys. Polon. Supp.* 6 (2013), pp. 613–620. DOI: 10.5506/APhysPolBSupp.6.613. arXiv: 1302.4892 [hep-ph].

[75] A. Buckley et al. "Systematic event generator tuning for the LHC". *Eur. Phys. J.* C65 (2010), pp. 331–357. DOI: 10.1140/epjc/s10052-009-1196-7. arXiv: 0907.2973 [hep-ph].

[76] S. Gieseke, C. Röhr, and A. Siódmok. "Multiple Partonic Interaction Developments in Herwig++". 2011.

[77] P. Bartalini et al. "Multi-Parton Interactions at the LHC". 2011.

[78] S. Gieseke et al. "Herwig++ 2.5 Release Note". (2011). arXiv: 1102.1672 [hep-ph].

[79] K. Arnold et al. "Herwig++ 2.6 Release Note". (2012). arXiv: 1205.4902 [hep-ph].

[80] S. Kirkpatrick, C. D. Gelatt, and M. P. Vecchi. "Optimization by simulated annealing". *Science* 220 (1983), pp. 671–680.

[81] G. Abbiendi et al. "Measurement of event shape distributions and moments in $e^+e^- \to$ hadrons at 91 GeV – 209 GeV and a determination of α_s". *Eur. Phys. J.* C40 (2005), pp. 287–316. DOI: 10.1140/epjc/s2005-02120-6. arXiv: hep-ex/0503051.

[82] G. Abbiendi et al. "A simultaneous measurement of the QCD colour factors and the strong coupling". *Eur. Phys. J.* C20 (2001), pp. 601–615. DOI: 10.1007/s100520100699. arXiv: hep-ex/0101044.

[83] K. Ackerstaff et al. "Measurements of flavour dependent fragmentation functions in $Z^0 \to q\bar{q}$ events". *Eur. Phys. J.* C7 (1999), pp. 369–381. DOI: 10.1007/s100529901067. arXiv: hep-ex/9807004.

[84] P. Pfeifenschneider et al. "QCD analyses and determinations of α_S in e^+e^- annihilation at energies between 35 GeV and 189 GeV". *Eur. Phys. J.* C17 (2000), pp. 19–51. DOI: 10.1007/s100520000432. arXiv: hep-ex/0001055.

[85] P. Abreu et al. "Strange baryon production in Z hadronic decays". *Z. Phys.* C67 (1995), pp. 543–554. DOI: 10.1007/BF01553980.

[86] P. Abreu et al. "Tuning and test of fragmentation models based on identified particles and precision event shape data". *Z. Phys.* C73 (1996), pp. 11–60. DOI: 10.1007/s002880050295.

[87] R. Barate et al. "Studies of quantum chromodynamics with the ALEPH detector". *Phys. Rept.* 294 (1998), pp. 1–165. DOI: 10.1016/S0370-1573(97)00045-8.

[88] D. Decamp et al. "Measurement of the charged particle multiplicity distribution in hadronic Z decays". *Phys. Lett.* B273 (1991), pp. 181–192. DOI: 10.1016/0370-2693(91)90575-B.

[89] A. Heister et al. "Studies of QCD at e^+e^- centre-of-mass energies between 91 GeV and 209 GeV". *Eur. Phys. J.* C35 (2004), pp. 457–486. DOI: 10.1140/epjc/s2004-01891-4.

[90] D. Duchesneau. "New method based on energy and particle flow in $e^+e^- \to W^+W^- \to$ hadron events for color reconnection studies". (2000).

[91] A. Buckley et al. "Rivet user manual". (2010). arXiv: 1003.0694 [hep-ph].

[92] J. Pumplin et al. "New generation of parton distributions with uncertainties from global QCD analysis". *JHEP* 07 (2002), p. 012. arXiv: hep-ph/0201195.

[93] A. Sherstnev and R. S. Thorne. "Parton Distributions for LO Generators". *Eur. Phys. J.* C55 (2008), pp. 553–575. DOI: 10.1140/epjc/s10052-008-0610-x. arXiv: 0711.2473 [hep-ph].

[94] R. Engel. "Hadronic interactions of photons at high energies". PhD thesis. 1997.

[95] E.-J. Ahn et al. "Cosmic ray interaction event generator SIBYLL 2.1". *Phys. Rev.* D80 (2009), p. 094003. DOI: 10.1103/PhysRevD.80.094003. arXiv: 0906.4113 [hep-ph].

[96] C. Pajares, A. Varias, and P. Yepes. "Reggeon Calculus at Collider Energies". *Z. Phys.* C19 (1983), pp. 89–93. DOI: 10.1007/BF01572342.

[97] M. Ryskin, A. Martin, and V. Khoze. "High-energy strong interactions: from 'hard' to 'soft'". *Eur. Phys. J.* C71 (2011), p. 1617. DOI: 10.1140/epjc/s10052-011-1617-2. arXiv: 1102.2844 [hep-ph].

[98] G. Aielli et al. "Proton-air cross section measurement with the ARGO-YBJ cosmic ray experiment". *Phys. Rev.* D80 (2009), p. 092004. DOI: 10.1103/PhysRevD.80.092004. arXiv: 0904.4198 [hep-ex].

[99] R. Battiston et al. "Measurement of the Proton-Antiproton Elastic and Total Cross-section at a Center-of-mass Energy of 540 GeV". *Phys. Lett.* B117 (1982), p. 126. DOI: 10.1016/0370-2693(82)90888-7.

[100] G. Arnison et al. "Elastic and Total Cross-section Measurement at the CERN Proton - Antiproton Collider". *Phys. Lett.* B128 (1983), p. 336. DOI: 10.1016/0370-2693(83)90271-X.

[101] C. Augier et al. "Measurement of the proton-antiproton total cross-section at the S$\overline{\text{p}}$pS collider by a luminosity dependent method". *Phys. Lett.* B344 (1995), pp. 451–454. DOI: 10.1016/0370-2693(94)01485-U.

[102] F. Abe et al. "Measurement of the $\overline{\text{p}}\text{p}$ total cross-section at $\sqrt{s} = 546\,\text{GeV}$ and 1800 GeV". *Phys. Rev.* D50 (1994), pp. 5550–5561. DOI: 10.1103/PhysRevD.50.5550.

[103] M. Bozzo et al. "Measurement of the Proton-Antiproton Total and Elastic Cross-Sections at the CERN SPS Collider". *Phys. Lett.* B147 (1984), p. 392. DOI: 10.1016/0370-2693(84)90139-4.

[104] G. Alner et al. "Antiproton-proton cross sections at 200 and 900 GeV c.m. energy". *Z. Phys.* C32 (1986), pp. 153–161. DOI: 10.1007/BF01552491.

[105] N. A. Amos et al. "Measurement of ρ, the ratio of the real to imaginary part of the $\bar{p}p$ forward elastic scattering amplitude, at $\sqrt{s} = 1.8\,\text{TeV}$". *Phys. Rev. Lett.* 68 (1992), pp. 2433–2436. DOI: 10.1103/PhysRevLett.68.2433.

[106] M. Honda et al. "Inelastic cross-section for p-air collisions from air shower experiment and total cross-section for pp collisions at SSC energy". *Phys. Rev. Lett.* 70 (1993), pp. 525–528. DOI: 10.1103/PhysRevLett.70.525.

[107] G. Antchev et al. "Luminosity-independent measurements of total, elastic and inelastic cross-sections at $\sqrt{s} = 7\,\text{TeV}$". *Europhys. Lett.* 101 (2013), p. 21004. DOI: 10.1209/0295-5075/101/21004.

[108] G. Antchev et al. "Measurement of proton-proton elastic scattering and total cross-section at $\sqrt{s} = 7\,\text{TeV}$". *Europhys. Lett.* 101 (2013), p. 21002. DOI: 10.1209/0295-5075/101/21002.

[109] R. Baltrusaitis et al. "Total Proton Proton Cross-Section at $\sqrt{s} = 30\,\text{TeV}$". *Phys. Rev. Lett.* 52 (1984), pp. 1380–1383. DOI: 10.1103/PhysRevLett.52.1380.

[110] P. Abreu et al. "Measurement of the proton-air cross-section at $\sqrt{s} = 57\,\text{TeV}$ with the Pierre Auger Observatory". *Phys. Rev. Lett.* 109 (2012), p. 062002. DOI: 10.1103/PhysRevLett.109.062002. arXiv: 1208.1520 [hep-ex].

[111] F. Abe et al. "Measurement of $\bar{p}p$ single diffraction dissociation at $\sqrt{s} = 546\,\text{GeV}$ and $1800\,\text{GeV}$". *Phys. Rev.* D50 (1994), pp. 5535–5549. DOI: 10.1103/PhysRevD.50.5535.

[112] D. Bernard et al. "The Cross-section of Diffraction Dissociation at the CERN SPS Collider". *Phys. Lett.* B186 (1987), p. 227. DOI: 10.1016/0370-2693(87)90285-1.

[113] R. Ansorge et al. "Diffraction Dissociation at the CERN Pulsed Collider at CM Energies of 900 GeV and 200 GeV". *Z. Phys.* C33 (1986), p. 175. DOI: 10.1007/BF01411134.

[114] N. A. Amos et al. "A Luminosity-independent Measurement of the $\bar{p}p$ Total Cross-section at $\sqrt{s} = 1.8\,\text{TeV}$". *Phys. Lett.* B243 (1990), pp. 158–164. DOI: 10.1016/0370-2693(90)90973-A.

[115] N. A. Amos et al. "Diffraction dissociation in $\bar{p}p$ collisions at $\sqrt{s} = 1.8\,\text{TeV}$". *Phys. Lett.* B301 (1993), pp. 313–316. DOI: 10.1016/0370-2693(93)90707-O.

[116] G. Aad et al. "Measurement of the Inelastic Proton-Proton Cross-Section at $\sqrt{s} = 7\,\text{TeV}$ with the ATLAS Detector". *Nature Commun.* 2 (2011), p. 463. DOI: 10.1038/ncomms1472. arXiv: 1104.0326 [hep-ex].

[117] *Inelastic pp cross section at 7 TeV*. Tech. rep. CMS-PAS-FWD-11-001. Geneva: CERN, 2011.

[118] F. Abe et al. "Measurement of small angle $\overline{p}p$ elastic scattering at $\sqrt{s} = 546\,\text{GeV}$ and $1800\,\text{GeV}$". *Phys. Rev.* D50 (1994), pp. 5518–5534. DOI: 10.1103/PhysRevD.50.5518.

[119] C. Avila et al. "A Measurement of the proton-antiproton total cross-section at $\sqrt{s} = 1.8\,\text{TeV}$". *Phys. Lett.* B445 (1999), pp. 419–422. DOI: 10.1016/S0370-2693(98)01421-X.

[120] R. Battiston et al. "First Results on Low Momentum Transfer Elastic Scattering at the CERN Proton-Antiproton Collider". *Phys. Lett.* B115 (1982), p. 333. DOI: 10.1016/0370-2693(82)90382-3.

[121] N. A. Amos et al. "$\overline{p}p$ elastic scattering at $\sqrt{s} = 1020\,\text{GeV}$". *Nuovo Cim.* A106 (1993), pp. 123–132. DOI: 10.1007/BF02771512.

[122] F. W. Bopp et al. "New parton structure functions and mini-jets in the two component dual parton model". *Phys. Rev.* D49 (1994), pp. 3236–3247. DOI: 10.1103/PhysRevD.49.3236.

[123] M. H. Seymour and A. Siódmok. "Constraining MPI models using $\sigma_{\text{effective}}$ and recent Tevatron and LHC Underlying Event data". (2013). arXiv: 1307.5015 [hep-ph].

[124] E. Luna et al. "Diffractive dissociation re-visited for predictions at the LHC". *Eur. Phys. J.* C59 (2009), pp. 1–12. DOI: 10.1140/epjc/s10052-008-0793-1. arXiv: 0807.4115 [hep-ph].

Acknowledgements

In the first place, I would like to thank Stefan Gieseke for his inspiring supervision throughout my PhD. I learned a lot from him during the last years. I would like to thank him particularly for always making time for me when I had questions. I would like to thank Dieter Zeppenfeld for agreeing to be my second supervisor. I am particularly thankful for his valuable feedback on my work. I am grateful to both my supervisors for giving me the possibility to attend numerous workshops, schools and conferences, from which I could gain insight into various aspects of elementary particle physics and related topics.

Further thanks go to all members of the Herwig collaboration for critical discussions and support. In this context, I would particularly like to thank Andrzej Síodmok for the very pleasant collaboration.

Many thanks go to Adam Davison and Jon Butterworth, from whom I learned a lot about experimental aspects of collider physics during my stay at UCL in London. Furthermore, I would like to thank Ralph Engel and Anatoli Fedynitch for inspiring discussions about the diffraction model in Phojet. I would also like to thank Markus Diehl, Jeff Forshaw, Simon Plätzer and Mike Seymour for fruitful discussions on diffraction.

I would like to thank the members of the Institut für Theoretische Physik for always creating a nice atmosphere. Special thanks go to Bastian Feigl, Ramona Gröber, Christian Hangst and Franziska Schissler for supporting me by proofreading this thesis. It was a pleasure for me to work with Johannes Bellm, Bastian Feigl, Thomas Hermann, Jens Hoff, Peter Marquard and Robin Roth on the system administration for the ITP and TTP institutes. I would like to thank them for their work and pleasant collaboration.

This work was in part supported by the Helmholtz Alliance "Physics at the Terascale", the Bundesministerium für Bildung und Forschung and the EU Marie Curie Research Training Network MCnet.

Finally, I would like to thank Jorinne Sturm and my family for their support and patience.